# Flux and polarization signals of the Trappist-1 system

## Numerical simulations

Fouad Abiad

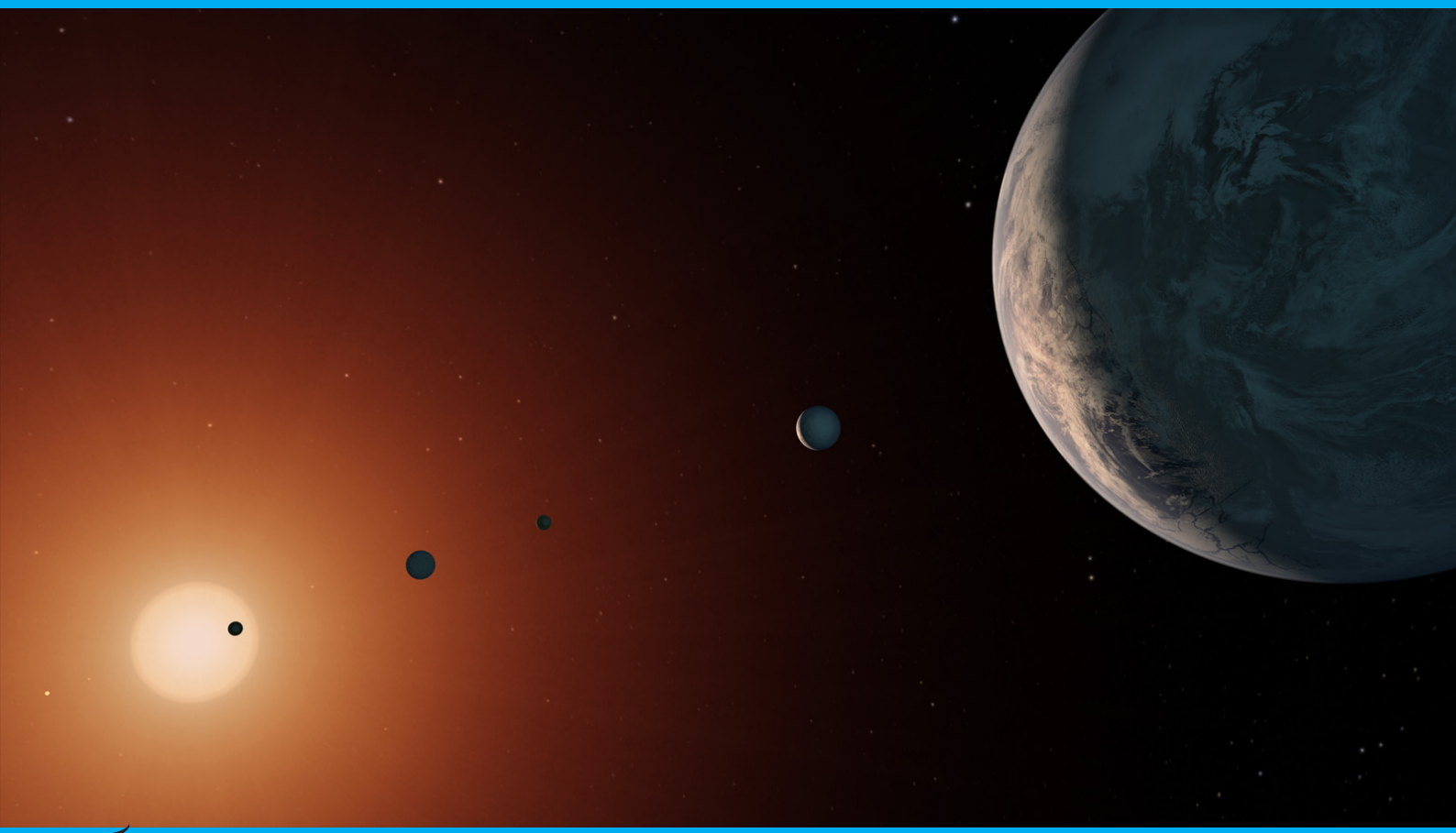

TU Delft

# Flux and polarization signals of the Trappist-1 system

## Numerical simulations

by

Fouad Abiad

to obtain the degree of Master of Science
at the Delft University of Technology,
to be defended publicly on Tuesday April 28, 2020.

Student number: 4744470
Thesis committee: Dr. D. M. Stam, Delft University of Technology, Supervisor
Dr. L. L. A. Vermeersen, Delft University of Technology
Dr. A. Endo, Delft University of Technology

An electronic version of this thesis is available at http://repository.tudelft.nl/.

*Cover page image: artist's impression of the Trappist-1 system, retrieved from NASA.*

TU Delft

# Abstract

The Trappist-1 system consists of an M-dwarf star and seven known planets tightly orbiting it, located 39 light years away from Earth. The system is interesting due to how closely the planets are orbiting their parent star, in addition to the likelihood of one of its planets containing surface water, a crucial component for life. The system has been the subject of many studies concerning atmospheric predictions and polarimetric modeling. However, these did not explore phenomena such as the atmospheric composition and its effect on the polarization signals, having a patchy cloud cover, and the eclipse of the planets behind their parent star. In this work, we present the phase curves of the polarized flux and degree of polarization of the individual Trappist-1 exoplanets, as well as the entire system including the star. A polarimetric accuracy of about 0.1 parts per million is required to detect the Trappist-1 system when its planets are non-cloudy, and an accuracy of about 1 part per million is required when all its planets are fully cloudy. In addition, we investigate the observability of a surface ocean on one of the system planets, and we present a way to detect its presence. For our chosen surface and atmospheric properties, the presence of an ocean is best observed when the cloud cover is 0%, requiring a polarimeter precision of nearly 40 parts per billion. We conclude that in the near future, the flux reflected by the Trappist-1 system, as well as the presence of oceans on its planets, could potentially be observed.

Delft, April 2020

# Contents

# 1

# Introduction

The Trappist-1 system consists of a red dwarf star and seven planets (1b, 1c, 1d, 1e, 1f, 1g, and 1h), discovered in 2015 by Gillon et al. by the transit method using the ground-based TRAPPIST telescope (TRAnsiting Planets and PlanetIsimals Small Telescope) [11]. These planets are approximately Earth-sized and orbit their parent star in tight orbits. It is the first dwarf star that has several planets cool enough to possibly form condensate clouds [60].

Polarimetry is a powerful technique for enhancing the contrast between a star and an exoplanet, with the reasoning that when integrated over the stellar disk, direct light of a solar-type star is considered unpolarized [64]. Starlight reflected by a planet will usually be polarized because it was scattered within the planet's atmosphere and/or because it was reflected by the surface [64]. Polarimetry helps planet detection because, integrated over the stellar disk, direct starlight (which is considered unpolarized) will become polarized upon reflection by the planet [66]. This direct observation of planetary radiation enables the detection of exoplanets that are not easily found with the currently used indirect detection methods, like not-so massive planets or ones in large orbits [66]. For instance, a planet can be observed by imaging a suspect planetary system in two perpendicular polarization directions; since the starlight is unpolarized, it will be equally bright in both images, while the polarized source (a planet) will show up in the difference between images [66].

In addition, polarimetry can be used for characterizing exoplanets as their degree of polarization (as a function of wavelength and/or planetary phase angle) is sensitive to the structure and composition of the planetary atmosphere and surface; this has been used for remote-sensing of planets, such as Venus and Neptune [64]. Characterizing a planetary atmosphere means deriving its chemical composition, size, and spatial distribution of its atmospheric constituents like cloud particles, which requires observing the thermal radiation the planet emits and/or the stellar light it reflects directly [66].

Examples of ground-based telescopes that use polarimetry for exoplanets include PlanetPol, whose aim was to detect spatially unresolved gases, and SPHERE, aiming to detect spatially resolved gaseous exoplanets, hosting the ZIMPOL polarimeter, which determines the size of some exoplanets [55, 64]. Other polarimeters include SPEXone and HARP-2 on-board the upcoming PACE satellite that will characterize aerosols on Earth, the upcoming Moon-based LOUPE instrument, aiming to characterize Earth's disk-integrated linear polarization spectrum [19], and the POLLUX spectro-polarimeter on-board the proposed LUVOIR mission to characterize habitable exoplanets [45]

Which polarization features can be observed rely greatly on the telescope and instrument characteristics (i.e., size, optical design, polarimetry method, detector properties, spectral resolution), integration time, and on the planetary system properties such as size, stellar type and age, orbital distance, and the planet-observer distance [64]. High polarimetry accuracy is needed to detect a planet's signal, even if the starlight reflected by a planet is strongly polarized, as it will be superposed on a background of unpolarized stellar light [64]. Degrees of polarization that can be measured for instance include PlanetPol, having a photon-noise-limited precision of $10^{-6}$, and SPHERE's polarimeter reaches $10^{-5}$ [64]. Note that this implies the instrument can distinguish one polarized photon out of $10^{6}$ unpolarized photons,

for PlanetPol [64]. The calculated degree and direction of polarization are useful for designing and building polarimeters for exoplanet research, in addition to aid in designing instruments that measure exoplanet fluxes only, as these instruments' optical components are sensitive to the observed light's state of polarization [64].

Another reason to include polarization in numerical simulations of reflected light is that neglecting it induces errors in fluxes and albedo by extension, as light is fully described by a 4-by-1 vector, and a scattering process is only fully described by a 4-by-4 matrix [64]. So, the flux resulting from the scattering of unpolarized light differs from that of scattering of polarized light, as the unpolarized starlight incident on a planet is usually polarized upon its first scattering, so higher orders of scattering induce errors in the fluxes when polarization is neglected [64]. For instance, for gaseous exoplanets, neglecting polarization causes flux errors reaching $10\%$ [64].

As such, in this work, we present results of numerical simulations of the total flux and polarization signals for the Trappist-1 system for various atmospheric configurations.

Trappist-1 has been the focus of many recent works. Most relevant to our study are the studies analyzing the system from a polarimetric viewpoint, particularly that of Kopparla et al., who modeled the expected polarimetric signals of the system [33]. This will be the subject of scrutiny later in this report.

While it bears a resemblance to the work of Kopparla et al., our work is novel as it considers various atmospheric compositions and cloud coverages, the eclipsing effect of planets, realistic orbital ephemerides, and a flexible choice of wavelength to view the ocean glint.

In the near future, the James Webb Space Telescope (JWST) will observe the Trappist-1 system and will use transit spectroscopy to characterize the planets and their atmospheres. As for observing the system by its reflected starlight, there are no current missions planning to perform this task; however, this is becoming more and more of a possibility given advancements in technology and improvements in the sensitivity of polarimeters.

## 1.1. Detection and Missions

Small planets, about Earth-size and smaller, are very challenging to characterize, primarily because of their small transit depths, decreasing the feasible precision for transit and eclipse observations [43]. While atmospheres of giant planets will be detectable around sun-like stars with the James Webb Space Telescope (JWST) [14], the atmospheres of Earth-sized planets will not be [43]. However, the atmospheres of small planets orbiting some of the smallest, closest stars will be readily detectable; these include previously-detected Earth-sized planets that are amenable to atmospheric characterization (all seven Trappist-1 planets, GJ 1132b, and LHS 1140b) [43]. These will be extensively studied with JWST, and the knowledge gained from them will be used as the basis for exo-Earths, until large-aperture telescopes capable of directly imaging earths around sun-like stars are launched [43].

Recent observations of the Trappist-1 system were done by the Kepler Space Telescope mission K2 [37] as well as by the Spitzer telescope [15], where the radial velocity technique was used to measure the planet masses [15].

Transiting habitable Super-Earths around small and cool M-dwarf stars are easier to detect than other habitable planets of the same stellar brightness, due to their favourable star-planet contrast [7, 38]. The hotter the planet, the fewer eclipse observations are needed, so 1b needs the least and 1h the most observations [43].

The number of transits required to detect a planet's atmosphere is affected by pressure [43]. For $P < 1$ bar, the required number of transits needed to detect atmospheres doubles every time the pressure drops by a factor of ten [43]. Planets with $P < 0.1$ bar are easier to detect because the blackbody flux from the surface dominates the emission spectrum, and spectral features are weak; however, this makes it harder to accurately characterize the atmospheric composition [43].

Trappist-1 planets are suited for detailed atmospheric characterization, especially by transmission spectroscopy, because transit signals are inversely proportional to the host-star radius, the latter being

only 12% the Sun's for Trappist-1 [11]. As such, Super-Earths are the main target for characterizing atmospheres of terrestrial exoplanets in near future missions [7]. These planets allow to test planet formation, evolution, and atmosphere properties for conditions that are unparalleled in the solar system [7]. Therefore, all seven Trappist-1 planets should be amenable to further characterization by the James Webb Space Telescope [70]

Recent missions like TESS and upcoming missions like CHEOPS, PLATO, and JWST, in addition to ground-based surveys, are expected to obtain candidates for the characterization of Super-Earths around bright nearby stars [7].

The structure of this thesis is as follow. In Chapter 2, we provide background information on the Trappist-1 system, focusing on the properties that are important for our numerical simulations. In Chapter 3, we describe our numerical method to compute the total fluxes and polarization that is reflected by the planets of the Trappist-1 system. In Chapter 4, we present the results of our numerical simulations for the individual planets and for the system as a whole. Chapter 5 contains the conclusions, and Chapter 6, finally, our suggestions for future work.

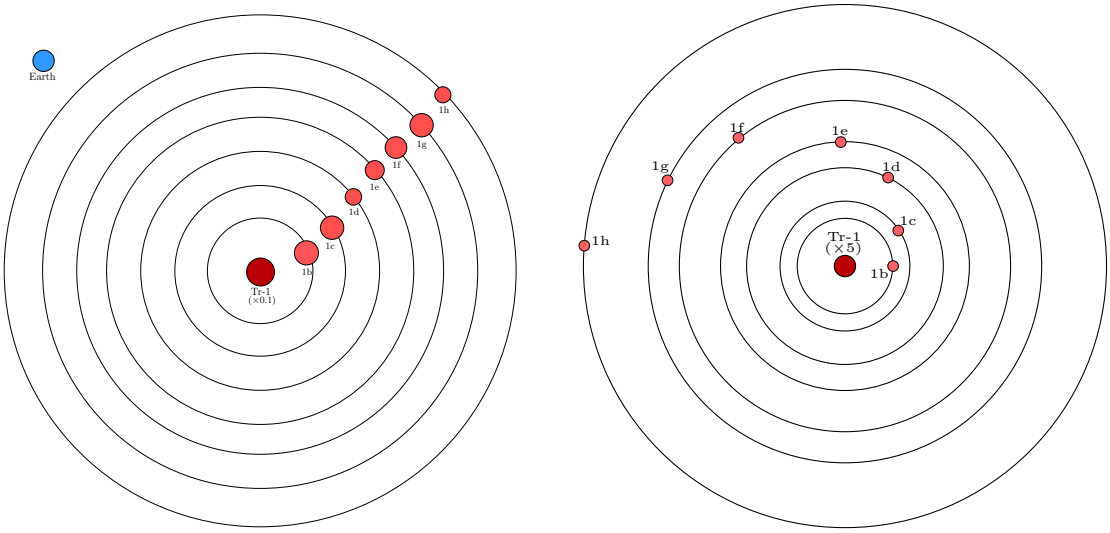


(a) Trappist-1 planet sizes. Orbits not to scale. Earth size for reference.

(b) Trappist-1 planet orbits. Planet sizes not to scale.

Figure 1.1: The Trappist-1 system: planet sizes and orbits, using data from Table 2.1

# 2

# The Trappist-1 System

In this chapter, we describe the Trappist-1 planetary system. In order to accurately model the signals of the system, the properties of its planets should also be accurate. Therefore, in this section we consider physical phenomena that help in determining which scenarios are most likely to occur. We base out conclusions on the available literature on the matter, rather than make our own model. By the end of this chapter, we aim to have established a slew of possibilities of atmospheric and surface properties for the Trappist-1 planets.

The Trappist-1 system was discovered by Gillon et al. in 2015 using the ground-based Trappist telescope system [11]. It comprises an ultra-cool M-dwarf star (called Trappist-1) and seven Earth-sized planet. With increasing distance from the star Trappist-1, the planets are usually referred to as Trappist-1b, c, d, e, f, g, and h. The planets were discovered using the transit method, and their masses and radii were estimated obtained using the transit method by the Spitzer telescope [15]. The system is located 12 parsecs (or $3.7 \times 10^{14}$ km) away from Earth [11], and the star has an estimated surface temperature of $2511 \pm 37$ K [9]. The characteristics of Trappist-1 and its planets are presented in Table 2.1.

The aim of this thesis research is to compute the flux and polarization signals of the Trappist-1 system, and to do this, we need information about the composition and structure of the planets' surfaces and atmospheres. The planets have been discovered through their transits, and apart from their distances to their parent star, and their sizes and masses, no measured data is available regarding their surfaces

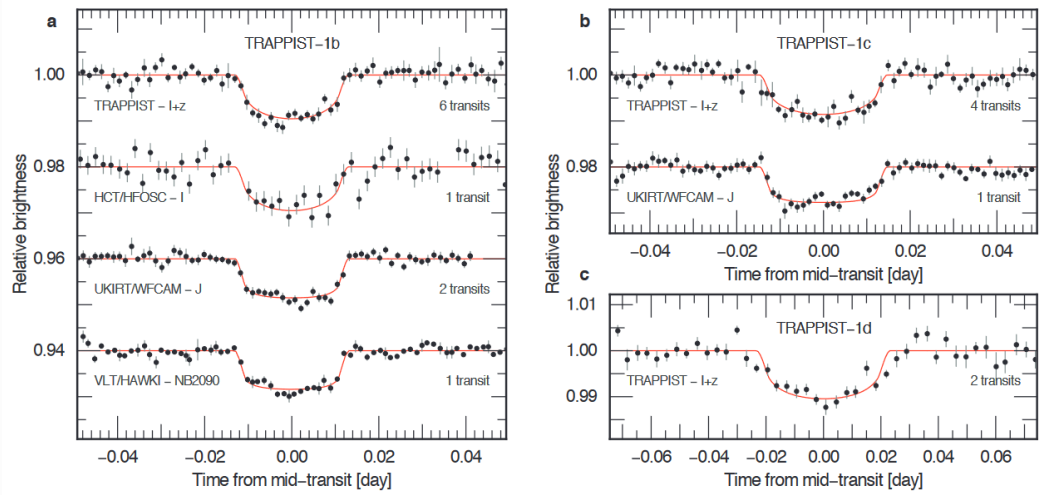


Figure 2.1: Transit photometry of the Trappist-1 planetary system showing the transits of planets 1b, 1c, and 1d, as measured by the Wide-Field infrared CAMera (WFCAM) on the UKIRT telescope in Hawai'i, and the High-Acuity Wide-Field K-band Imager (HAWK-I) on the VLT telescope in Chile [11]

and atmospheres, only numerically model simulations. These will be discussed in Sect. 2.2. Because the light the planets reflect depends on the stellar light that is incident on them, and because the planets are in tight orbits around their parent star and any future observations will thus include the light of the star, the properties of Trappist-1 are also important. These will be discussed next, in Sect. 2.1.

## 2.1. M-dwarf star Trappist-1

Trappist-1 is a so-called M-dwarf star, which is not to be confused with red giants or red super-giants. The properties of this star, as far known, are listed in Table 2.1. M-dwarfs are low-mass stars, with low photospheric temperatures, and constitute about 75% of the main sequence stars [24, 77]. They have a low fuel burning rates, giving them long lifetimes; this should allow their planets to evolve over long timescales, which might be advantageous for habitability [61]. M-dwarfs emit strongly in the near-InfraRed (IR) wavelength range, at which wavelengths $CO_2$ and $H_2O$ in planetary atmosphere are strong absorbers, and would increase a planetary temperature, if present [61]. As a result, planets around M-dwarfs might be more resistant to global-scale glaciation, and may have more stable climates over long timescales, which could be advantageous for biological evolution [61].

We are interested in computing the light of Trappist-1 that is reflected by its planets. Therefore, we need to compute the stellar flux that is incident on each planet and its wavelength dependence. Furthermore, any future observation of the system will include the light of Trappist-1. Thus when modelling future observations, the stellar flux and its wavelength dependence also have to be known. We approximate the flux of Trappist-1 using a black-body approximation. The radiation $B_\lambda$ that a black body emits is given by Planck's law [2]:

$$B_\lambda(\lambda, T) = \frac{2hc^2}{\lambda^5} \cdot \frac{1}{e^{\frac{hc}{\lambda k_B T}} - 1} \tag{2.1}$$

With $B_\lambda$ $[W/(sr \cdot m^2 \cdot m)]$, the body's surface brightness, $h = 6.626 \times 10^{-34}\ J \cdot s$, Planck's constant, $k_B = 1.380649 \times 10^{-23}\ J/K$, Boltzmann's constant, $c = 2.998 \times 10^8\ m/s$, the speed of light, $\lambda$ $[m]$, the wavelength, and $T$ $[K]$, the stellar surface temperature. Figure 2.2 shows the Planck curve for Trappist-1 as computed by Eq. 2.1 and assuming a temperature of 2511 K [9]. It should be noted that a star's spectrum is not perfectly described by one Planck function as the star's temperature varies with depth, so the actual stellar flux would be described by many Planck functions. Furthermore, absorbing gases in the stellar atmosphere would leave spectral lines in the spectrum. For M-dwarfs, the absorption spectra contain oxygen molecules, such as titanium oxide (TiO) and vanadium oxide (VO) [57].

The stellar surface flux or flux density $F$ or $\pi B_\lambda$ $[W/(m^2\ m)]$ is obtained by integrating the radiation emitted by the star $B_\lambda$, across all emission directions. This is given by the following equation [65]

$$F(T) = \int_0^{2\pi} \int_0^1 B_\lambda(T)\ \cos\theta\ d\cos\theta\ d\phi = 2\pi\ B_\lambda(T) \int_0^1 \cos\theta\ d\cos\theta = \pi B_\lambda \tag{2.2}$$

$\phi$ is the azimuth angle and $\theta$ is the emission angle with respect to the vertical axis.

The flux $F$ $[W/(m^2\ m)]$ is obtained by integrating over all wavelengths [65]

$$F(T) = \int_0^\infty F_\lambda(T)\ d\lambda = \pi \int_0^\infty B_\lambda(T)\ d\lambda = \sigma\ T^4 \tag{2.3}$$

A spherical black body with radius $R$ $[m]$ and surface temperature $T$ $[K]$ emits a total flux, or luminosity, $L$ $[W]$ given by [65]

$$L(T,\ R) = 4\ \pi R^2\ F(T) = 4\ \pi R^2\ \sigma T^4 \tag{2.4}$$

For a surface temperature of 2511 K, and using Eq. 2.4, the luminosity of Trappist-1 is $L = 2.00 \times 10^{23}\ W$, while that of the sun given a surface temperature of 5778 K is $L = 3.84 \times 10^{26}\ W$. So the luminosity of Trappist-1 is $5.2059 \times 10^{-4}$ times that of the sun, which agrees well with the benchmark value of $5.22 \times 10^{-4}$ [72].

From Eq. 2.1, we compute the maximum $B_\lambda$ occurs at $\lambda = 1.154\ \mu m$, for which Trappist-1 emits most of its flux ($4.088 \times 10^{11}\ W/[m^2 \cdot m]$). For comparison, our Sun emits most of its flux around 0.48 $\mu$m. For future observations of starlight that is reflected by the planets around Trappist-1, it is best to select a wavelength at which $B_\lambda$ is maximum, to maximize the observable flux (this could of course also depend on absorbing gases in the planetary atmosphere). Depending on the spectral bandwidth of the instrument that would be used for such observations, the reflected flux should be integrated over the appropriate wavelength region, taking into account the instrumental response function.

Because of the very small stellar flux at short wavelengths, Rayleigh scattering, which is inversely proportional to $\lambda^4$, never becomes an important factor in the atmosphere of a planet around the star [31]. Combined with the high near-IR absorption by the planet's atmosphere if it contains $CO_2$ and/or $H_2O$, yields extremely low planetary albedos [31].

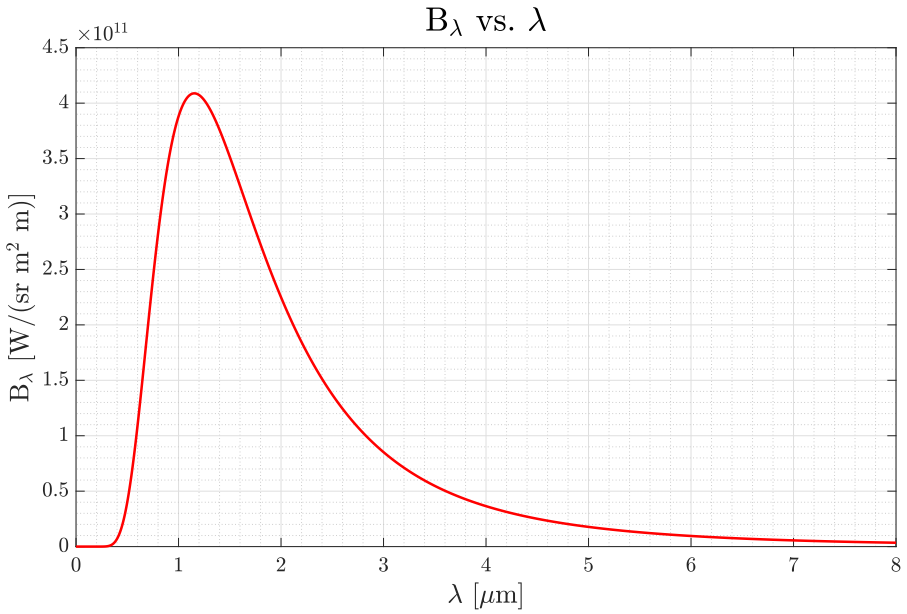


Figure 2.2: The computed Planck curve for the Trappist-1 star, assuming an effective temperature of 2511 K [9]. The maximum flux is emitted at $\lambda = 1.154\ \mu$m.

## 2.2. The Trappist-1 planets

Because the Trappist-1 planets have been found through the transit method, and not through e.g. direct imaging, we have no actual information about the composition and/or structure of their atmospheres nor on the properties of their surfaces (assuming they have solid surfaces since they are Earth–sized). Table 2.1 lists the properties as far as we know them. For computing the flux and degree of polarization of the starlight that these planets reflect, we need to know for every planet: the surface composition (albedo, reflection properties), the atmospheric gas composition, the surface pressure, the properties of clouds and hazes (composition, altitude, amount of cloud coverage and cloud locations, particle column number density and particle microphyiscal properties).

Below, we present and discuss the atmospheric and surface properties that have been proposed for the individual Trappist-1 planets.

Our knowledge and predictions of the Trappist-1 planets and their atmosphere are based off the works of people who accurately modeled these. For instance, Wolf assessed the Trappist-1 planets' possible climate and habitability using a 3D atmospheric climate model (which includes a radiative transfer code), assuming all the planets are covered by a 50 m deep ocean, and included clouds and convection [76]. They concluded that planets 1b, 1c, and 1d are probably too hot to sustain surface liquid water, while 1f, 1g, and 1h are likely too cold to sustain surface liquid water, and finally, 1e is the best bet for a

| **Star** | **Trappist-1** | | | | | | |
|---|---|---|---|---|---|---|---|
| Mass $M_*$ $[\times 10^{-2} M_{sun}]$ | $8.90 \pm 0.7$ | | | | | | |
| Radius $R_*$ $[R_{sun}]$ | $0.1210 \pm 0.003$ | | | | | | |
| Density $\rho_*$ $[\rho_{sun}]$ | $51.1^{+1.2}_{-2.4}$ | | | | | | |
| Luminosity $L_*$ $[\times 10^{-4} L_{sun}]$ | $5.22 \pm 0.19$ | | | | | | |
| Effective Temperature $T_{eff}$ $[K]$ | $2511 \pm 37$ | | | | | | |
| **Planet** | **1b** | **1c** | **1d** | **1e** | **1f** | **1g** | **1h** |
| Mass $m$ $[M_e]$ | 1.017 | 1.156 | 0.297 | 0.772 | 0.934 | 1.148 | 0.331 |
| Radius $R$ $[R_e]$ | 1.121 | 1.095 | 0.784 | 0.910 | 1.046 | 1.148 | 0.773 |
| Density $\rho$ $[\rho_e]$ | 0.726 | 0.883 | 0.616 | 1.024 | 0.816 | 0.759 | 0.719 |
| Surface gravity $g$ $[m/s^2]$ | 0.812 | 0.966 | 0.483 | 0.930 | 0.853 | 0.871 | 0.555 |
| Semi-major Axis $a$ $[\times 10^{-3} AU]$ | 11.548 | 15.82 | 22.28 | 29.283 | 38.534 | 46.877 | 61.935 |
| Eccentricity $e$ $[\times 10^{-2}]$ | 0.622 | 0.654 | 0.837 | 0.510 | 1.007 | 0.208 | 0.567 |
| Argument of Perigee $\omega$ [°] | 336.86 | 282.45 | −8.73 | 108.337 | 368.81 | 191.34 | 338.92 |
| Mean Anomaly $M$ [°] | 203.12 | 69.86 | 173.92 | 347.95 | 113.61 | 365.08 | 269.72 |
| Equilibrium Temperature[a] $T_{eq}$ $[K]$ | 391.5 | 334.8 | 282.1 | 246.1 | 214.5 | 194.5 | 169.2 |
| Orbital inclination $i$ [°] | 89.56 | 89.70 | 89.89 | 89.736 | 89.719 | 89.721 | 89.796 |
| Orbital Period $P$ $[day]$ | 1.511 | 2.422 | 4.005 | 6.099 | 9.206 | 12.354 | 18.768 |
| Irradiation $S_p$ $[S_e]$ | 3.88 | 2.07 | 1.043 | 0.604 | 0.349 | 0.236 | 0.135 |

[a] Each equilibrium temperature $T_{eq}$ has been computed assuming a planetary Bond albedo of zero.

Table 2.1: Characteristics of the Trappist-1 planetary system taken from Grimm et al. and Delrez et al. [9, 15]. The subscript $X_{sun}$ is for the sun, and $X_*$ is for Trappist-1. Note that $M_{sun} = 1.988 \times 10^{30}$ kg, $R_{sun} = 695700$ km, $\rho_{sun} = 1408\ kg/m^3$, $L_{sun} = 382.8 \times 10^{24}$ W, $S_e = 1360$ W/m$^2$ [74, 75].

habitable ocean-covered world in the Trappist-1 system [76].

Turbet et al. derived theoretical mass-radius relationships for rocky Trappist-1 planets, assuming the planets have water-rich atmospheres and are more irradiated than the runaway greenhouse limit, using a 1D numerical radiative-convective climate model, coupled with mass-radius relationships of rocky interiors [70].

Morley et al. modeled transmission and thermal emission spectra for the planets, for a variable atmospheric composition and surface pressure [43]; they used the planets' characteristics at the time of discovery and use a set of simple analytic equations (rather than radiative transfer models), assuming an isothermal pressure-temperature profile, to model the planets' atmospheric profiles. In addition, they used a chemical equilibrium applications model to compute thermo-chemical equilibrium molecular mixing ratios to calculate the gas abundances along each profile [43]. For instance, Fig. 2.3 is an example of a pressure-temperature profile for the Trappist-1 planets that Morley et al. modeled.

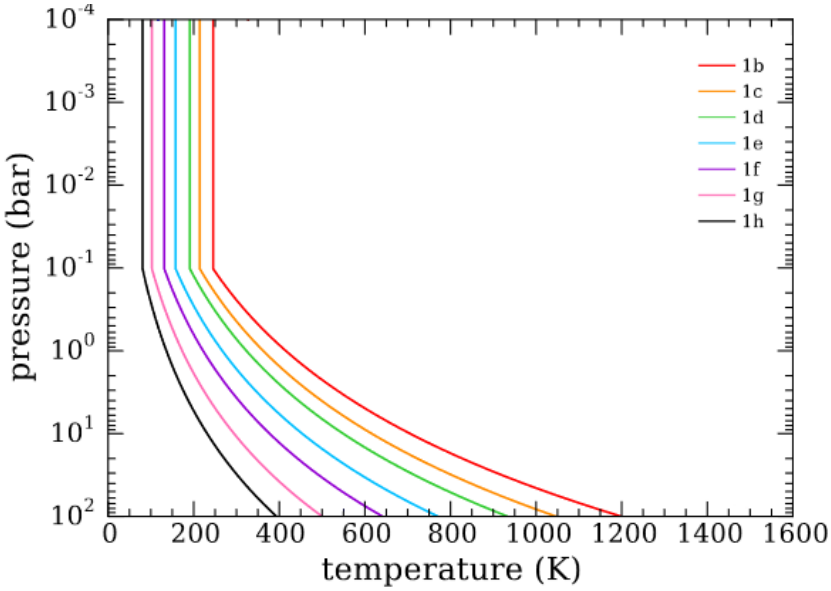


Figure 2.3: Example of model pressure-temperature profiles for Trappist-1 planet atmospheres. This example assumes the planets have a surface pressure of 100 bar and Venus-like composition, with an isothermal atmospheres. From Morley et al. [43]. Edited for readability and to include Trappist-1 planets only.

The properties of the Trappist-1 planets are listed in Table 2.1, and are summarized here for convenience:

**Planet Trappist-1b** is the closest planet to Trappist-1, at a distance of 0.0115 AU and an orbital period of 1.5 days. Assuming no heat processes other than stellar flux, it is the hottest planet in its system, at an equilibrium surface temperature of $391.5$ K. It is approximately Earth-sized in both mass ($1.017\ M_{earth}$), and radius ($1.121\ R_{earth}$).

**Planet Trappist-1c** is the second closest planet to Trappist-1, at a distance of 0.0158 AU and an orbital period of 2.4 days. Assuming stellar flux is the only heat process, it has an equilibrium surface temperature of $334.8$ K. It is also roughly Earth-sized in both mass ($1.156\ M_{earth}$), and radius ($1.095\ R_{earth}$).

**Planet Trappist-1d** is the third closest planet to Trappist-1, and possibly the innermost planet in its habitable zone, at a distance of 0.0223 AU and an orbital period of 4 days. Assuming stellar flux is the only heat process, it has an equilibrium surface temperature of $282$ K. It the lightest planet in its system ($0.297\ M_{earth}$), and the second smallest planet ($0.784\ R_{earth}$).

**Planet Trappist-1e** it is the fourth closest planet to Trappist-1, and possibly the central planet in the system's habitable zone, at a distance of 0.0293 AU and an orbital period of 6 days. Assuming stellar flux is the only heat process, it has an equilibrium surface temperature of $246$ K. This planet likely possesses surface water, making it very interesting in terms of habitability. It has a mass of $0.772\ M_{earth}$ and a radius of $0.910\ R_{earth}$.

**Planet Trappist-1f** is the third outermost planet to Trappist-1, and possibly the outermost planet in its habitable zone, at a distance of 0.0385 AU and an orbital period of 9.2 days. Assuming stellar flux is the only heat process, it has an equilibrium surface temperature of $214$ K, and it is nearly Earth-sized in both mass ($0.934\ M_{earth}$) and radius ($1.046\ R_{earth}$).

**Planet Trappist-1g** is the second outermost planet to Trappist-1, at a distance of 0.0469 AU and an orbital period of 12.4 days. Assuming stellar flux is the only heat process, it has an equilibrium surface temperature of $195$ K, and it is nearly Earth-sized in both mass ($1.148\ M_{earth}$) and radius ($1.148\ R_{earth}$).

**Planet Trappist-1h** is the outermost planet to Trappist-1, at a distance of 0.0619 AU and an orbital period of 18.8 days. Assuming stellar flux is the only heat process, it has an equilibrium surface

temperature of $169$ K. It is the second lightest planet ($0.331\ M_{earth}$) and the smallest in the system ($0.773\ R_{earth}$).

### 2.2.1. Concepts

#### Tidal Locking

Planets (moons) orbiting close enough to their host star (planet) can have the differential gravity across their diameters produce an elongated shape with bulges, which are prevented from aligning perfectly with the star due to frictional forces in the planet, resulting in torques altering the planet's rotation, fixing the rotation rate at a specific frequency; this process is called tidal locking [3].

Lower mass stellar hosts, such as late M-dwarfs ($\leq 0.1 M_{sun}$ like Trappist-1), induce stronger tidal effects on potentially habitable planets, making them very likely to be circularized within short timescales, so locking is possible for most planets in the HZ of M-dwarfs [3].

#### The Greenhouse Effect

The main source of heat to Earth is solar energy, which is transmitted from the sun to Earth by radiation, then converted to heat at the surface; to balance this input of radiation, Earth emits radiation back to space, some of which is trapped by greenhouse gases and re-radiated back to Earth, resulting in the warming of the surface; this is called the *greenhouse* effect [23]. This trapping of terrestrial radiation by naturally occurring greenhouse gases is essential for maintaining the Earth's surface temperature above freezing point [23].

*Greenhouse gases* are gases in the atmosphere that absorb and emit radiation in the IR range, which is the wavelength range emitted by Earth's surface, its atmosphere, and its clouds [22]. Water vapor ($\mathrm{H_2O}$), carbon dioxide ($\mathrm{CO_2}$), methane ($\mathrm{CH_4}$), nitrous oxide ($\mathrm{N_2O}$), and ozone ($\mathrm{O_3}$) are the primary greenhouse gases in Earth's atmosphere [22]. The major atmospheric constituents for Earth like nitrogen ($\mathrm{N_2}$) and oxygen ($\mathrm{O_2}$) are not greenhouse gases because diatomic molecules like $\mathrm{N_2}$ and $\mathrm{O_2}$ have no net change in their electrical charge distribution when they vibrate [4]. For reference, the main contributions to Earth's greenhouse effect are by water vapor (50%), clouds (25%), $\mathrm{CO_2}$ (19%), and minor greenhouse gases (7%) [56]. Water vapor is the most important greenhouse gas present in Earth's atmosphere; its evaporation into the atmosphere generates a positive greenhouse feedback, where the increase in water vapor amplifies the greenhouse effect, warming up more water vapor, adding more greenhouse gas [23].

#### Clouds

The presence of clouds is instrumental in shaping the polarimetric signals, thus this section serves to introduce them and outline their effects. We are most interested in cumulus clouds, as they are associated with the presence of water and are thick enough to induce a sizeable effect on the system's polarimetry.

Clouds are visible bodies formed by ascended damp air, and exist in the atmosphere of planets or similar bodies, such as Earth [20, 59]. They are solid or liquid particles resulting from condensation processes due to temperature and pressure conditions of the atmosphere, while aerosols and haze are particles of any size and kind suspended in the atmosphere [42, 59]. Haze on the other hand, consists of very small, photochemically-produced, opaque solid particles suspended in the atmosphere that diminish visibility [42, 59]. Clouds have a composition varying from body to another; for instance, Earth clouds are mainly water ($\mathrm{H_2O}$) [59]. Clouds and/or haze are present in the atmosphere of every solar system planet, and are expected to be present in exoplanet atmospheres [18].

Clouds are classified based on the type of ascending motion that formed them; for our interests, cumulus clouds are formed by convective processes, or parcels that rise above their lifted condensation level [20, 67]. Clouds have a large impact on terrestrial planet atmospheres and greatly alter the atmospheric radiation balance, dynamics, and vertical transport of other gases and aerosols [20, 59]. For Earth, there are low- and high-level clouds, where low ones are water droplet clouds, and high ones are made of water ice [28].The optical properties depend on the cloud phase (liquid or ice), water

content, and average cloud particle size [20]. The overall feedback effect of clouds on the surface temperature can be positive or negative; for low clouds, the reflectivity effect dominates, so they cool the Earth-atmosphere system, while for high clouds, the blanketing effect dominates, so they warm the system [20].

Assessing the role of clouds in a planetary atmosphere requires knowing the altitude (or pressure) at cloud-top and bottom, the optical thickness, and the cloud particles' micro-physical properties (i.e., composition, size, shape and thermodynamic phase), refractive index, surface albedo, surface pressure, mean molecular mass, gravitational acceleration, particle effective radius, variance, and depolarization factor [26, 52].

For exoplanets, on which they are expected to exist, clouds add color to a planet when viewed from afar but pose an issue for exoplanet observations: on one hand, their existence can give clues about the planet's atmosphere, while on the other they: 1) complicate exoplanet data interpretations by blocking the atmosphere below and weaken the planet's spectral features [59], and 2) scatter and absorb incident starlight and the planet's thermal radiation, influencing the surface temperature and climate (and by extension, the presence of liquid water on the planet) [52, 59].

In short, clouds influence a planet's atmosphere by scattering or absorbing incident radiation, changing spectral features, and by altering the radiation budget through forming and precipitating. For exoplanets, clouds give cues about their atmosphere, but they obstruct data collection and are tougher to model than atmospheres, in part due to clouds' morphology, which affects their radiative properties [51].

The cloud cover or coverage is the ratio of total projected cloud area over the total area, and is computed in either the horizontal or vertical direction (horizontal cover $\leq$ vertical cover) [51]. The cloud cover and thickness of high- and low-level clouds may greatly influence the radiative balance of the planet and its temperature [73]. As such, a cloud's net heating or cooling effect depends on its temperature [23]. A low cloud's temperature is close to the surface due to convective heat transport, so it radiates about the same energy as the surface did prior to the cloud forming, causing little greenhouse warming [23].

#### Planetary Rotation

A planet's rotation rate, not orbit, is discussed here. The term 'zonal' will be used to refer to a circulation or pattern along latitudinal lines/circles.

Planetary rotation is an important parameter in regulating atmospheric and oceanic heat flow, cloud formation and determining the spatial pattern of clouds [78], and is divided into many ranges: very fast rotation ($p_{rot} \lesssim 1\ day$), fast rotation ($p_{rot} \lesssim 6\ days$), slow rotation ($p_{rot} \gtrsim 6\ days$), and very slow rotation ($p_{rot} \gtrsim 30\ days$) [7].

Planetary rotation rate greatly affects the climate of Earth-like planets; a slow rotation weakens the Coriolis effect and causes the atmospheric circulation to shift from a rapidly rotating regime characterized by zonal uniformity and symmetry about the equator (like Earth), to a slowly rotating regime characterized by dayside to nightside heat transport and circular symmetry about the substellar point [30]. An example of such would be planets near the inner edge of an M-dwarf's HZ, like 1d [30]. For slow and synchronously rotating Earth-like planets expected around low-mass stars, if global mean temperatures exceed $310\ K$ (which 1b and 1c do, see Table 2.1), then increasing water vapor causes both strong solar absorption and inefficient radiative cooling in the low atmosphere, resulting in net radiative heating of the layers above the surface; this forms a thermal inversion, which is stable against deep convection, prohibiting the formation of convective clouds [30]. On the other hand, fast rotators like present-day Earth and Trappist-1d exhibit zonal patterns of temperature and clouds These feature the fewest clouds, so reach Earth-like temperatures at relatively low values of the incident stellar flux [30].

### 2.2.2. Discussing the Effects

This section discusses the various atmospheric and surface possibilities of the Trappist-1 system, featuring the previously-mentioned phenomena, to survey its planets' most likely properties.

If an M-dwarf planet orbits close to its parent star, strong tidal effects may result in capture into resonances in spin-orbit period; this could cause super-synchronous rotation, causing the atmosphere to condense out onto the nightside of M-dwarf planets [61]. Since a star's HZ is contingent on its luminosity, the HZ around M-dwarfs is close to them due to the stars' weak luminosity [21]. As a consequence, exoplanets in this HZ are likely tidally locked to their parent star, whereby their dark side would succumb to atmospheric collapse, which can potentially be prevented by atmospheric heat transport [21]. Furthermore, it is believed that all Trappist-1 planets are tidally locked [12].

At high stellar flux, strong convection produces thick water clouds near the substellar location that greatly increase the planetary albedo and reduce surface temperatures [77]. Higher instellation produces stronger substellar convection and therefore higher albedo, making this phenomenon a stabilizing climate feedback [77]. The stabilizing cloud feedback, which arises from an increase in the planetary albedo due to the presence of thick clouds at the substellar point, can expand the inner HZ to roughly twice the stellar flux for tidally-locked planets around low mass stars [32]. As such, it is expected that tidally-locked planets have more clouds, especially near the substellar point [61].

A planet's magnetic field strength greatly affects its ability to maintain an atmosphere, where this magnetic shield helps regulate the planet's climate, surface temperature, and day-night temperature contrasts [61]. For Trappist-1 planets, which are tidally-locked M-dwarf planets, planetary magnetic moments are weak and thus may not be enough to protect the atmosphere, but M-dwarfs have small coronal mass ejections, so planets can actually retain their atmospheres [61].

#### Oceans

It is believed that planets within M-dwarf systems are likely to contain significantly more water than the Earth or any planetary body in the solar system [71]. The large ocean cover fraction on Earth stabilizes climate over an annual cycle, due to the large effective heat capacity of the atmosphere over the ocean [63]. Planets with small ocean fractions or polar continents can still maintain seasonally and regionally habitable conditions over a larger range of orbital radii than planets that are more Earth-like [63].

Depending on their original water inventory, some Trappist-1 planets could have retained enough water to maintain surface habitability [61].

### 2.2.3. Trappist-1 Planets Climates

This section explores the specific mechanisms and properties of Trappist-1 planets. Neighboring planets are grouped into the same subsection. For continuity and if necessary, the mechanisms and properties of some planets may not be described in their respective subsections.

While the exact limits of a star's HZ vary between sources, it is generally agreed that Trappist-1 has three planets in its HZ, namely 1d, 1e, and 1f, with 1d at its inner edge and 1f at its outer edge [30].

All seven Trappist-1 planets are very likely in synchronous rotation, and it is expected that tidal heating is the dominant process of internal heating for the inner planets (1b, 1c, and 1d), potentially play a role on 1e, and have a much weaker effect on 1f, 1g, and 1h [70].

It is believed that 1b, 1c, 1f, 1g, and 1h are primarily rocky planets, in addition to 1e [8, 70]. The surface albedo of the Trappist-1 planets (excluding 1e) most likely falls in the range 0.2-0.3 [43, 70]. For this albedo range and excluding all heat sources but stellar flux, none of the planets but 1b would have an equilibrium temperature above the boiling point of water, so all but one Trappist-1 planets could be cool enough to host surface liquid water [12]. However, since these planets are so close to their parent star, tidal interactions in the form of tidal heating become crucial to their heat balance [37].

Planets 1b, 1c,and 1d are believed to be too hot to support surface water as they would have undergone a runaway greenhouse process and lost their water throughout [70, 76]. On the other hand, planets 1f, 1g, and 1h might be too cold to support surface water, though if they do contain water, they would probably be encased in ice or snow and would have a pressure of 30 bars of $CO_2$ [76]. However, some speculate that 1d and 1f may have surface liquid water [35], though 1b and 1c are most likely too hot to sustain global liquid water oceans [31]. In addition, due to how close it is to its parent star, 1b exhibits a very high surface temperature, and is very unlikely to produce clouds or aerosols [35].

Trappist-1 planets could still harbor a large variety of atmospheres, such as thick $H_2O$, $CO_2$, $N_2$, or $O_2$ dominated atmospheres [70]. In addition, Grimm et al. considered an $H_2$-$H_2O$ composition for the planets [15]. Since the composition of Trappist-1 planets is not certain as of yet, we will also consider this composition when computing the reflected flux and polarization signals in Section 4.2 (despite the fact that some planets are confirmed to not have an $H_2$-dominated atmosphere, as shown in the following paragraphs).

**Planets 1b, 1c**

1b and 1c are unlikely to have an extended gas envelope as they lie in a region in space where high-altitude cloud/haze formation is not expected to be significant for hydrogen-dominated atmospheres [8]. By comparing masses and radii, Grimm et al. concluded that Trappist-1 planets most likely do not contain more than 5% condensed water mass in their atmosphere, except for 1b and 1d, which have respective probabilities of 70% and 50% of containing $< 5\%$ water mass fraction in their atmosphere [15].

Transit spectroscopy using the Hubble telescope was performed on 1b and 1c and showed that they do not have a cloud/haze $H_2$-dominated atmosphere; this makes sense as $H_2$, one of the lightest materials, would have escaped to space [8, 70]. As such, $H_2$-dominated atmospheres are unlikely for 1b and 1c [8]. These two could possess relatively thick $H_2O$, $CO_2$, $N_2$, or $O_2$ dominated atmospheres, or potentially tenuous atmospheres composed of a variety of chemical species [8]. In addition, the cloud formation efficiency at the irradiation levels of 1b and 1c is small, but possible for a pressure level $p \geq 0.1\ bar$ [8].

**Planets 1d, 1e**

1d, a fast rotator with an estimated orbital period of $\sim 4$ days, receives $\sim 1.1$ times current Earth flux, is likely in a runaway greenhouse state [30]. Considering its proximity to the inner edge of its parent star's HZ, if 1d can sustain a thick water cloud cover near the substellar region, then it could sustain surface liquid water global oceans [70].

1e is akin to the planet Proxima Centauri b, as both are a type of planet that always sustains surface liquid water, and are highly promising for habitability prospects [70]. If 1e is synchronously-rotating and is water-rich, then it should have a patch of liquid water at its substellar point, regardless of its atmosphere or lack thereof, for which the atmosphere would be composed of water vapor [49, 70].

From here on, adding greenhouse gases to the atmosphere would increase the mean surface temperature as well as the size of the liquid water patch [70]. As such, 1e is the only Trappist-1 planet able to host surface liquid water without the need of greenhouse warming from a gas other than $H_2O$, though this requires a sufficient $H_2O$ reservoir covering the whole surface, which cannot be trapped on the nightside [70].

While Turbet et al. mentioned that 1e can sustain at least a patch of water without an atmosphere, it is speculated that the atmosphere of ocean planets could have high $CO_2$ levels because silicate weathering can be ceased by water coverage [70]. On the other hand, $CO_2$ concentrations that are high enough to maintain open water in the outer portions of the HZ might be incompatible with limitations imposed by sea-floor weathering [21]. As $CO_2$ concentration is sufficiently high, ocean heat transport is very efficient in warming the nightside and causing sea-ice melting there [21]. The possibility of having $CO_2$ on 1e was also brought up by Lincowski et al., who claimed that 1e, which resides in the star's HZ, requires much more $CO_2$ than Earth to maintain an Earth-like surface temperature [35].

High-altitude clouds have been suggested for 1d, 1e, 1f, and 1g, for which the cloud-top pressure is $p \leq 0.012\ bar$ (1d and 1e, though are likely un-physical), and $p \approx 0.1\ bar$ (1f and 1g) [42].

**Planets 1f, 1g, 1h**

Given their distance from their parent star, 1f, 1g, and 1h are cold enough to be fully covered by a layer of water ice [70]. These planets are in the transition between slow and fast rotating regimes [70].

As the dominant gas in a planet's atmosphere becomes less volatile, building up an atmosphere becomes more complicated due to atmospheric collapse; this would trigger a positive feedback, because

as the atmosphere condenses, the heat redistribution would become less efficient, leading to even more condensation; this would drive the planets to a complete and irreversible atmospheric collapse [70]. For example, $CO$ and $O_2$, which are a compromise between volatility and abundance, are more condensable gases than $N_2$ and so are expected to collapse for pressures $> 10\ mbar$ [70].

Morley et al. reasoned that since atmospheric composition changes with temperature, the composition of Trappist-1 planets can be matched with their Earth counterpart, based on temperature; for instance, they used the composition of Titan's atmosphere (predominantly $N_2$) as an analog for the coldest planet, 1h [43].

**Carbon Dioxide**

The solar system terrestrial planets are either airless bodies like Mercury, or worlds where carbon dioxide ($CO_2$) is or was abundant in the atmosphere or subsurface, like Earth [70]. Following this logic, Turbet et al. assumed that the four outer Trappist-1 planets (1e, 1f, 1g, 1h) today possess large $CO_2$ quantities in their atmosphere, surface, or subsurface [70]. These have a low internal heat flux due to how far away they are from their parent star, so need to accumulate very large quantities of volatiles on their nightside before a runaway greenhouse process reforms the atmosphere [70].

If the planet initially starts with a thick $CO_2$ atmosphere (i.e., 10 bars), the greenhouse effect and the heat redistribution are efficient enough for the atmosphere to be stable [70]. If however the planet initially starts with little to no atmospheric $CO_2$ and progressively accumulates it in the atmosphere (i.e, by volcanic outgassing), all the additional $CO_2$ would keep condensing on the nightside, so the planet would have a cold and thin $CO_2$ atmosphere [70]. $CO_2$-dominated atmospheres are sensitive to atmospheric collapse, so if 1e, 1f, and 1g have a $CO_2$-dominated atmosphere, it must be very thick [70]. However, these planets (1e, 1f, 1g and 1h), as well as 1d, are unlikely to have an enriched atmosphere (e.g. $CO_2$) above a bare core (assuming a standard Earth-like composition) without invoking unrealistically large quantities of gas [15]. Therefore, these planets are unlikely to have surface liquid water.

**Methane**

Let us assume all Trappist-1 planets had an atmosphere made of methane ($CH_4$), a volatile gas. For the equilibrium temperature of the four outer planets, the $CH_4$ saturation pressure is at $10 - 100\ bar$, so all the methane is expected to vaporize in the atmosphere, if no other component is present [70]. When $CH_4$ is an atmospheric constituent, it influences the planet surface temperature by heating due to the greenhouse effect of tropospheric $CH_4$, and by radiative cooling of stratospheric $CH_4$ [70]. For the spectrum of Trappist-1, $CH_4$ absorbs stellar radiation efficiently around $1.15\ \mu m$ (this is the wavelength at which Trappist-1 emits the most, as per the discussion of Eq. 2.1), warming the upper atmosphere and reducing the short-wave irradiation flux reaching the surface and troposphere, thereby cooling the planetary surface [70]. Despite the cooling effect of $CH_4$, Trappist-1 planets cannot sustain liquid or ice $CH_4$ on their surface, as the surface temperature of these planets greatly exceeds the temperature at which the equilibrium vapor pressure of $CH_4$ occurs, so it cannot condense. Also, methane is prevented from substantially building up in a thick and $O_2$-rich atmosphere as it can easily undergo combustion (following $CH_4 + 2O_2 \rightarrow CO_2 + 2H_2O$) [70]. In addition, photolysis, organic hazes, and their sedimentation help to rapidly deplete atmospheric $CH_4$ [70]. Therefore, we do not expect methane on any of the Trappist-1 planets

**Other Compositions**

Assuming a background atmosphere only made of either $N_2$, $CO$, or $O_2$, none of the Trappist-1 outer planets (1f, 1g, or 1h) can maintain surface liquid water, as they are unable to generate a significant greenhouse effect, and instead need to build up greenhouse gases in their atmosphere, like $CO_2$, $CH_4$, $NH_3$, or $H_2$ [70]. As previously mentioned, 1f and 1g are unlikely to host surface water, while 1e is expected to. As for 1h, regardless of atmosphere, it cannot maintain surface liquid water; for any $CO_2$ atmosphere thickness, it is unable to build up a $CO_2$ atmosphere in the first place due to surface condensation of $CO_2$ (which is expected beyond the orbit of 1g) [70]. For an $N_2/CH_4$ atmosphere, 1h would be unable to have its surface temperature above 160 K, and for an $H_2$ atmosphere (through collision induced absorption), 1h's surface temperature could exceed the melting point of water at $273\ K$, though this composition is highly unlikely [70].

Atmospheres consisting of $N_2$, $CO$, $O_2$ are resistant to collapse, even for synchronously rotating planets, while greenhouse gases ($CO_2$, $NH_3$, $CH_4$) are difficult to maintain in Trappist-1 planet atmospheres: $CO_2$ can easily condense on the permanent nightside, while $CH_4$ and $NH_3$ photo-dissociate rapidly and are hard to accumulate in the atmosphere [70]. On these planets, the surface temperature is extremely low, making volatile species (such as $N_2$, $CH_4$, or $CO_2$) highly sensitive to nightside trapping and potentially atmospheric collapse [70]. For 1f, 1g, and 1h, a pure $N_2$ atmosphere (with $H_2O$ as a variable gas) is quite resistant to atmospheric collapse, unless the $N_2$ partial pressure is below $10\ mbar$ [70].

Observations of terrestrial planets like Earth and Venus were all guided by observations, which do not exist for exoplanets, so there are no existing general cloud models for exoplanets due to how little is known about them; for instance, Batalha et al. assumed a gray opacity source and used a cloud pressure in the range $p = 0.01 - 0.1$ bar [5]. We have shown in Fig. 4.9 and its respective discussion that the cloud pressure does not constitute a large difference in signal, so we decided to keep the cloud pressure more conservative.

### 2.2.4. Summary

In this chapter, we looked into the Trappist-1 system. We covered the star and its spectrum, the planets and their characteristics, introduced physical phenomena that shape the climate of the Trappist-1 planets, and finally, using those phenomena, we discussed what composition, surface features, and atmospheric features we expect on the planets.

The outcome of the discussion is summarized into Table 2.2, which presents a multitude of possibilities for the composition of Trappist-1 atmospheres. The content of these tables will provide the basis for the computations in Chapter 4.

| **Planet** | 1b | 1c | 1d | 1e | 1f | 1g | 1h | Source |
|---|---|---|---|---|---|---|---|---|
| Clouds | | | | | | | | [8, 35, 42] |
| Albedo | 0.2 | 0.2 | 0.2 | 0 | 0.2 | 0.2 | 0.2 | [30, 61, 70] |
| Ocean | | | | | | | | [15, 30, 70, 76] |
| $T_{surf}$ [K] | 391.5 | 334.8 | 282.1 | 246.1 | 214.5 | 194.5 | 169.2 | |
| $P_{surf}$ [atm] | 1 | 1 | 1 | 1 | 1 | 1 | 1 | |
| Pure | | | | | | | | |
| $H_2$ | | | | | | | | [37, 70**?** ] |
| $H_2O$ | | | | | | | | [15, 30] |
| $CO_2$ | | | | | | | | [35, 70] |
| $N_2$ | | | | | | | | [43, 70] |
| $O_2$ | | | | | | | | [8] |
| $CH_4$ | | | | | | | | [35, 70] |
| Composite | | | | | | | | |
| $H_2$ | | | | | | | | [8, 15] |
| $H_2O$ | | | | | | | | [15] |
| $CO_2$ | | | | | | | | [21, 35] |

Red = not feasible, green = feasible, purple = possibly feasible, white = no data

Table 2.2: Table showing the possible Trappist-1 planet scenarios.

# 3

# The Numerical Method

In this chapter, we describe the numerical method we used to perform the computations. First, we define the flux and polarization, then show how those can be computed for a single planet and the whole system, in terms of the atmosphere and surface.

## 3.1. Definitions of flux and polarization

The flux and state of polarization of starlight that is reflected by a planet are described by the following column vector $\mathbf{F}$ [64].

$$\mathbf{F} = [F,\ Q,\ U,\ V]. \tag{3.1}$$

Here, $F$ is the total flux, $Q$ and $U$ describe the linearly polarized fluxes, and $V$ describes the circularly polarized flux. The units of all the vector elements are $W/(m^2\ m)$ [64]. Elements $Q$ and $U$ are defined with respect to a reference plane, chosen to be the *planetary scattering plane*, which passes through the centers of the star, the planet, and the observer [64]. The circularly polarized flux $V$ is very small [52], and will be ignored from hereon. Note that light scattering changes the direction of light propagation without absorption, and may occur by reflection, refraction, or diffraction of the light beam [23]. Also, the scattering efficiency of a particle is the probability that a photon incident on the surface will be scattered [23].

The total and linearly polarized fluxes can be obtained by the following 'measurements' [64]

$$\begin{aligned} F &= F_{0^\circ} + F_{90^\circ} \quad \text{or} \quad F_{45^\circ} + F_{135^\circ} \\ Q &= F_{0^\circ} - F_{90^\circ} \\ U &= F_{45^\circ} - F_{135^\circ} \end{aligned} \tag{3.2}$$

Where $F_{x^\circ}$ is the flux measured through a polarization filter oriented perpendicular to the direction of light propagation, making an angle $x^\circ$ with the reference plane. The angle is measured rotating from the reference plane to the filter's optical axis in the anti-clockwise direction when looking into the direction of propagation of the light [64].

Flux vectors can be redefined from one reference plane to another (i.e., from the scattering plane to a polarimeter's optical plane) by multiplying them with a rotation matrix $\mathbf{L}$ [64]

$$\mathbf{L}(\beta) = \begin{Bmatrix} 1 & 0 & 0 & 0 \\ 0 & \cos(2\beta) & \sin(2\beta) & 0 \\ 0 & -\sin(2\beta) & \cos(2\beta) & 0 \\ 0 & 0 & 0 & 1 \end{Bmatrix} \tag{3.3}$$

With $\beta$ the angle between the two reference planes, measured by rotating in the anti-clockwise direction from the old to the new plane when looking in propagation direction of the light ($\beta \geq 0$) [64]. The direction

of linear polarization with respect to the reference plane, is given by $\chi$ [64], with

$$\tan(2\chi) = U/Q. \tag{3.4}$$

Where $0 \leq \chi \leq \pi$ such that $\cos(2\chi)$ and $Q$ have the same sign [64]. When $\chi = 90°$, $Q < 0$ and the direction of polarization is perpendicular to the reference plane; when $\chi = 0°$, $Q > 0$ and the direction of polarization is parallel to the reference plane [64].

The degree of polarization of the reflected starlight, $P_s$, is independent of the choice of reference plane, and is defined as [64]

$$P = \frac{\sqrt{Q^2 + U^2}}{F}. \tag{3.5}$$

Assuming the planet is mirror-symmetric with respect to the reference plane and that the incoming starlight is unpolarized, flux $U$ (and $V$) equals zero due to the symmetry. In that case, $P_s$ can be re-written as [64]

$$P_{\mathrm{s}} = -\frac{Q}{F} = -\frac{F_{0°} - F_{90°}}{F_{0°} + F_{90°}}. \tag{3.6}$$

The minus sign adds information about the direction of polarization [66]. For $P_{\mathrm{s}} > 0$, the reflected light is polarized perpendicular to the reference plane ($\chi = 90°$), while for $P_{\mathrm{s}} < 0$, the light is polarized parallel to the reference plane ($\chi = 0°$).

## 3.2. Definition of the signals of a single planet

For a spatially unresolved spherical planet with radius $r$ $[m]$, the flux vector **F** of stellar light of wavelength $\lambda$ that is reflected by the planet and that arrives at an observer at distance $d$ $[m]$ ($d \gg r$) can be written as [66]

$$\mathbf{F}(\lambda,\ \alpha) = \frac{r^2}{d^2}\ \frac{R^2}{D^2}\frac{1}{4}\mathbf{S}(\lambda,\ \alpha)\ \pi\mathbf{B}_0(\lambda), \tag{3.7}$$

with $R$ $[m]$ the stellar radius, $D$ $[m]$ the distance between the star and the planet ($D \gg R$), $\alpha$ the planetary phase angle (defined as the star-planet-observer angle), **S** the 4-by-4 planetary scattering matrix, and $\pi\mathbf{B}_0 = [\pi B_0,\ 0,\ 0,\ 0]$ the stellar surface flux [W/(m$^2$ · m)] [64] . Note that when integrated over the stellar disk, M-dwarfs have negligible polarization [41]. For the star Trappist-1, $\pi B_0$ across the desired wavelength range was computed in Ch. 2 and is shown in Fig. 4.1.

Planetary scattering matrix **S** depends on phase angle $\alpha$, on the wavelength $\lambda$, and on the composition and structure of the planetary atmosphere and surface [64]. For a planet that is mirror-symmetric with respect to the reference plane, matrix **S** has the following form:

$$\mathbf{S}(\lambda,\ \alpha) = \begin{Bmatrix} a_1(\lambda,\ \alpha) & b_1(\lambda,\ \alpha) & 0 & 0 \\ b_1(\lambda,\ \alpha) & a_2(\lambda,\ \alpha) & 0 & 0 \\ 0 & 0 & a_3(\lambda,\ \alpha) & b_2(\lambda,\ \alpha) \\ 0 & 0 & -b_2(\lambda,\ \alpha) & a_4(\lambda,\ \alpha) \end{Bmatrix}, \tag{3.8}$$

with $a_1$ the planetary phase function and $b_1$ the polarized phase function. Matrix **S** is normalized such that the average of $a_1$ over all directions equals the planet's monochromatic Bond albedo ) $A_B$ $[-]$, which is defined as the fraction of incident stellar flux that is reflected by the planet in all directions [64]

$$A_B(\lambda) = \frac{1}{4\pi}\int_{4\pi} a_1(\lambda,\ \alpha)\ d\omega = \frac{1}{2}\int_0^{\pi} a_1(\lambda,\ \alpha)\ \sin\alpha\ d\alpha \tag{3.9}$$

with $d\omega$ an element of solid angle.

A planet's monochromatic geometric albedo $A_G$ is the ratio of the flux reflected by the planet at $\alpha = 0°$ to the flux reflected by a Lambertian reflecting[1], white surface subtending the same solid angle on the sky [64].

$$A_G(\lambda) = \frac{F(\lambda,\ 0°)}{F_0(\lambda)}\ \frac{d^2}{\pi r^2} = \frac{1}{4}\ a_1(\lambda,\ 0°), \tag{3.10}$$

with $a_1$ the planet's phase function (see Eq. 3.8), and $\pi F_0$ $[W/(m^2\ m)]$ the stellar flux arriving at the planet, measured perpendicular to the direction of propagation of stellar light [64].

Given unpolarized incident starlight, the observable total and polarized fluxes of starlight reflected by a planet and arriving at Earth (a distance $d$ away) can be written as [64]

$$\begin{aligned} F(\lambda,\ \alpha) &= \frac{r^2}{d^2}\ \frac{R^2}{D^2}\ \frac{1}{4} a_1(\lambda,\ \alpha)\ \pi B_0(\lambda) \\ Q(\lambda,\ \alpha) &= \frac{r^2}{d^2}\ \frac{R^2}{D^2}\ \frac{1}{4} b_1(\lambda,\ \alpha)\ \pi B_0(\lambda) \end{aligned} \tag{3.11}$$

The degree of polarization $P_s$ of the reflected starlight is then simply given by [64]

$$P_s(\lambda,\ \alpha) = -\ \frac{Q(\lambda,\ \alpha)}{F(\lambda,\ \alpha)} = -\ \frac{b_1(\lambda,\ \alpha)}{a_1(\lambda,\ \alpha)}. \tag{3.12}$$

It is clear that this $P_s$ depends solely on the planetary scattering matrix elements $a_1$ and $b_1$ [64]. As $P_s$ is a relative measure, it is independent of the radii of the star and planet, and the distances between the star and the planet and the planet and the observer, making it a convenient tool when analysing direct observations of exoplanets with inaccurately known sizes and at inaccurately known distances [64]. Furthermore, $P_s$ of a given planet is also independent of the stellar flux that is incident on the planet.

Vector **F** describes the flux vector that arrives at the top of the Earth's atmosphere, and it does not include extinction in the Earth's atmosphere in the case of a ground-based telescope and/or and instrument's response. To add these effects, **F** should be multiplied by matrices describing the desired effects [64]. Note that atmospheric extinction affects all elements of **F** equally and thus not its degree of polarization $P_s$.

In Eq. 3.12, it is assumed that at wavelength $\lambda$, the only planetary flux is due to reflection. In general, of course, a planetary signal consists of starlight that the planet reflects and of thermal radiation that the planet emits. Depending on the temperature of the planet, the thermal radiation is emitted at near-IR wavelengths and is mostly unpolarized when integrated over the planetary disk [66].

In case there is both reflected starlight flux and thermally emitted flux at wavelength $\lambda$, $P_s$ of the planet thus equals [66]

$$P_s(\lambda,\ \alpha) = -\ \frac{Q_{\text{reflected}}(\lambda,\ \alpha)}{F_{\text{reflected}}(\lambda,\ \alpha) + F_{\text{thermal}}(\lambda,\ \alpha)} \tag{3.13}$$

With $F_{\text{reflected}}$ and $Q_{\text{reflected}}$ given by and with $F_{\text{thermal}}$ the thermally emitted flux ($Q_{\text{thermal}}$ is assumed to equal zero). Note that for very hot planets, the thermal flux might severely suppress $P_s$ and limit the use of polarimetry to the shortest wavelengths [66].

## 3.3. Definition of the signals of the planetary system

The Trappist-1 planetary system consists of red dwarf star Trappist-1 and 7 planets (see Ch. 2). The planets orbit the star in such tight orbits that it will be impossible to observe the signal of a single planet

[1] A Lambertian reflecting surface reflects all incident light unpolarized and isotropically. Note that in this report, we apply an albedo to a Lambertian reflecting surface. For example, a Lambertian reflecting surface with an albedo of 0.3, reflects 30% of the incident light, unpolarized and isotropically.

without also capturing the signals of the other planets and that of the star itself. From the observer's point of view on Earth, the angular distance for each Trappist-1 planet and its star, when going from 1b to 1h, is: 0.0019, 0.0026, 0.0037, 0.0049, 0.0064, 0.0078, 0.010 arcsec. Given that the James Webb Space Telescope has an angular resolution of 0.1 arcsec (at about $\lambda = 2\ \mu m$) [13], which exceeds the angular distance of the Trappist-1 planets, these cannot be spatially resolved from their star.

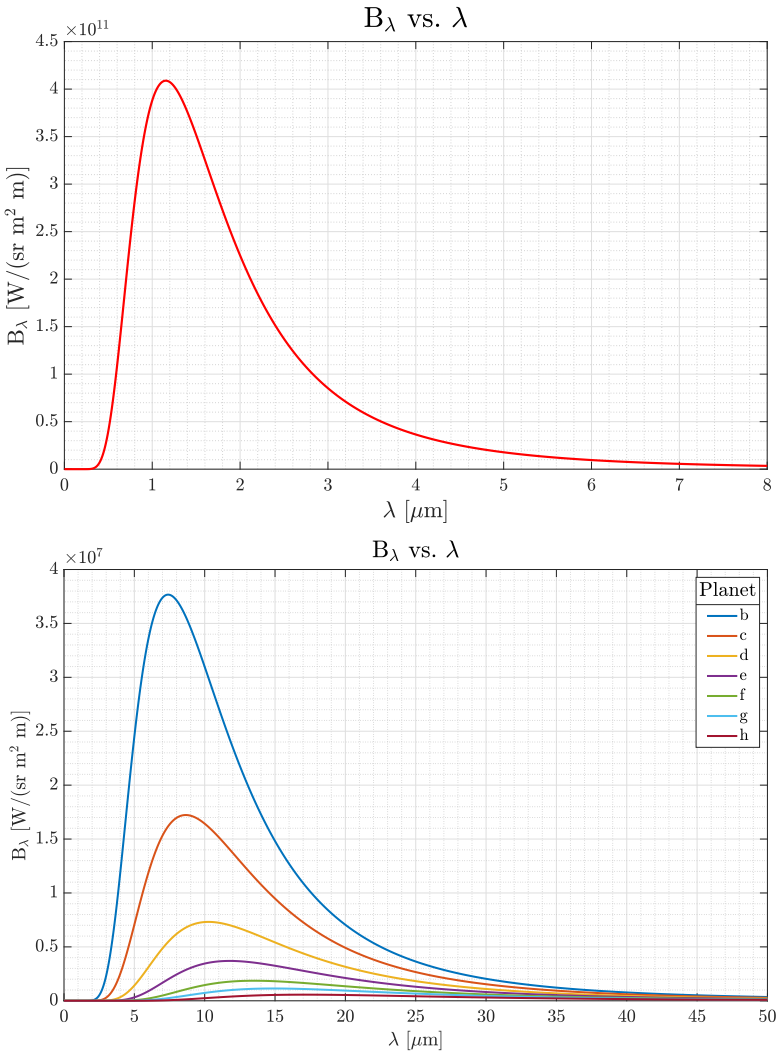


Figure 3.1: Top: The computed Planck curve for the Trappist-1 star, for an effective temperature of 2511 K [9], taken from Chapter 2 Fig. 2.2. Bottom: The computed Planck curves for the Trappist-1 planets, assuming their effective temperature, $T_{\text{eff}}$, predictions from Delrez et al. (see Table 2.1) [9]: 391.5 K for planet b, 334.8 K for planet c, 282.1 K for planet d, 246.1 K for planet e, 214.5 K for planet f, 194.5 K for planet g, and 169.2 K for planet h.

Assuming that the thermal flux of each planet can be neglected, that the orbits of all planets have the same inclination angle $i$, namely $i = 90°$ (which they almost do, see Table 2.1), and that all planets are mirror-symmetric with respect to the planetary scattering plane, the degree of polarization of the system as a whole at time $t$ is given by

$$P_s(\lambda, t) = -\frac{\sum_{j=1}^{7} Q_j(\lambda, \alpha_j(t))}{F_0(\lambda) + \sum_{j=1}^{7} F_j(\lambda, \alpha_j(t))}, \tag{3.14}$$

with $F_j$ the total flux of the starlight that is reflected by planet $j$, with $Q_j$ the polarized flux of the starlight that is reflected by planet $j$, and with $F_0$ the direct stellar flux that arrives at the target planet. Since $F_0$ depends on the stellar flux of Trappist-1, which is a function of the star's spectrum (see Fig. 2.2), then the flux intercepted by the observer depends on the wavelength at which it is seen.

The phase angles $\alpha_j$ of the 7 Trappist-1 planets change as each planet orbits the star, and they thus depend on time $t$. Figure 3.2 shows the time dependence of the planets for a period of 10 Earth days.

Note that when computing $P_s$ of the Trappist-1 planetary system according to Eq. 3.14, we ignore the small decrease in the stellar flux $F_0$ when one of the 7 planets transits, and we ignore the temporarily disappearance of the planetary flux as a planet is behind the star, as seen from the Earth. When we compute the signal of the whole Trappist-1 system in Ch. 4, we take into account this temporary disappearance, or the eclipse, explained as follows.

The reflected and polarized fluxes are at a maximum when an exoplanet's starlit hemisphere is directly facing the observer, which occurs in the event of an eclipse, when said exoplanet is behind its parent star (so is configured as a straight observer-star-planet line). When this occurs, the fluxes and degree of polarization equal 0 as they cannot be intercepted by the observer, due to the star being in the way. Given a star of radius $R$ and a planet orbiting it at semi-major axis $a$, the angle $\theta_{ecl}$ at which the planet is covered by its star is $\theta_{ecl} = \arctan\frac{R}{a}$. For a circular orbit, symmetry shows that the planet is behind its star at orbital angle range $[\theta_{ecl};\ -\theta_{ecl}]$, which occur at the smallest phase angles. Assuming the planet is much smaller than the star, and the star radius is much smaller than the semi-major axis, the fluxes and degree of polarization therefore instantly drop to 0 throughout the eclipsing range. Interestingly, while planets with larger orbits have a smaller eclipsing angle $\theta_{ecl}$, this effect is outweighed by their longer orbiting periods, causing the eclipse time to be larger for planets further from their star. The effect of this phenomenon is shown in Fig. 4.18, where 1b (of $\theta_{ecl} = 2.8°$) has an eclipse of about 32 minutes, and 1h (of $\theta_{ecl} = 0.5°$) has an eclipse of about 4 hours, despite it having a smaller eclipse angle.

Furthermore, it is important to realise that $P_s$ of the planetary system as a whole does depend on the radii of the planets, and on their distances to the star Trappist-1, as the latter determine the stellar flux that is incident on each planet. When computing $P_s$ of the system as a whole, we can thus also not replace a $Q_j$ and an $F_j$ by the respective planetary scattering matrix elements $b_{1j}$ and $a_{1j}$, respectively, as could be done for a single planet (see Eq. 3.12). Indeed, we have to compute each $F_j$ and $Q_j$, using Eqs. 3.11. In order to do so, we need to know for each Trappist-1 planet at the wavelength $\lambda$ under consideration:

- Its radius, $r$ (see Table 2.1)
- Its distance to the star, $D$ (see Table 2.1)
- Its flux phase function, $a_1$ (see Sect. 3.4)
- Its polarized phase function, $b_1$ (see Sect. 3.4)
- Its phase angle, $\alpha$, at each time $t$ (see Fig. 3.2)

Note that $P_s$ is independent of the distance $d$ between the Trappist-1 system and the Earth.

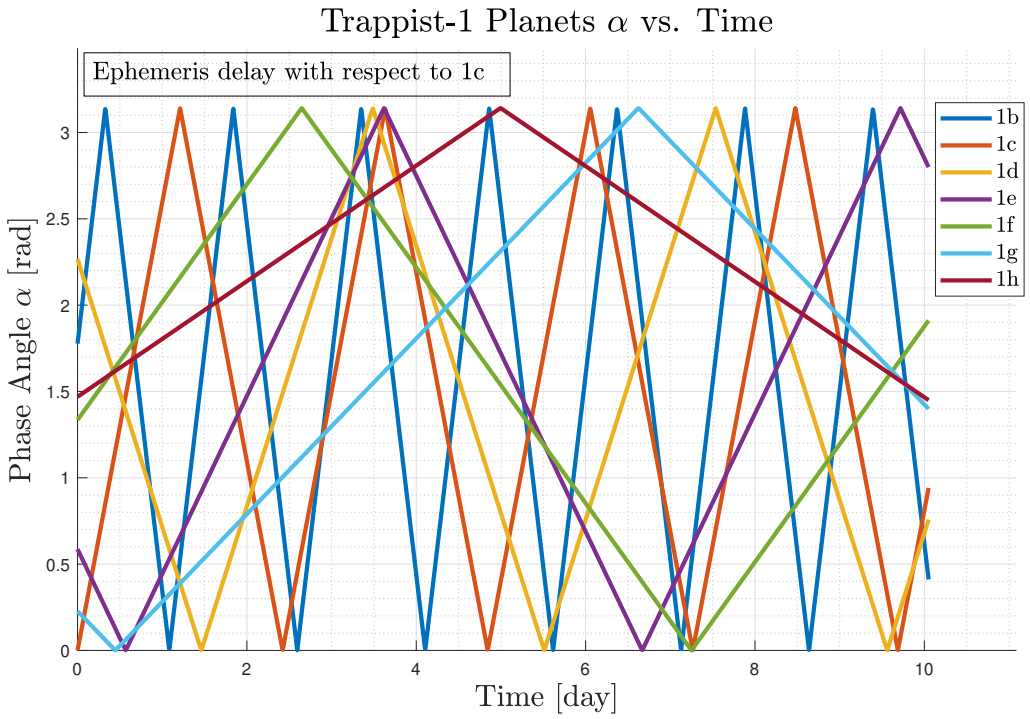


Figure 3.2: The temporal variation of the phase angle $\alpha$ of each of the 7 Trappist-1 planets over a period of 10 Earth days, see Table 2.1 for the periods of the planets. At $t = 0$, $\alpha$ of planet Trappist-1c is equal to 0°. Note that these curves follow a sinusoidal shape, though due to the very large distance of the Trappist-1 system from the observer on Earth, they look linear.

## 3.4. Calculating the planetary phase functions $a_1$ and $b_1$

To calculate the total and polarized fluxes of the planets in the Trappist-1 system, we have to compute elements $a_1$ (the phase function) and $b_1$ (the polarized phase function) of each planet of the planetary scattering matrix **S** of each planet. The first step in calculating these elements of **S** as functions of the phase angles is to make a numerical model of the planetary atmosphere and underlying surface.

The atmosphere is defined as a stack of locally plane-parallel, horizontally homogeneous layers, containing gaseous molecules and optionally aerosols [66]. for which an adding-doubling algorithm was used to calculate the radiative transfer through a locally plane-parallel planetary atmosphere, then a disk-integration algorithm was used to integrate the reflected flux vectors across the illuminated and visible parts of the planetary disk [64].

The planetary disk seen by the observer is divided into a grid of square pixels. For each pixel we compute with the reflected total and polarized fluxes, allowing us to study both disk-resolved and disk-integrated signals. Each pixel can be assigned a different model atmosphere such that we can study the effects of different cloud coverage maps on the reflected signals [54].

Directions in the plane-parallel model atmosphere are specified by $\mu = \cos\theta$, with $\theta$ the angle with the downward vertical, and the azimuth angle $\phi$, which is measured from an arbitrary plane and clockwise when looking up [66]. The direction of incident starlight is denoted by $(\mu_0, \phi_0)$, and that of light reflected towards the observer is by $(\mu, \phi)$; since horizontally homogeneous planets are assumed in this study, only the difference $\phi - \phi_0$ is relevant [66].

The adding-doubling radiative transfer code was used and tested for Earth remote-sensing applications, and the disk-integration algorithm is very efficient, yielding a very small computing time, and depends a little on the number of planetary phase angles for which the disk-integrated flux vectors are calculated [64].

## 3.5. The planetary atmospheres and surfaces

To describe the light reflection by the flat surface under the atmosphere, the surface reflection matrix $\mathbf{A}_s$ should be specified, and is normalized such that the average of its element $(1,\ 1)$ over all reflection directions is equal to the surface albedo $A_s$, defined as the fraction of incident stellar flux that the surface reflects in all directions [64]. It is assumed that reflection by the surface is isotropic, so the reflection matrix element $(1,\ 1)$ is independent of the direction of the incoming and reflected light [64].

The surface of Earth and maybe even some exoplanets is covered by numerous soil types with various albedos, which in turn depend on factors like the time of the year of air humidity [64]. The model planet in this work is made up of either a deep ocean, or a plain surface (whose albedo is to be set). Vegetation will not be considered for this work.

Even with an albedo of 0, the modelled oceans reflect a fraction of incident light because a specular (i.e. Fresnel) reflecting interface between the atmosphere and the black ocean was included, where specular reflection is anisotropic and usually leads to polarized reflected light [64].

The model planetary atmosphere is locally plane–parallel, and vertically divided in homogeneous layers filled with gas, and one of them, optionally, also containing cloud particles [54]. Cloud particles considered in this paper are spherical, homogeneous, liquid water cloud droplets, whose refractive index is chosen to be wavelength-independent and equal to $1.33 + 0.0001i$ [64]. The clouds are modelled as horizontally homogeneous layers, allowing surface features to show up in the reflected light even if the planet is fully covered [64].

A visualization of how the layer characteristics are defined and how the layers are read by the code is presented in Fig. 3.3.

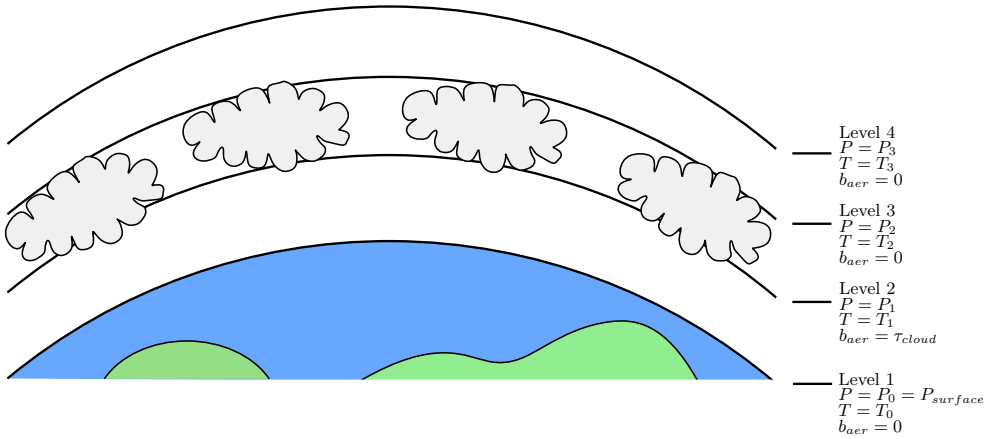


Figure 3.3: Diagram depicting the atmospheric layers and their main properties.

The model atmospheres used in this study consist of stacks of homogeneous layers containing gaseous molecules, in addition to cloud particles, where each atmosphere is bounded by a flat homogeneous surface underneath it [64]. For radiative transfer calculations, the optical thickness $b$, the single-scattering albedo $a$, the scattering matrix $\mathbf{F}_{sca}$ of the mixture of molecules and cloud particles must be known for each layer [64]. For starters, the optical thickness $b$ $[-]$ for each atmospheric layer can be treated as the sum of molecular and cloud extinction optical thicknesses $b^m$ $[-]$ and $b^c$ $[-]$ respectively [64]

$$b(\lambda) = b^m(\lambda) + b^c(\lambda) = b^m_{sca}(\lambda) + b^m_{abs}(\lambda) + b^c_{sca}(\lambda) + b^c_{abs}(\lambda) \tag{3.15}$$

The molecular scattering and absorption optical thicknesses are ${b^m}_{sca}$ and ${b^m}_{abs}$ respectively, and the the cloud scattering and absorption optical thicknesses are ${b^c}_{sca}$ and ${b^c}_{abs}$ respectively. The molecular scattering ${b^m}_{sca}$ depends on molecular column density ($molecules/m^2$, depends on ambient pressure and temperature), the refractive index of dry air, and depolarization factor of air [64]. The molecular

absorption ${b^m}_{abs}$ depends on molecular column density, mixing ratios of absorbing gases, and their molecular absorption cross section ($m^2$/molecule, depend on wavelength and ambient pressure and temperature) [64]. The cloud absorption and scattering ${b^c}_{abs}$ and ${b^c}_{sca}$ respectively are obtained from the cloud particle column density, the extinction cross-section, and the single-scattering albedo of the cloud particles [64].

With respect to Fig. 4.3, and for the same surface pressure, a heavier atmospheric gas causes the degree of polarization to drop. As such, a smaller molecular mass implies the number of molecules present in the atmosphere is higher, to maintain the same pressure. The atmospheric gas' molecular scattering optical thickness $b^m_{sca}$ $[-]$ is given by

$$\begin{aligned} b^m_{sca}(\lambda) &= N_{gas}\ \sigma_{sca} \\ N_{gas} &= \frac{p_{bottom} - p_{top}}{m_{gas}\ g} \\ \sigma_{sca}(\lambda) &= \frac{24\ \pi^3}{N_L^2} \frac{(n^2-1)^2}{(n^2+2)^2} \frac{6+3\delta}{6-7\delta} \frac{1}{\lambda^4} \end{aligned} \tag{3.16}$$

With $\sigma_{sca}$ $[m^2]$ the scattering cross section of a gas molecule, $N_L = 2.54743 \times 10^{25}\ m^{-3}$ Loschmidt's number, $n$ $[-]$ the refractive index of the atmospheric gas, $\delta$ $[-]$ the depolarization constant of the gas, $N_{gas}$ $[\#/m^2]$ the column number density of the gas molecules, $p_{top}$, $p_{bottom}$ $[Pa]$ the pressure at top and bottom of the layer respectively, $m_{gas}$ $[kg]$ the mass of a single molecule, and $g$ $[m/s^2]$ the local gravitational field strength.

The single-scattering albedo of the mixture of gaseous molecules and cloud particles in an atmospheric layer is [64]

$$a(\lambda) = \frac{b^m_{sca}(\lambda) + b^c_{sca}(\lambda)}{b^m_{sca}(\lambda) + b^m_{abs}(\lambda) + b^c_{sca}(\lambda) + b^c_{abs}(\lambda)} \tag{3.17}$$

The scattering matrix of said mixture is [64]

$$\mathbf{F}_{sca}(\Theta,\lambda) = \frac{b^m_{sca}(\lambda)\ \mathbf{F}^m_{sca}(\Theta,\lambda) + b^c_{sca}(\lambda)\ \mathbf{F}^c_{sca}(\Theta,\lambda)}{b^m_{sca}(\lambda) + b^c_{sca}(\lambda)} \tag{3.18}$$

with $\Theta$ the scattering angle ($\Theta = 180 - \alpha$, and $\Theta = 0°$ for forward scattering), $\mathbf{F}^m_{sca}$ is the scattering matrix of molecules and $\mathbf{F}^c_{sca}$ is the scattering matrix of cloud particles.

Next, the local reflection matrix **R** should be calculated for various combinations of $(\mu_0,\ \phi_0)$ and $(\mu,\ \phi)$ [66]. **R** depends on the optical thickness, the single scattering albedo, and the scattering matrix of gas molecules and aerosols in the layer [66]. The eDAP program, a adding-doubling radiative transfer algorithm that considers multiple scattering and polarization, was used to obtain and integrate the **R** matrix at every $\alpha$ over the illuminated and visible part of the planetary disk, (to obtain **R**) [66]. To visualize, the reflection matrix of a Lambertian surface for instance, is given as [69]

$$\mathbf{R}_L = A_s \begin{Bmatrix} 1 & 0 & 0 & 0 \\ 0 & 0 & 0 & 0 \\ 0 & 0 & 0 & 0 \\ 0 & 0 & 0 & 0 \end{Bmatrix}, \tag{3.19}$$

### 3.5.1. Code principles and possibilities

The disk integration method is based on expanding the radiation field of the planet into generalized spherical functions, and pertains to horizontally (in)homogeneous planets having vertically inhomogeneous planetary atmospheres [64]. One advantage of this method (compared to more conventional flux integration and polarization over a planetary disk) is that a planet's flux and polarization can be rapidly obtained for an arbitrary number of planetary phase angles, without performing radiative transfer calculations for each new phase angle; this is advantageous because polarization calculations are

highly time consuming compared to mere flux calculations [64]. One disadvantage of the code is that it takes long to run for a partial cloud cover, so we rely on Eq. 3.20 to compute the signals for patchy clouds.

Fig. 3.4 gives a taste of the shape of plots we expect from the code (presented in Ch. 4). From this figure, we see that for singly scattered light, $P_s$ is highest at $\alpha = \Theta = 90°$, at which the light is not completely polarized, only about 95% due to the molecular depolarization factor [64]. Also, due to symmetry, $P_s = 0$ when $\Theta = 0°$ and $180°$ (for singly scattered light) [64].

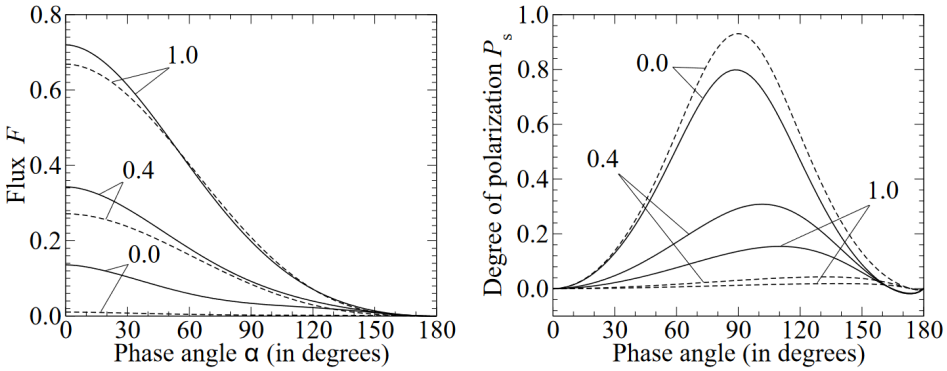


Figure 3.4: Flux $F$ (left) and degree of linear polarization $P_s$ (right) of starlight reflected by model planets with a surface albedo $A_s = 0.0,\ 0.4,\ 1.0$, as a function of the phase angle $\alpha$. The curves are plotted for two wavelengths, 0.44 $\mu$m (solid lines) and 0.87 $\mu$m (dashed lines). From Stam [64].

Gaseous molecules have strong polarizing capabilities, especially around $\alpha = 90°$, around which $P_s$ peaks, because $P_s$ of light singly-scattered by gaseous molecules (which are present in every model atmosphere) is largest at $\alpha = 90°$, see Fig. 3.4 [66]. Aside from the slight $\lambda$-dependence of the depolarization factor, the scattering matrix elements of cloud (and haze) particles are $\lambda$-dependent, while those of the gaseous molecules are not [66]. The maximum value of $F$ provides much less information on a planet's atmosphere than that of $P_s$, because 1) the maximum value of $F$ depends on the orbital inclination angle; 2) $F$ is less sensitive to the composition and structure of the planetary atmosphere; 3) $F$ can be measured less accurately than $P_s$ because the latter is a relative measure (so it can be determined with accuracies up to $10^{-5}$); and 4) to derive information on the planet from measured values of $F$, accurate knowledge about the planetary system is required [66].

So far, we have considered a full cloud layer covering the entire surface. If we want to consider a patchy cloud cover, which can be anywhere on the planet, the following can be done [52]. The signals of a partially cloudy planet is obtained by weighing the average of a clear planet and a fully cloudy one. Assuming the cloud cover is patchy, and considering a clear planet of Stokes parameters $[F_{clear},\ Q_{clear},\ P_{clear}]$, and a cloudy planet of Stokes parameters $[F_{cloudy},\ Q_{cloudy},\ P_{cloudy}]$, then for a desired cloud cover fraction $N$, the Stokes parameters for a partial cloud cover are computed as follows

$$\begin{aligned} F_{patchy} &= (1-N)\ F_{clear} + N\ F_{cloudy} \\ Q_{patchy} &= (1-N)\ Q_{clear} + N\ Q_{cloudy} \\ P_{s,\,patchy} &= -\frac{Q_{tot}}{F_{tot}} \end{aligned} \tag{3.20}$$

**Required Variables**

The following variables are required in order to compute the polarization signal of the model planets.

- The surface albedo $A_S$
- The wavelength $\lambda$, upon which most calculations depend

- The effective particle radius $r_{eff}$ and variance $v_{eff}$, on which the aerosol/droplet particle size distribution is based
- The refractive index $n$
- The number of layers
- The thickness of layers
- The planetary phase angle $\alpha$, with which the flux and degree of polarization are computed
- The medium's optical thickness $b$, which is a measure of the absorption or scattering of radiation by an optically active medium, such as the atmosphere or clouds [23]
- The atmospheric degree of polarization $\delta$

### 3.5.2. Other work

Here we look into the work done by Kopparla et al. [33], as it concerns the polarimetry of the Trappist-1 system. This is of particular importance as there is no available data for Trappist-1, so we compare our work with theirs instead.

Kopparla et al. modelled the disk-integrated phase curves and polarization signals for Trappist-1 planets, where they examined the following cases: dry, cloud-covered, partly oceanic, and fully oceanic planets [33]. They used a 1-dimensional radiative transfer model, and the target planet is divided into a grid of 64 boxes, with the radiation field derived at each box using a plane parallel 1-dimensional atmosphere. A Lambertian surface with an albedo of 0.2 was used to simulate dry land. Also, they have not included star-planet interactions like transits of eclipse effects, for which the flux would be 0. In addition, their code can only have one atmospheric constituent per layer (either clouds or gas), includes the rainbow effect for clouds and Fresnel reflection for oceans, but does not compute the glint through the clouds or a thick atmosphere; they have therefore used a high $\lambda$ to have minimal scattering by the atmosphere, making it 'most transparent' (remember that scattering is inversely proportional to $\lambda^4$, see Eq. 3.16).

We will come back to this during the discussion of results in Ch. 4.

### 3.5.3. Summary

The main advantage of using polarimetry for detecting exoplanets is that it can be used to distinguish the weak, polarized signal of starlight that is reflected by a planet from the strong, unpolarized, and direct starlight; as such, polarimetry can be used for direct detection of exoplanets that cannot be observed spatially resolved from their star (either because they are in a very close or very large orbit) [66]. Compared to flux observations, another advantage of polarimetry for characterizing planetary atmospheres is that because $P_s$ is a relative measure, it is independent of the distances between the planet and its parent star, between the planet and the observer, the sizes of the planet and the star, and the incoming stellar flux; so an exoplanet's atmospheric information can still be derived from $P_s$ without accurately knowing the aforementioned parameters [66]. Also, as $P_s$ is a relative measure, it is not affected upon transmission through Earth's atmosphere, so its $\lambda$-dependence is retained without needing to perform atmospheric corrections; this is particularly beneficial when searching for exoplanets with Earth-like atmospheres [66]. In some cases, polarization can provide additional constraints on atmospheric structure and cloudiness, which would further our understanding of these planets' atmospheres [39]. However, obtaining information about said exoplanet's atmosphere from reflected flux measurements is a much more difficult task as it requires accurate flux measurements, which we cannot obtain using present-day ground and space telescopes [33, 66]. Such direct observations of exoplanets are not yet available; they are very challenging as the faint signal of exoplanets is easily lost in the bright stellar glare [66].

We mentioned above that $P_s$ is a relative measure. For instance, if a telescope were on Earth, the polarization features would be unaffected by absorption from Earth's atmosphere (so elements in exoplanet atmosphere can be detected regardless of Earth's atmosphere), though the number of photons

received by the telescope (i.e. the flux) would be strongly affected by absorption in Earth's atmosphere [64].

In short, polarimetry is a useful tool to distinguish the (polarized) stellar light reflected by an Earth-like exoplanet from the (unpolarized) direct stellar light, and to detect Earth-like exoplanets [64]. Also, in contrast to using spectroscopy only, polarimetry can provide more and different information on the structure and composition of an exoplanet's atmosphere and surface, for example obtaining cloud top altitudes and gas mixing ratios [64].

# 4

# Results

In this chapter, we present the numerically computed total fluxes and degrees of polarization of the Trappist-1 planetary system. First, in Sect. 4.1, we present the signals of a few standard model planets to explain the features of the reflected total fluxes and polarization and their relation with the planet properties. Then, in Sect. 4.2, we present the signals of the individual Trappist-1 planets, as if they could be observed spatially resolved from their star. In Sect. 4.3, we present the combined signals, thus the signals of the planets and the star. Because of the tightness of the system and the huge distance between the system and the Earth, the latter signals are representative for future observations.

## 4.1. Flux and polarization signals of standard planets

In this section, we present the signals of a few standard Earth-like model planets to explain the features of the reflected total fluxes and polarization and their relation with the planet properties. The standard parameters that we use to describe these planets are representative for the Earth, and are listed in Table 4.1.

The total fluxes in the figures are normalized such that the vertical axis of the plots represents the planet's geometric albedo, which is equivalent to the first term in the $\mathbf{S}(\lambda, \alpha)$ matrix (from Eq. 3.7), called the planetary phase function $a_1$, divided by 4, so $a_1/4$. Furthermore, the signals that we present are for single planets that are spatially resolved from their parent star. They thus not include direct starlight.

| Parameter | Value |
|---|---|
| Depolarization factor | $\delta_{air} = 0.03,\ 0.027206$ (@$1.15\mu m$) |
| Gravitational acceleration | $g = 9.81\ m/s^2$ |
| Surface albedo | $A_s = 0.3$ |
| Air refractive index | $n_{\text{air}} = 1.0$ |
| Surface pressure | $p_s = 1\ atm$ |
| Top of atmosphere pressure | $p_{top} = 0\ atm$ |
| Molecular mass | $M_{\text{air}} = 29\ amu$ |

Table 4.1: Table showing the parameters for Earth. The depolarization factor, gravitational acceleration, air refractive index, surface pressure, top of atmosphere pressure, and molecular mass are atmospheric properties, while the surface albedo is a surface property.

The reason we include Table 4.1 is because the degree and direction of polarization of light that is scattered by a planet is sensitive to the properties of the atmospheric scatterers (size, shape, and composition), their spatial distribution, as well as to the reflection properties of the planetary surface

[53].

The reason for choosing this value of $\lambda$ is because Trappist-1 emits the most at this wavelength (see discussion of Eq. 2.1).

**Planets with gaseous, cloud–free atmospheres**

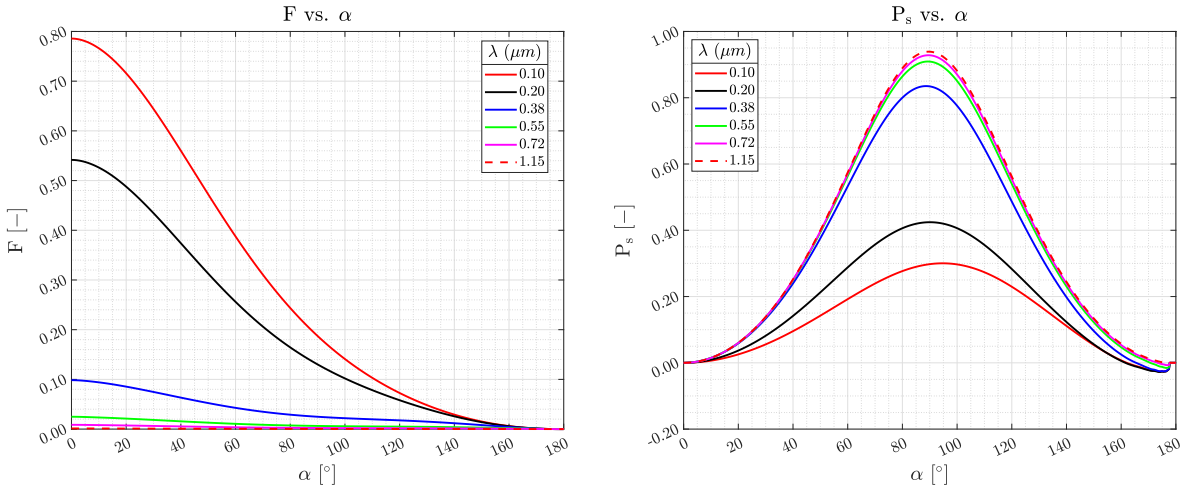


Figure 4.1: The total flux $F$ (left) and degree of polarization $P_s$ (right) of light reflected by an Earth-sized planet with a black surface ($A_s = 0$) and a gaseous atmosphere (of similar composition to Earth's, $M_u = 29$ amu, $\delta = 0.0284$, $p_s = 1\ atm$), for different wavelengths $\lambda\ (\mu m)$: 0.10 (red, solid lines), 0.20 (black, solid lines), 0.38 (blue, solid lines, corresponding to the violet spectrum), 0.55 (green, solid lines, corresponding to the average of the visible spectrum), 0.72 (pink, solid lines, corresponding to the red spectrum), and 1.15 (red, dashed lines, corresponding to the near-IR spectrum). The flux is normalized such that at $\alpha = 0°$, it equals the geometric albedo of the planet.

Figure 4.1 shows the total flux $F$ and degree of polarization $P_s$ of starlight that is reflected by a planet with a black surface ($A_s = 0.0$) and an Earth-like atmosphere in terms of $g$, $\delta$, $P_{\text{surf}}$, $n_{\text{air}}$, and $M_{\text{air}}$ (see Table 4.1) for wavelengths ranging from 0.1 $\mu$m to 1.15 $\mu$m. The latter is the wavelength at which the flux of star Trappist-1 is largest (see Fig. 2.2). The optical thickness (for each wavelength in $\mu$m) of these gases is: 14.1 (0.10), 0.0676 (0.38), 0.0154 (0.55), 0.0052 (0.72), 0.0008 (1.15).

From Fig. 4.1, some things can be noticed.

- The reflected flux is largest at $\alpha = 0°$, also called full phase, and decreases with $\alpha$, as the illuminated fraction of the disk decreases with respect to the observer. So at the smallest values of $\alpha$, the planet's starlit hemisphere is facing the observer (though in reality, it cannot be seen due to the star being in the way, this is described more thoroughly in Sect. 4.3). At the largest values of $\alpha$, the viewer is exposed to the nightside of the planet, thus $F$ is zero.
- The reflected flux decreases with increasing wavelengths. This is due to Rayleigh scattering being more effective at shorter wavelengths, as per Eq. 3.16, showing that the Rayleigh scattering is proportional to $1/\lambda^4$. So, as the wavelength increases, the atmosphere's scattering optical thickness decreases, and so the reflected flux decreases.
- $P_s$ for this black surface planet is (mostly) positive, so the reflected light is polarized perpendicular to the scattering plane (i.e. perpendicular to the imaginary line connecting the planet and the star as seen by the observer). $P_s$ is negative at the largest phase angles, where the reflected light is polarized parallel to the scattering plane; this negative polarization is due to second-order scattered light, which decreases with increasing wavelength [64].
- $P_s$ is more or less symmetric at $\alpha = 90°$, as the degree of polarization of light singly scattered by gaseous molecules is symmetric around $\alpha = 90°$ [64]. Only for the shortest wavelengths, multiple scattering in the atmosphere breaks the symmetry.
- For large phase angles, so when only a narrow crescent of the planet is visible, $P_s < 0$ and the direction of polarization is parallel to the scattering plane, where this negative polarization is

characteristic for light that has been scattered twice by molecules in the planetary atmosphere [66]. Note that multiply scattered light usually has a much lower degree of polarization than singly scattered light [64]. For such large $\alpha$, the contribution of the twice scattered light to $P$ can be significant because the single scattered light is virtually unpolarized [66].

- The dependence of $P_s$ on $\alpha$ depends strongly on the atmosphere, except when reflection is near the backward and forward directions ($\alpha \approx 0°$ and $\alpha \approx 180°$ respectively), where $P_s = 0$ regardless of the atmosphere due to symmetry, and because these values of $\alpha$ are not accessible for polarimetry [66].

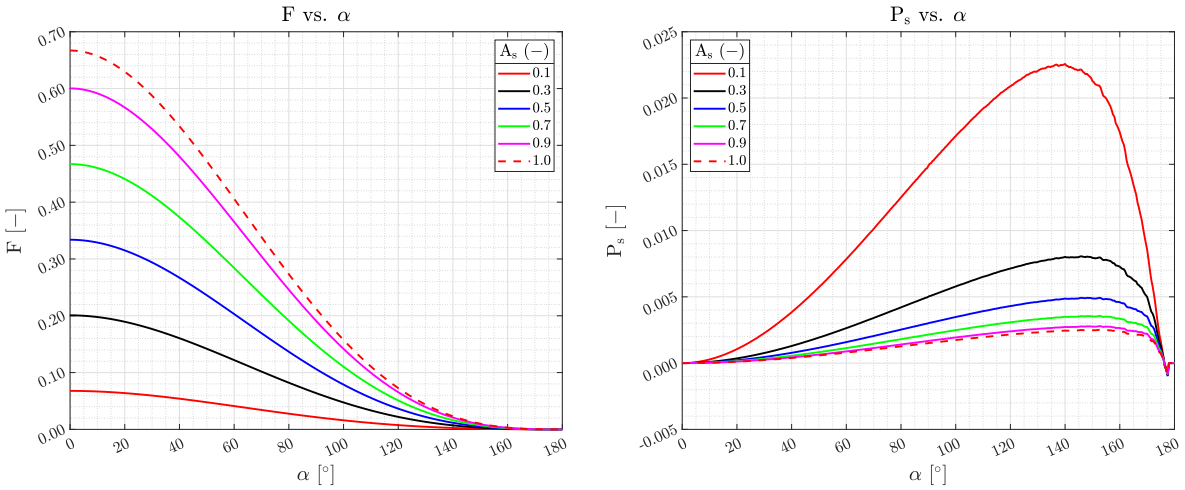


Figure 4.2: Similar to Fig. 4.1, except for different values of the planetary surface albedo $A_s$: 0.1 (red, solid line), 0.3 (black, solid line), 0.5 (blue, solid line), 0.7 (green, solid line), 0.9 (pink, solid line), and 1.0 (red, dashed line). The wavelength $\lambda$ is 1.15 $\mu$m.

Figure 4.2 shows $F$ and $P_s$ for planets with Lambertian reflecting surfaces with various albedo values. The planets have Earth-like atmospheric parameters (see Table 4.1). Fig. 4.2, some things can be noticed.

- A Lambertian reflecting surface, such as the one used here, results in a decrease in the degree of polarization curve, where this effect is amplified with increasing wavelength values. This is due to the unpolarized flux $F$ that is reflected by the surface (the $F$ curves in Fig. 4.2 are higher than those in Fig. 4.1, and the opposite holds for the $P_s$ curves), thereby lowering $P_s$ (reminder that $P_s = -Q/F$). For our case of an optically thin atmosphere (of optical thickness 0.0008 when $\lambda = 1.15\ \mu m$, as per the discussion of Fig. 4.1), and starting from a black surface of $A_s = 0$, increasing the surface albedo reduces the role of the atmosphere, increasing $F$ and decreasing $P_s$. The maximum $P_s$ occurs at $\alpha > 90°$; more specifically, with increasing $A_s$, the maximum $P_s$ shifts to larger $\alpha$ because for increasing $\alpha$, the photons travel a longer path through the atmosphere due to the geometry, thereby reducing the role of the surface.

Figure 4.3 shows $F$ and $P_s$ for a planet with $A_s = 0$ or $A_s = 0.3$, and Earth-like atmospheric parameters. Here, we have varied the atmospheric molecular mass $M_u$. It can be seen that when the atmospheric gas is heavier ($M_u$ is larger) for a given surface pressure, the column number density of the gas $N_{gas}$ decreases (see Eq. 3.16), thus the atmospheric gaseous scattering optical thickness $b^m_{sca}$ decreases, and reflected flux $F$ decreases. If the surface reflects (the bottom row of Fig. 4.3), this effect is small because most of the flux then comes from the surface. For a black surface, with increasing $M_u$ (and thus decreasing $N_{gas}$ and $b^m_{sca}$), the multiple scattering in the atmosphere will decrease, and hence $P_s$ slightly increases. For a non-black surface, the trend in $P_s$ is reversed: an increase in $M_u$ gives a decrease in $P_s$, because of the added unpolarized light that is reflected by the surface.

Figure 4.4 shows $F$ and $P_s$ for a planet with Earth-like atmospheric parameters, $A_s = 0.3$, and various values of the gravitational acceleration $g$. These curves are very similar to those shown in Fig. 4.3, because increasing $g$ (while the surface pressure and $M_u$ are constant), has a similar effect as increasing the surface pressure (see Eq. 3.16). Figure 4.5, finally, shows $F$ and $P_s$ for a planet with various surface

pressures $p_s$, $\lambda = 1.15\ \mu m$, and $A_s = 0.3$. Increasing $p_s$, increases the atmospheric scattering optical thickness $b_{\mathrm{sca}}^{\mathrm{m}}$, and thus the amount of scattering by the gas. This increases $F$ and it also increases $P_{\mathrm{s}}$, because more scattering by the gas decreases the contribution of unpolarized light that has been reflected by the surface.

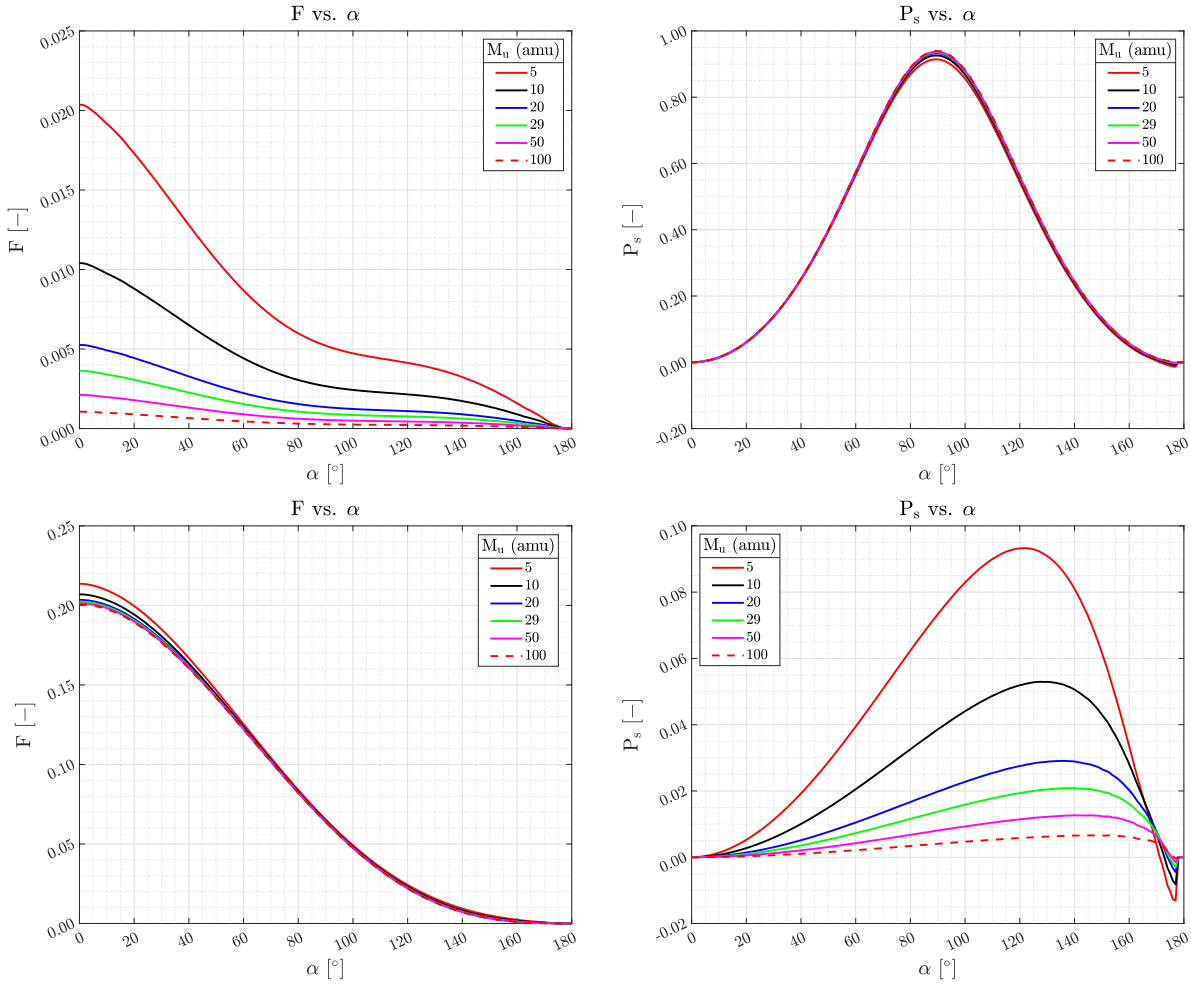


Figure 4.3: Similar to Fig. 4.1, except for different values of the gaseous molecular mass $M_u$ (in amu): 5 (red line), 10 (black line), 20 (blue line), 29 (green line, alluding to Earth's atmospheric mass), 50 (pink line), 100 (red dashed line). The wavelength $\lambda$ is 1.15 $\mu$m. In the top row, the surface albedo $A_s$ is zero (a black surface), and in the bottom row, $A_s = 0.3$. In reality, a change in $M_u$ would be associated with a change in $\delta$, and $p_s$, which we have not changed here.

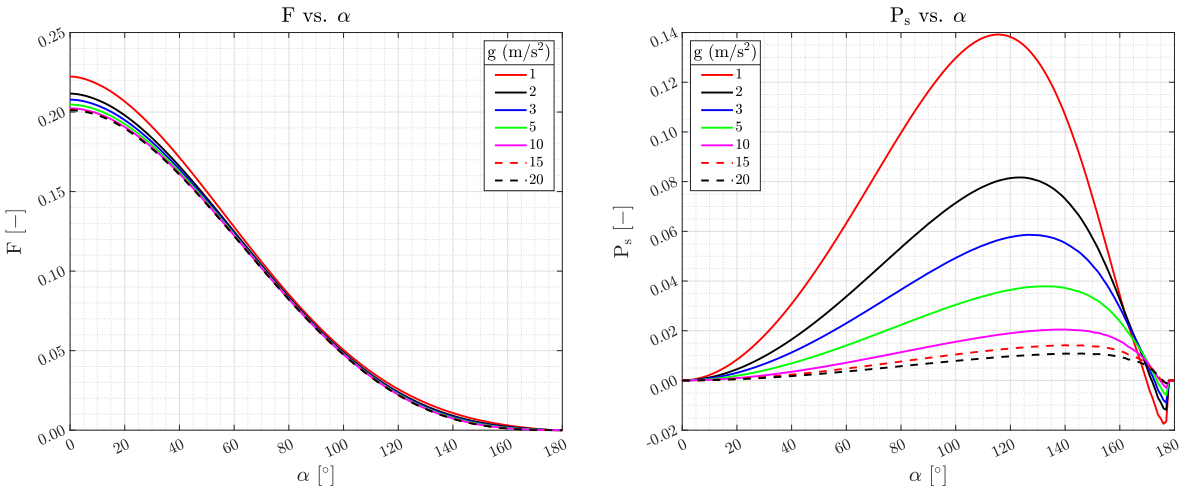


Figure 4.4: Similar to Fig. 4.1, except for different values of the gravitational acceleration $g$ (in $m/s^2$): 1.0 (red line), 2.0 (black line), 3.0 (blue line), 5.0 (green line), 10.0 (pink line), 15.0 (red dashed line), 20.0 (black dashed line). The wavelength $\lambda$ is 1.15 $\mu$m, and the surface albedo $A_s$ is 0.3. In reality, a change in $g$ would be associated with a change in $p_{\rm surf}$ which we have not changed here. It should be noted that not all values of $g$ shown here are realistic for an Earth-like planet, as it would alter the planet's mass or volume, which may not be Earth-like.

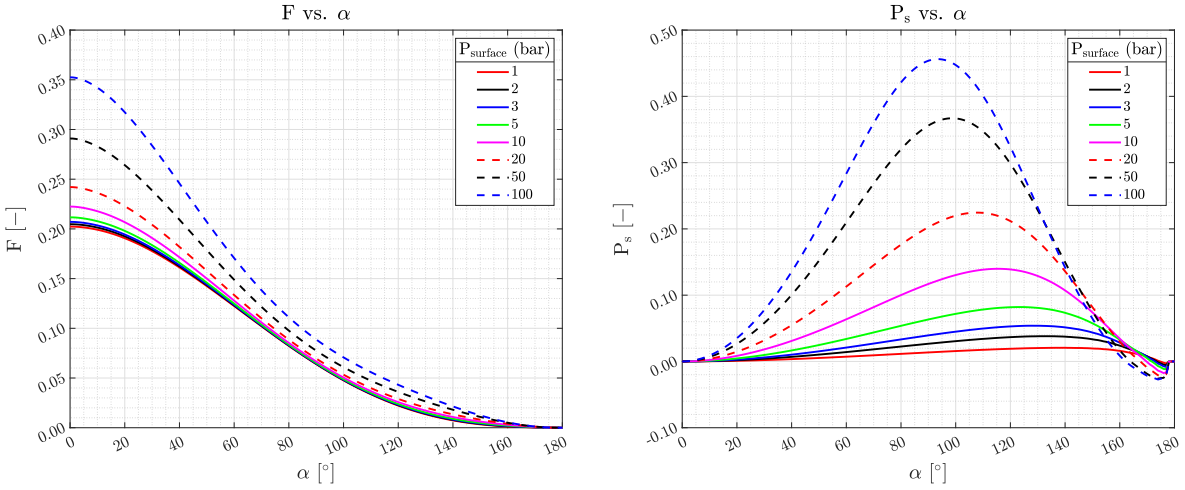


Figure 4.5: Similar to Fig. 4.1, except for different values of the surface pressure $p_s$ (in bar): 1 (red line), 2 (black line), 3 (blue line), 5 (green line), 10 (pink line), 20 (red dashed line), 50 (black dashed line), 100 (blue dashed line). The wavelength $\lambda$ is 1.15 $\mu$m, and the surface albedo $A_s$ is 0.3. In reality, a change in $p_s$ would be associated with a change in $g$, which we have not changed here.

The model planets discussed above, had either black surfaces or Lambertian reflecting surfaces, that reflect unpolarized light. Figure 4.6 shows $F$ and $P_{\rm s}$ for a planet with Earth-like atmosphere parameters and a Fresnel reflecting, water ocean surface. Note that Fresnel reflection is a type of specular reflection, described as reflection occurring at the boundary between two objects with different refractive indices, where some incident light is reflected back from the boundary and some of it is transmitted [25]. Below the surface, there is a 100 m thick water-body and a black surface. We show curves for different wind speeds $v_{wind}$, and thus for different angular distributions of the waves (more wind = higher waves). The following can be concluded from Fig. 4.6.

At small phase angles, the Fresnel reflection is weak, while at large phase angles, it is quite strong as its fraction is increased compared to the planetary disk (which resembles a crescent shaped illuminated disk at such high $\alpha$); this makes the planet appear white [69]. This causes a spike in $F$ at large $\alpha$ values. At small wind speeds, the glint size is smaller, but the reflection peak is stronger, because

there is less variation in the wave facets, producing a sharper peak in $F$ for large $\alpha$ [69]. It appears that the intersection phase angle of the $F$ curves is the same, regardless of wind speed: around 115°. Its location in terms of $\alpha$ depends on the reflection properties of the atmosphere, and the reflectance properties of the surface that is encountered by the light [69] (see below).

To investigate the dependence of the intersection phase angle on the surface composition, we repeated our computations with an ocean consisting of methane, (on Saturn's moon Titan liquid methane lakes have been found). The refractive index of liquid methane is $n = 1.2684$ at $\lambda = 1.15\ \mu m$ [40]. The curves are shown in Fig. 4.7. As can be seen, when changing from water to methane, the reflected flux decreases across all phase angles including the glint peak. The intersection phase angle shifts to a larger value: 135°.

The $P_s$ curve of a planet with a water ocean (Fig. 4.6) at low wind speed shares a big resemblance to the $P_s$ curve for a planet with a black surface in terms of size and shape (though the ocean planet skews more to the right). This is because the ocean is modeled as a 100 m thick layer of water, under which is a black Lambertian surface (similar to the one in Fig. 4.1). In the $P_s$ plot, all curves converge in an asymptotic manner a few degrees after their respective peak. This pattern is also found in Trees, who obtained this trait for numerous wavelengths, wind speeds, and sea foam albedo values [69]. When changing from water to methane, the $P_s$ curves significantly decrease, with more dramatic changes for higher wind speeds. The asymptotic convergence feature for different wind speeds is still present, though it occurs at a larger $\alpha$.

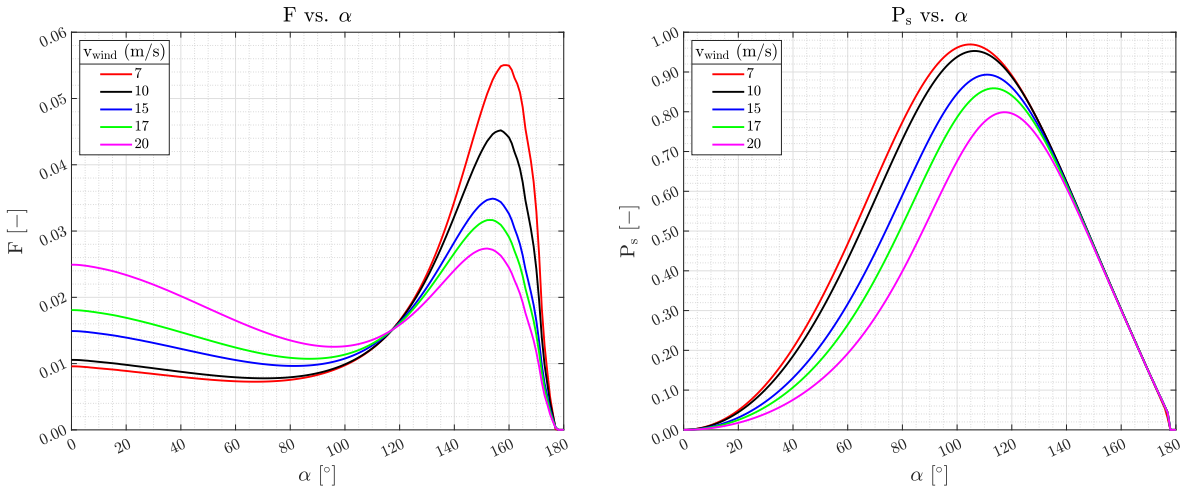


Figure 4.6: Similar to Fig. 4.1, except for a planet covered by a Fresnel reflecting water ocean surface. The wind speed over the ocean is varied: 7 m/s (red line), 10 m/s (black line), 15 m/s (blue line), 17 m/s (green line), 20 m/s (pink line). White caps are not included.

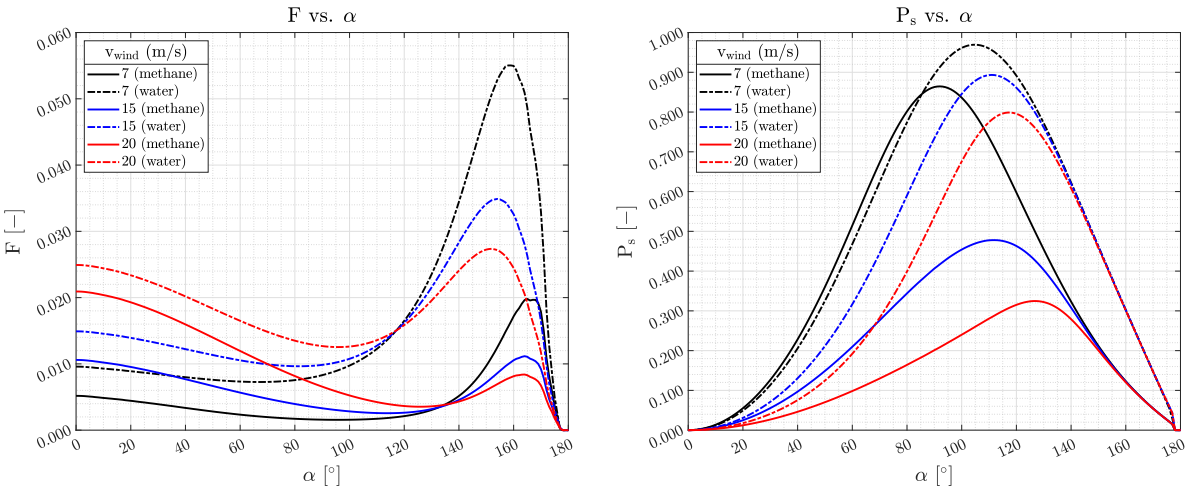


Figure 4.7: Similar to Fig. 4.6, but with the overlaying of curves for a methane ocean onto it, for selected values of wind speed: 7 m/s (black line), 15 m/s (blue line), 20 m/s (red line), for both methane (solid) and water (dashed) oceans.

### Planets with gaseous atmospheres and clouds

In this section, we add clouds to the atmospheres of the model planets. The clouds consist of spherical water droplets with properties defined in Table 4.2.

| Parameter | Value |
|---|---|
| Effective radius | $r_{eff} = 8\ \mu m$ |
| Effective variance | $v_{eff} = 0.1$ |
| Optical thickness | $b = 30$ (@1.15 $\mu m$) |
| Refractive index | $n_{cloud} = 1.33$ |

Table 4.2: The numerical parameters that describe the clouds.

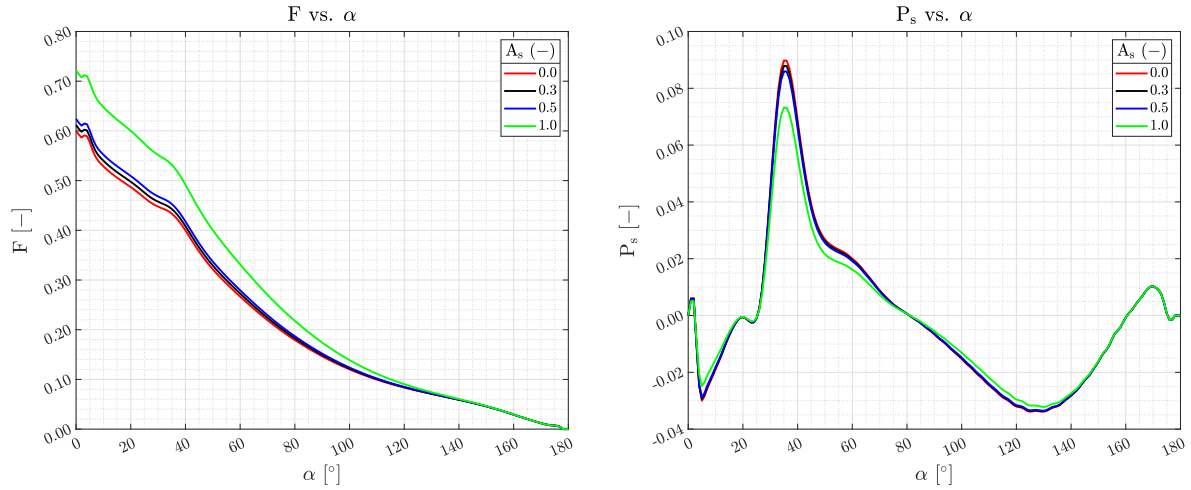


Figure 4.8: Similar to Fig. 4.2, except for a completely cloudy planet (with an optical thickness $b$ of 30).

Figure 4.8 shows $F$ and $P_s$ for a planet with Earth-like atmosphere parameters and a homogeneous cloud deck at an altitude of 2 to 3 km. The planet is completely covered by the cloud deck. The surface albedo is varied, and $\lambda = 1.15\ \mu m$. Figure 4.8 tells us the following.

Light reflected by the cloud layer depends on the scattering geometry and is generally polarized (while light is isotropically reflected by a Lambertian surface and is unpolarized) [29].

The degree of polarization of cloudy planets is low compared to that of planets with clear atmospheres except at short wavelengths; this is because of the following [64]. First, cloud particles strongly increase the amount of multiple scattering of light within the atmosphere, thereby decreasing the degree of polarization. Second, the degree of polarization of singly-scattered light by cloud particles is generally lower than that of singly-scattered light by gaseous molecules, especially at single-scattering angles $\approx 90°$. Finally, the direction of polarization of singly-scattered light by cloud particles is opposite to that of singly-scattered light by gaseous molecules. This causes the direction of polarization to be perpendicular to the terminator at longest wavelengths, at $\lambda \approx 0.73\ \mu m$. For this $\lambda$, the scattering optical thickness due to atmospheric molecules is negligible compared to the optical thickness of the cloud layer, so most of the reflected light is scattered by cloud particles [64]. In addition, on cloudy planets, a big amount of incoming starlight is diffusely transmitted through the cloud layer (through multiple scattering of light) then absorbed by the planet surface [64].

At about $\alpha = 37°$, the rainbow feature appears in the $F$ and $P_s$ curves, with an especially sharp increase in $P_s$. The rainbow indicates the presence of spherical cloud particles, as opposed to crystalline ones for instance [17]. For the chosen effective particle size of $8\ \mu m$, the particles are too small to produce a color bow, this would require a much larger particle radius of $\sim 20-30\ \mu m$, large enough so the light ray can have enough distance to refract and split colors. The first rainbow feature occurs at about $\alpha = 37°$, and the second rainbow feature, characterized by a much fainter bump in the $P_s$ curve is located at about $\alpha = 56°$. Because of the large cloud optical thickness (and assuming a thin atmosphere), the effect of the surface albedo on the polarization signals is reduced, though the value of the surface albedo plays a role. For instance, for a thin clear atmosphere with a white surface ($A_s = 1$), the degree of polarization is lower and the reflected flux is higher than for an atmosphere with clouds.

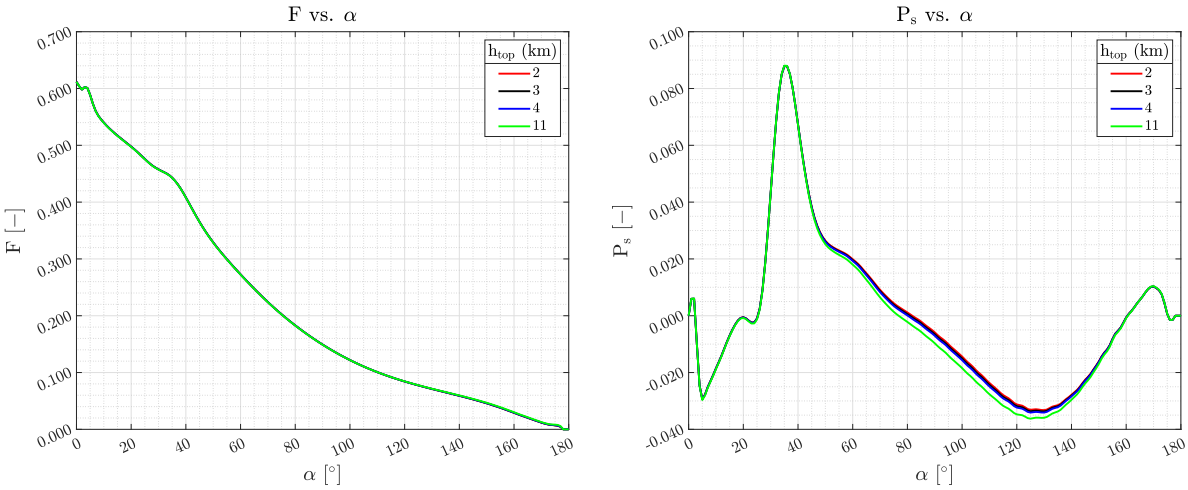


Figure 4.9: Similar to Fig. 4.8, but with a variable cloud-top altitude. The cloud layer has $b = 30$ and is 1 km thick and its top is located at the following altitudes (km): 2 (red), 3 (black), 4 (blue), 11 (green).

Figure 4.9 shows the normalized reflected flux and degree of polarization for a planet with Earth-like atmosphere parameters, a black surface and a homogeneous cloud cover with the cloud top at variable altitudes. Varying the cloud layer altitude changes the amount of gas above it for a given surface pressure. The higher the cloud layer, the less gas particles above it, so, the column number density of the gas $N_{\text{gas}}$ above the cloud decreases, and the gaseous scattering optical thickness $b^{\text{m}}_{\text{sca}}$ decreases too (see Eq. 3.16). At this large wavelength, $b^{\text{m}}_{\text{sca}}$ above the clouds is however very small for every cloud top pressure, and changing it has almost no effect of $F$ and very little effect on $P_{\text{s}}$, and only in the phase angle range where $P_{\text{s}}$ of the gas is largest.

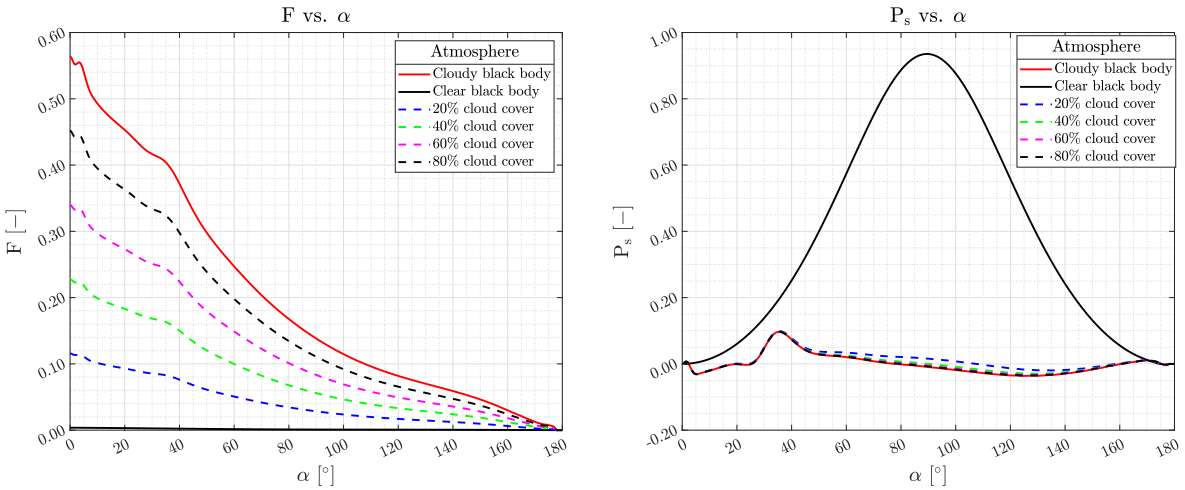


Figure 4.10: Similar to Fig. 4.8, except for a non-homogeneous patchy cloud cover: 20% clouds (blue dashed), 40% (green dashed), 60% (pink dashed), 80% (black dashed), along with a fully cloudy atmosphere (solid red) and clear atmosphere (solid black).

Figure 4.10 shows the normalized reflected flux and degree of polarization for a black surface planet with Earth-like atmosphere parameters and a non-homogeneous patchy cloud cover at an altitude of 2-3 km, for $\lambda = 1.15\ \mu m$, as computed using Eq. 3.20. This figure also includes the signals for two reference cases of a fully cloudy planet surface and a clear one (a purely gaseous atmosphere). It is interesting to note that the $F$ plot shows almost evenly spaced curves for a 20% increment in cloud cover (where a higher cover is associated with a higher $F$). The $P_s$ curves for the planets with even a little bit of clouds, on the other hand, are tightly clumped together near the fully cloudy case, which is due to the dark surface and the small gaseous optical thickness at this large wavelength: the clear atmosphere in between the clouds hardly contributes to the planetary signal.

It is worth mentioning that cloud particle size and variance play a role in reflected flux and degree of polarization, though this is beyond the scope of this study, the reader is referred to Stam [64].

## 4.2. Flux and polarization signals of the Trappist-1 planets

In this section, we present the signals of the individual 7 Trappist-1 planets, thus, as if they were observable spatially resolved from the star and from each other. Like in the previous section (Sect. 4.1), the total fluxes are normalized such that the vertical axis of the plots represents the planet's geometric albedo. As such, in this section, the normalized reflected flux is referred to as $F$.

Since there exist no measured data on the atmospheres and clouds of the Trappist-1 planets, many papers used their own numerical models to determine the presence and location of e.g. a cloud layer (see de Wit et al. [8], Kopparapu et al. [30], Moran et al. [42]). These models differ greatly in assumptions and computed atmospheric cloud layer properties. As such, we used clouds whose properties are shown in Table 4.2, a cloud layer of 1 km thickness, and a cloud-top altitude of 3 km. For the descriptions of the model atmospheres and surfaces, we used the possible characteristics of the Trappist-1 planets as listed in Tables 2.1 and 2.2. For a more detailed review of the possible atmospheric compositions on the Trappist-1 planets, the reader is referred to Chapter 2.

#### Planet Trappist-1b

Planet-1b is the innermost Trappist-1 planet: a rocky planet that most likely bears no clouds or surface water given its proximity to its parent star. Its atmosphere is thought to consist mostly of water vapor or oxygen, though a water-hydrogen mixture is possible. For the latter, it is assumed the elements are mixed throughout the atmosphere. Figure 4.11 shows $F$ and $P_s$ of this planet using the most likely

atmospheric combinations. The curves are for 1 atmospheric layer, with a surface albedo $A_s$ of 0.2, and a surface pressure $p_s = 1\ atm$. The wavelength is $1.15\ \mu m$.

In Fig. 4.11, the $F$ and $P_s$ signals are plotted for the most likely atmospheric composition, with and without clouds. The case of a homogeneous cloud deck covering the entire surface was considered, in addition to partial coverage, consisting of patchy clouds, which are assumed to be randomly distributed above the surface. This is done for various partial coverage percentages, from 20% to 80% in increments of 20%. While clouds are highly unlikely on 1b because to the planet's high temperature as it is very close to its parent star, we decided to include them for our atmospheric compositions nonetheless. The top row shows entries for the most likely atmospheric composition ($H_2O$ and $O_2$), in addition to a scenario where the atmospheric composition is a mixture of elements (shaded blue region) of varying percentages, without clouds. In this case, the shaded region is for the $H_2O - H_2$ mixture, and starts at 100% $H_2O$ / 0% $H_2$ (bottom edge of the shaded region) until it reaches 0% $H_2O$ / 100% $H_2$ (top edge). The curves show a very large degree of polarization for $H_2$, as per the discussion of Fig. 4.3, and a much smaller degree of polarization for the other compositions.

For the cloudy curves, the degree of polarization is generally very small, reaching a high value of $P_s$ at the rainbow (see the discussion of Fig. 4.8). The $P_s$ curves for cloudy planets are almost identical for $\alpha = 0-45°$, after which they separate slightly, rejoining at about $155°$; this is due to the scattering by the atmospheric gas above the cloud layer (reminder that for a black surface planet with an atmosphere, the $P_s$ increases with increasing gas weight $M_u$, and for a non-black surface, $P_s$ decreases with increasing $M_u$). The $F$ curves are highest for a homogeneous cloud deck, for which the curves for different compositions are almost, but not entirely, identical until about $\alpha = 120°$, at which point the curves separate by a tiny amount. For the non-cloudy cases, the $F$ curves showcase a larger difference.

The second row of Fig. 4.11 shows the $H_2O$ atmosphere with a variable horizontal cloud cover fraction, in increments of 20%. The same goes for the third row, except for an $O_2$ atmosphere. Starting from a non-cloudy case, the more we increase the cloud coverage, the more the $F$ and $P_s$ curves resemble the completely cloudy case. For instance, the normalized reflected flux increases for all phase angles, while the degree of polarization experiences a more uneven change. The degree of polarization increases for some phase angles and decreases in others; most prominent instances of this include the formation of the rainbow peak (at $\alpha = 38°$) becoming sharper with increasing cloud coverage, and the diminishing role of the atmospheric gas, which is seen by the change in the curvature of $P_s$ at $\alpha \approx 60 - 170°$.

When comparing the $F$ to the $P_s$ plots, the latter is more sensitive to the atmospheric composition, exhibiting more noticeable changes when varying the constituent (for both cloudy and clear atmospheres), and making features such as the rainbow more prominent. For instance, the degree of polarization curve peaks at $P_s \approx 0.055$ (for $\alpha \approx 130°$) for a $H_2O$ atmosphere, while for an $O_2$ atmosphere it peaks at $P_s \approx 0.033$ (for $\alpha \approx 135°$). This change of $P_s$ for varying atmospheric composition is similar to the one presented in Fig. 4.3.

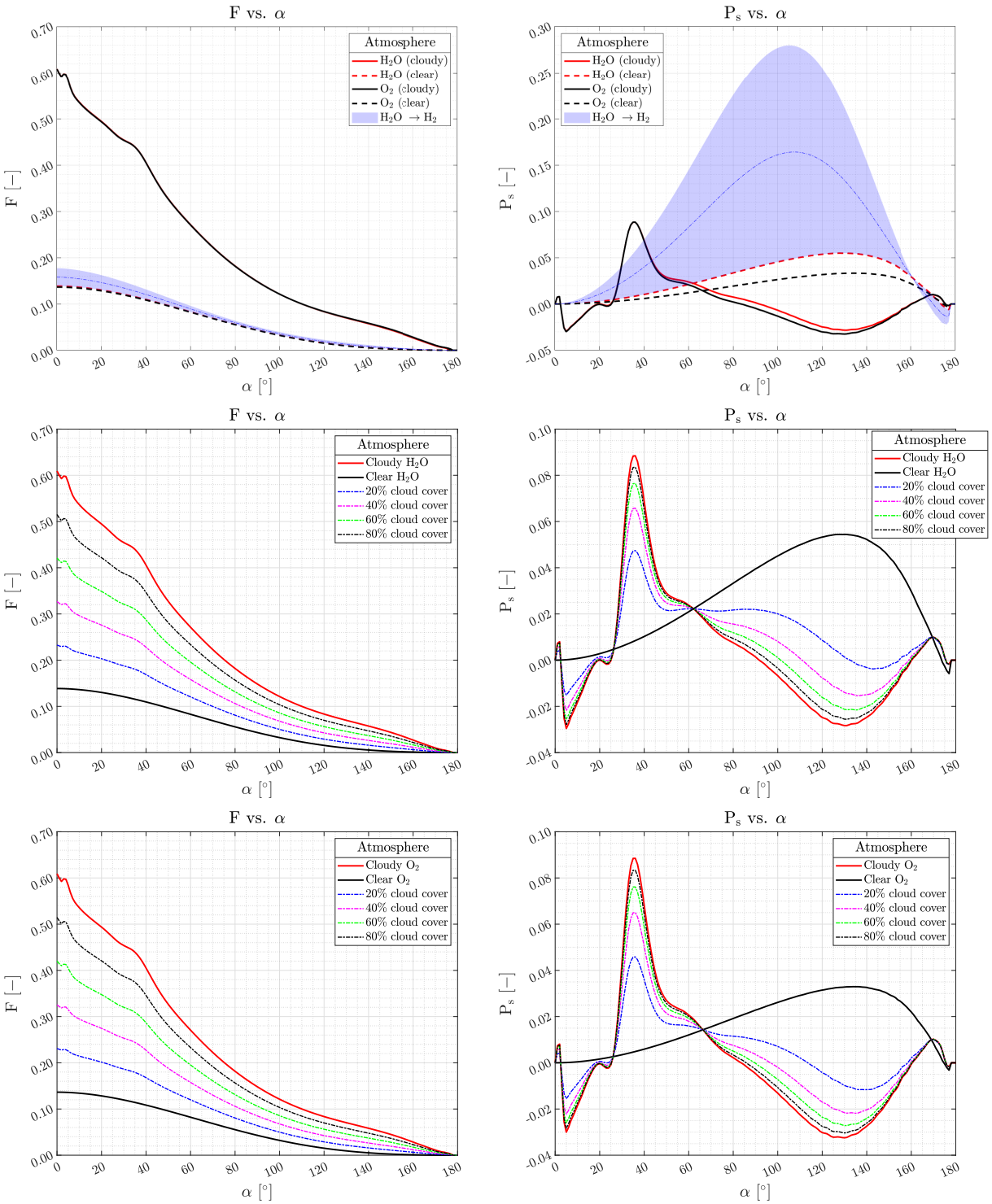


Figure 4.11: Flux and polarization signals for planet-1b. The first row illustrates the signals for the most likely compositions, with and without clouds. The second row illustrates the first likely composition according to Table 2.2 ($H_2O$), along with varying cloud cover values. The third row is the same as the previous one, but illustrates the other likely composition ($O_2$). The shaded portion in the first row encompasses many composition variations of $H_2O$ and $O_2$, varying from $100\%$ $H_2O$ (bottom edge) to $100\%$ $H_2$ (top edge). The notation "X→Y" in the legend implies X is the composition at the bottom edge of the shaded region, and Y is the composition at the top edge. The blue dotted line located in the shaded figure represents the average of all curves of the shading at every $\alpha$.

### Planet Trappist-1c

Planet-1c is the second closest planet to parent star Trappist-1. This is probably a rocky planet that most likely lacks any surface water given its proximity to its parent star, although it could have liquid water clouds. Its atmosphere is thought to consist mostly of oxygen, though a water-hydrogen mixture is possible. In Fig. 4.12, $F$ and $P_s$ for the most likely atmospheric combinations are shown, and the presence of clouds is also considered. The curves are for one atmospheric layer, with a surface albedo of $A_s = 0.2$, and an assumed surface pressure $p_s = 1\ atm$. The wavelength is $1.15\ \mu m$.

Planet-1c is very similar to planet-1b in terms of composition and features, differing in gravitational acceleration, size, and semi-major axis, though the latter two parameters are not employed in this section. From these, the atmospheric profile (in terms of pressure, temperature, or density) and cloud pressure vary between planets 1b and 1c. As such, what was said for Fig. 4.11 also holds for Fig. 4.12. In addition, the presence of clouds on 1c is more certain than on 1b, as the planet's surface temperature is lower due to it being further away from its parent star.

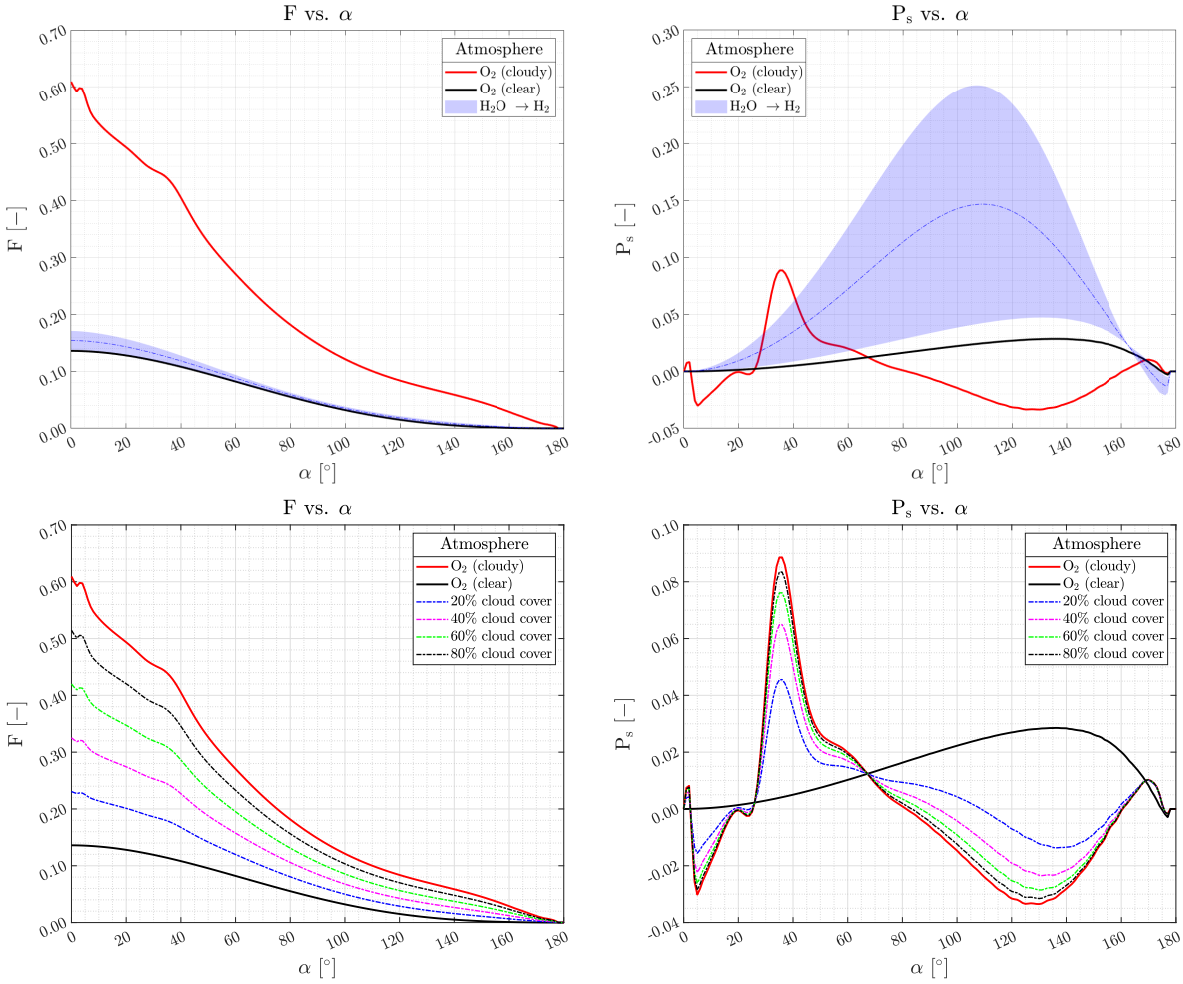


Figure 4.12: Similar to Fig. 4.11, except for planet-1c. The most likely atmospheric composition here is $O_2$.

### Planet Trappist-1d

Planet-1d is the third closest planet to Trappist-1 and possibly the innermost planet of the habitable zone. It is a rocky planet that could possibly bear clouds and/or surface water. Its atmosphere is

thought to consist mostly of water vapor, though a water-hydrogen mixture is possible. Figure 4.13 shows $F$ and $P_s$ for the most likely atmospheric combinations, and the presence of clouds on these combinations is also considered. The curves are for one atmospheric layer, with a surface albedo of $A_s = 0.2$, and an assumed surface pressure $p_s = 1\ atm$. The wavelength is $1.15\ \mu m$.

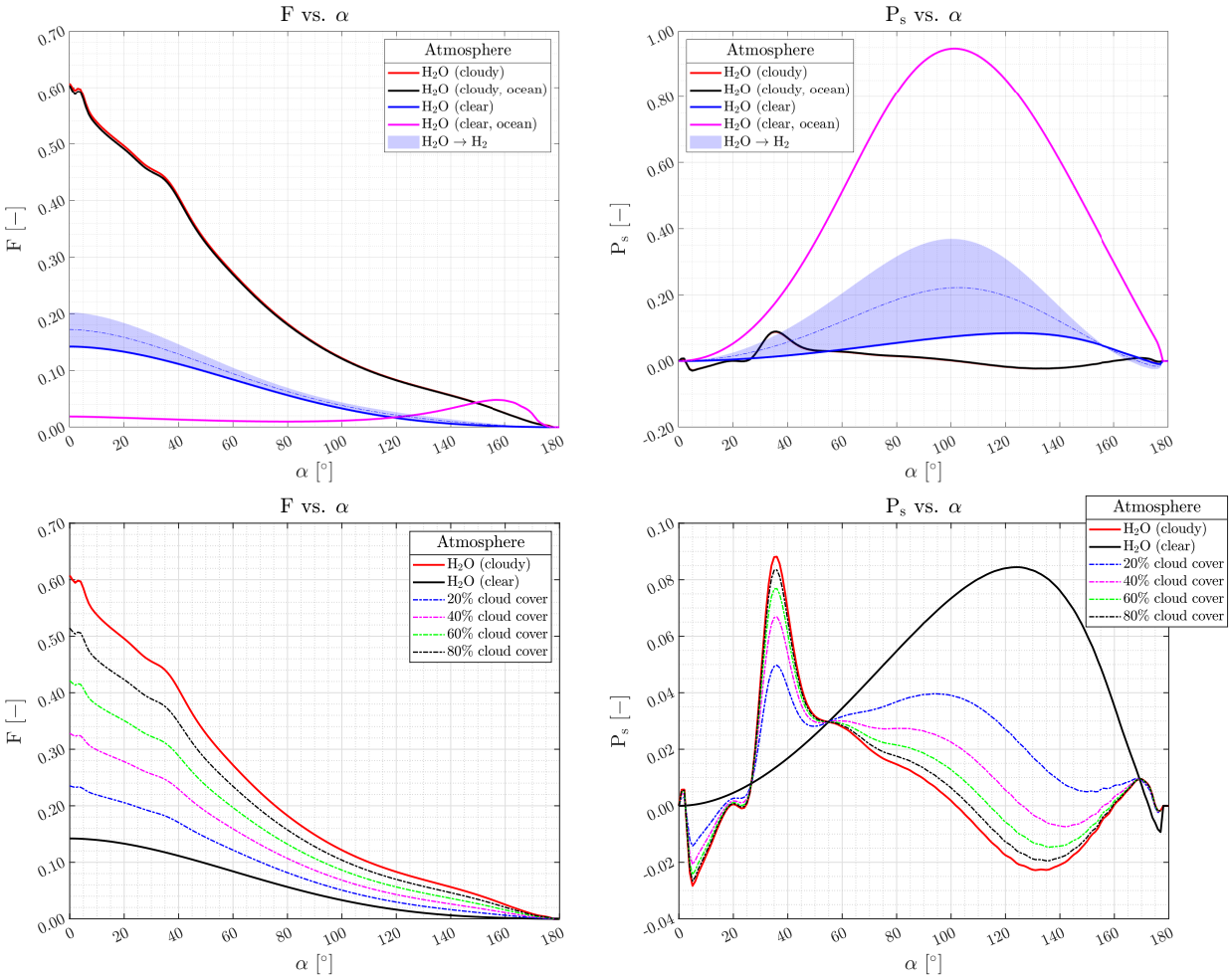


Figure 4.13: Similar to Fig. 4.11, except for planet-1d. The most likely atmospheric composition here is $H_2O$. The wind speed for the ocean case is $v = 7\ m/s$.

Fig. 4.13 is similar to Fig. 4.11 in terms of likely composition ($H_2O$) and features, differing in atmospheric profile and orbital properties. As such, what was said for planet 1b also holds for planet 1d. Despite the planets having the same composition, their curves are not identical, as they differ in gravitational acceleration and surface temperature, both of which affect the planet's pressure profile. For instance, the peak of the $P_s$ curve for a water vapor atmosphere in Fig. 4.13 is about 0.081, while in Fig. 4.11, it is about 0.058.

The main difference between these two planets is that planet-1d could have an ocean, modeled here as a Fresnel reflecting surface with a wind speed of 7 $m/s$. When compared to the non-ocean $F$ curves, the Fresnel reflecting ocean surface has a much lower normalized reflected flux for low and medium phase angles (we can see this in the top left plot of Fig. 4.13 at about $\alpha < 120°$), as it behaves like a Lambertian surface, in addition to having a surface albedo of zero, then experiences a spike in $F$ at large phase angles, due to the ocean glint, overtaking the other curves, as per the discussion of Fig. 4.6. In the $P_s$ plot, the ocean planet case is expressed as a bell-shaped, almost symmetric curve (though slightly skewed to the right), with large values of $P_s$ similar to those of a planet with a black surface.

Adding a cloud layer to the atmosphere of an ocean-covered planet increases $F$ [64]. When adding a cloud deck over an ocean surface planet, the $F$ and $P_s$ signals are almost similar to signals of a cloudy planet above a dry surface, overshadowing the presence of an ocean.

Similar to Fig. 4.11, the second row of Fig. 4.13 shows the $H_2O$ atmosphere with a variable horizontal cloud cover fraction, in increments of 20%. Also similarly the more we increase the cloud coverage, the more the $F$ and $P_s$ curves resemble the completely cloudy case, where the former increases for all phase angles and the latter undergoes a more uneven change, increasing for some phase angles and decreasing for others. With increasing cloud cover, the rainbow peak becomes sharper and the role of the atmospheric gas in $P_s$ diminishes, as seen by the change in the curvature of $P_s$ at $\alpha \approx 55 - 170°$.

**Planet Trappist-1e**

Planet-1e is the central planet of Trappist-1's habitable zone. It is a rocky planet that is believed to have a surface ocean and clouds. Its atmosphere is most likely water vapor, though a fraction of carbon dioxide is believed to be present as well. In Fig. 4.14, the $F$ and $P_s$ signals are shown for the most likely atmospheric compositions, with and without clouds. The curves are for one atmospheric layer, with a Fresnel reflecting ocean surface, an assumed surface pressure $p_s = 1\ atm$, for a wavelength of $1.15\ \mu m$.

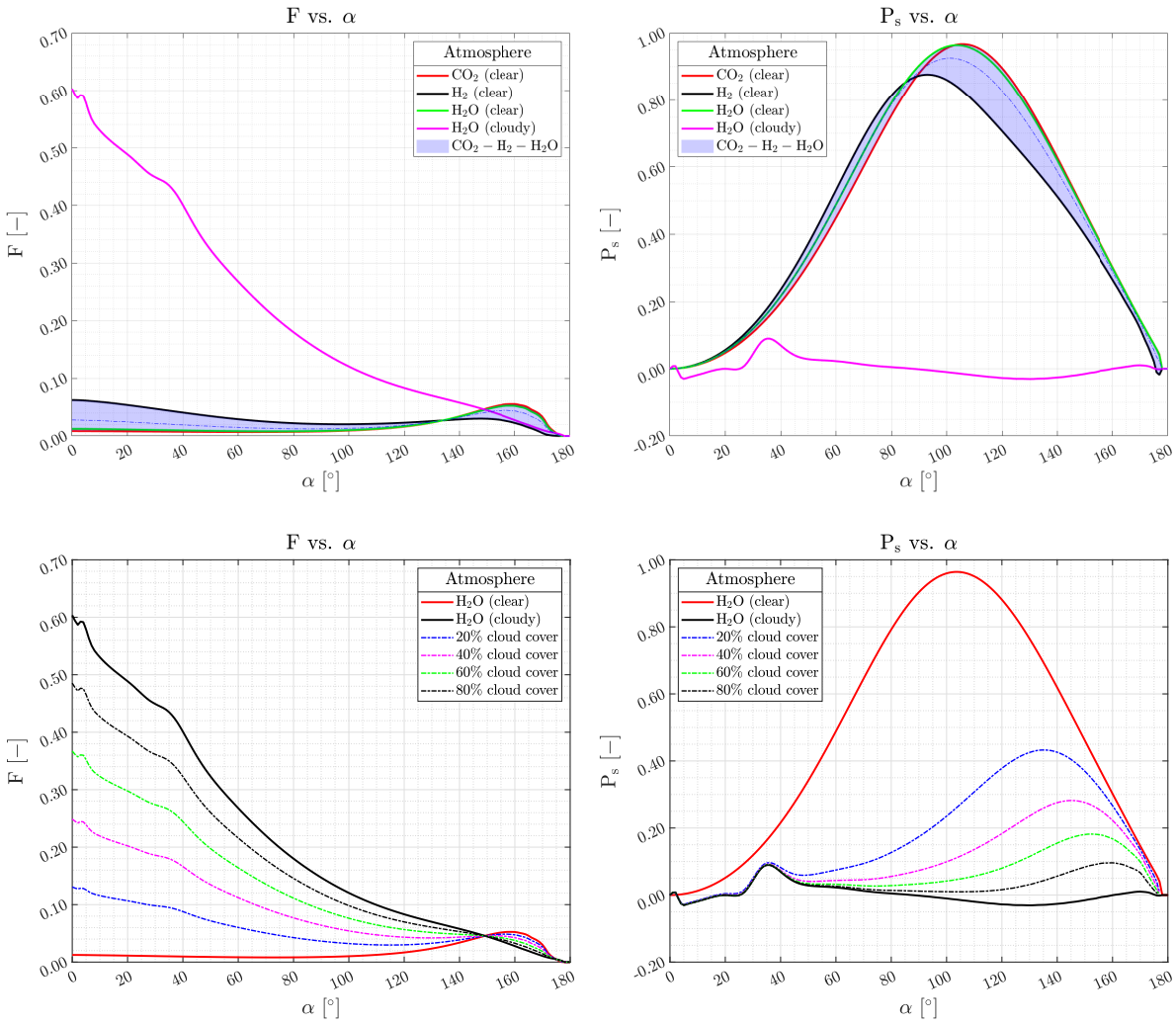


Figure 4.14: Similar to Fig. 4.11, except for planet-1e. The most likely atmospheric composition here is $H_2O$. The varying atmospheric compositions which make up the shaded region are as follows: $H_2O$ (green), $H_2$ (black), $CO_2$ (red).

Figure 4.14 is similar to Fig. 4.13 in terms of likely composition ($H_2O$) and features, differing in atmospheric profile and orbital properties. As such, what was said for planet 1d also holds for planet 1e. According to the models, planet-1e probably holds a surface ocean, for which an atmospheric composition of $H_2O$ is most likely, though partial compositions of $H_2O$, $H_2$, and/or $CO_2$ are believed to exist.

Unlike previous figures, the $P_s$ plot shows overlapping partial composition curves (and not above one another, like in Figs. 4.11, 4.12), due to accounting for an ocean which skews these figures to the right, rather than move them upwards, where a larger molecular mass causes a larger skew. This is yet another detail that is found in the $P_s$ curve which would otherwise go unnoticed in the $F$ curves, highlighting the importance of including the degree of polarization curves when observing exoplanets.

However, in the $F$ plot, the curves are aligned following the trend of a black surface in Fig. 4.3, where a lighter gas would have a larger $F$. This trend is coupled with that of the glint, where at a certain phase angle, all the ocean curves intersect and their trends are flipped, forming a peak due to the glint. Heavier gases form sharper peaks. In other words, the behaviour of the $F$ curves for a varying gas molecular mass resembles that of a varying wind speed, where a heavier gas has the trend of a lower wind speed (so starts with the lowest value of $F$, which then increases with phase angle until crossing, after which it has the highest value of $F$), and vice-versa.

Similar to the previous figures, the second row of Fig. 4.14 shows the $H_2O$ atmosphere with a variable horizontal cloud cover fraction, in increments of 20%. The higher the cloud coverage, the more the $F$ and $P_s$ curves resemble the completely cloudy case, where $F$ increases for all phase angles and $P_s$ increasing for some phase angles and decreasing for others. Also, when the cloud cover increases, the rainbow peak becomes sharper and the role of the atmospheric gas in $P_s$ diminishes, as seen by the change in the curvature of $P_s$ at $\alpha \approx 55 - 170°$.

**Planet Trappist-1f**

Planet-1f is the second outer planet to Trappist-1 and possibly the outermost planet of its habitable zone. It is a rocky planet that could possibly bear clouds, and to a much lesser extent, a surface ocean. Its atmosphere is thought to consist mostly of nitrogen gas, though a water-hydrogen mixture is possible. The case for the surface ocean is included in Fig. 4.15. The curves are for one atmospheric layer, with a surface albedo of $A_s = 0.2$, and an assumed surface pressure $p_s = 1\ atm$. The wavelength is $1.15\ \mu m$.

The main difference between planet 1f and planets 1d and 1e is the atmospheric composition, which is most likely $N_2$ for 1f, and gravitational acceleration. As such, what was said for planet-1e concerning the ocean surface holds for planet-1f. Similarly, what was said for 1d concerning the atmospheric composition holds for 1f, though the atmosphere here is $N_2$, which is an increase in gas molecular mass, compared to an $H_2O$ atmosphere for 1d (for the case without an ocean). Thus, the $P_s$ is expected to be lower, and $F$ is expected to be higher, since the surface is non-black. In a similar vein, the gravitational acceleration increases when going from 1d to 1f, also accounting for a lower $P_s$ and a higher $F$. The reader is referred to the discussion for Figs. 4.3 and 4.4 for an account of how atmospheric molecular mass and gravitational acceleration affect $F$ and $P_s$.

Similar to the previous figures, the second row of Fig. 4.15 shows the $N_2$ atmosphere with a variable horizontal cloud cover fraction, in increments of 20%. Also similarly, the higher the cloud coverage, the more the $F$ and $P_s$ curves resemble the completely cloudy case, where $F$ increases for all phase angles and $P_s$ increasing for some phase angles and decreasing for others. For a higher cloud cover, the rainbow peak becomes sharper and the role of the atmospheric gas in $P_s$ diminishes.

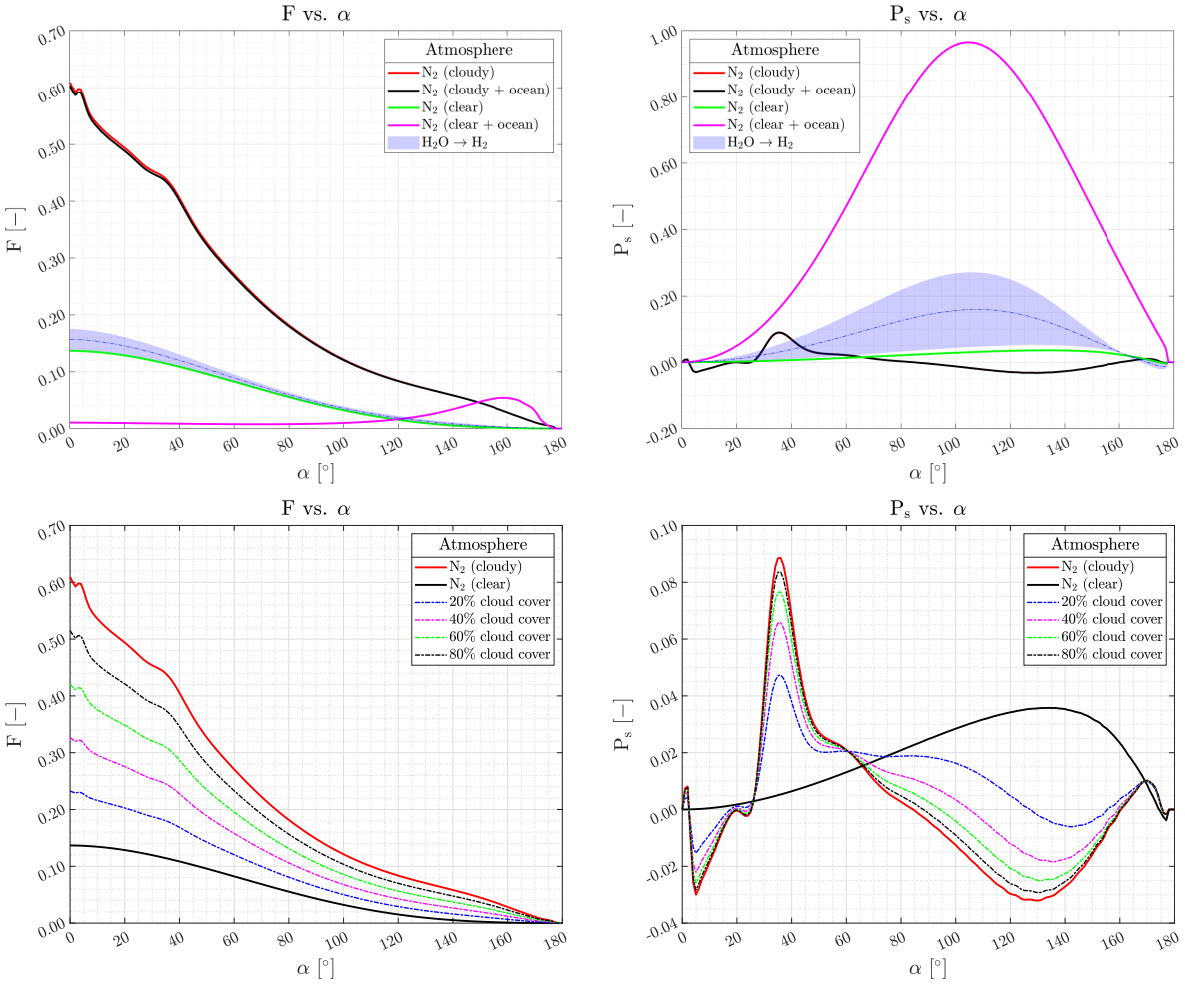


Figure 4.15: Similar to Fig. 4.13, except for planet-1f. The most likely atmospheric composition here is $N_2$. The wind speed for the ocean case is $v = 7\ m/s$.

### Planet Trappist-1g

Planet-1g is the second furthest planet to Trappist-1. It is a rocky planet that could possibly bear clouds, though most likely does not bear a surface ocean due to its low surface temperature. Its atmosphere is thought to consist mostly of nitrogen gas, though a water-hydrogen mixture is possible. The signals for planet 1g are presented in Fig. 4.16. The curves are for one atmospheric layer, with a surface albedo of $A_s = 0.2$, and an assumed surface pressure $p_s = 1\ atm$. The wavelength is $1.15\ \mu m$.

Figure 4.16 is similar to Fig. 4.15 in terms of likely composition ($N_2$) and features, differing in atmospheric properties. As such, what was said for 1f for the non-oceanic surface also holds for 1g. The gravitational acceleration slightly increases when going from 1f to 1g, accounting for a lower $P_s$ and a higher $F$. The reader is referred to the discussion for Figs. 4.3 and 4.4 for an account of how the gravitational acceleration affects $P_s$.

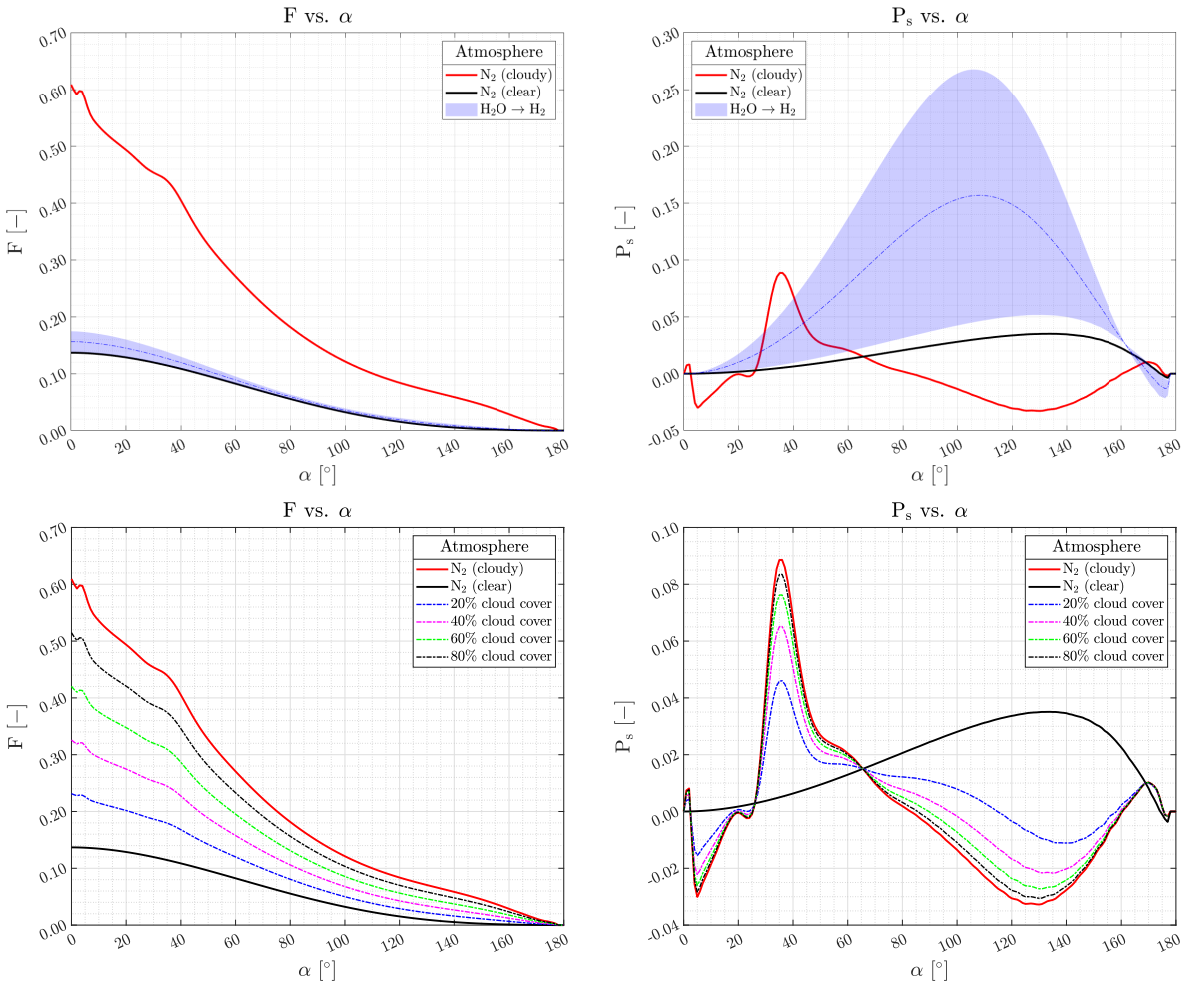


Figure 4.16: Similar to Fig. 4.11, except for planet-1c

### Planet Trappist-1h

Planet-1h is the outermost planet of the Trappist-1 system, and as a result probably has the lowest surface temperature. It is a rocky planet that most likely bears no clouds or surface ocean due to its low temperature. Its atmosphere is thought to consist mostly of nitrogen gas, though a water-hydrogen mixture is possible. The signals for 1h are presented in Fig. 4.17.

The curves are for one atmospheric layer, with a surface albedo of $A_s = 0.2$, and an assumed surface pressure $p_s = 1\ atm$. The wavelength is $1.15\ \mu m$. Fig. 4.17 is similar to Fig. 4.16 in terms of likely composition ($N_2$) and features, differing in atmospheric profile and orbital properties. As such, what was said for 1g also holds for 1h. The gravitational acceleration decreases when going from 1g to 1h, accounting for a higher $P_s$ and a lower $F$, when compared to 1g. The reader is referred to the discussion for Figs. 4.3 and 4.4 for an account of how the gravitational acceleration affects $P_s$.

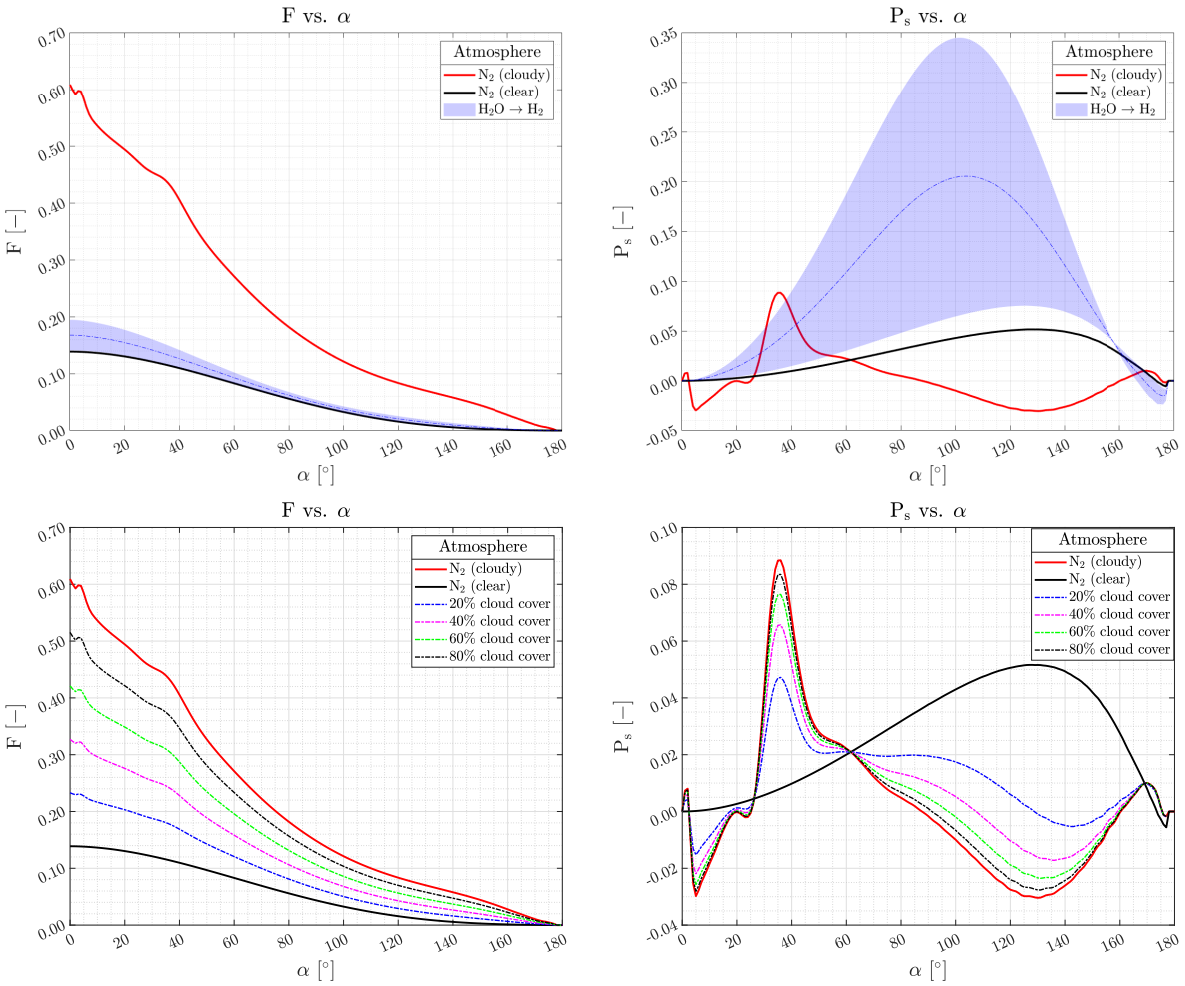


Figure 4.17: Similar to Fig. 4.11, except for planet-1h.

## 4.3. Flux and polarization signals of the Trappist-1 system

Here, we present the reflected total fluxes and degree of polarization for the Trappist-1 system as a whole, thus the combined signals of the seven planets and the star. Also, unless otherwise stated, all plots in this section begin at Julian day $T_0 - 2,450,000 = 7282.8087\ BJD_{TDB}$, corresponding to the earliest mid-transit time of the planet-1c, during the observation survey of Delrez et al. [9]; however, a delay period of 7 days was added to this so the main features can fit into the plots of the outermost planets. The arbitrary time duration of 10 days is large enough to show the orbital variations of the planets, while being sparse enough to identify certain features with the naked eye.

Note that in this section, $F$ denotes the reflected flux in $W/(m^2\ m)$, and thus not the normalized reflected flux like in the previous section, because here, the sizes of the individual planets and their distances to their parent star are important. In addition, we assume that the observed degree of polarization is not subject to Earth's atmospheric extinction [64].

The computation of the reflected flux $F$ and $P_s$ of the system as a whole are explained as follows. The scenario of 'Earth-like planets with black surfaces' is used for demonstration.

Figure 4.18 shows signal curves for the black surface Earth-like planets. This scenario is akin to that of Fig. 4.1, so we interpolated the normalized reflected flux variation with phase angle from Fig. 4.1 to fit our phase angles, which vary with time (the phase angle variation with time is shown in Fig. 3.2). Then, this normalized reflected flux (in $[-]$) is substituted into Eq. 3.7 as the first term in the $\mathbf{S}(\lambda,\ \alpha)$ matrix, where it is multiplied by the stellar surface flux $\pi B_0$ $[W/(sr\ m^2\ m)]$, and then scaled with respect to

the stellar radius, the planet semi-major axis, the planet radius, and the planet distance to observer. The output of this equation is the stellar flux reflected by a planet arriving at an observer, or simply the reflected flux, given as $F\ [W/(sr\ m^2\ m)]$. The same can be said for computing the reflected flux $Q$. For the whole system including the star, the degree of polarization includes the stellar flux, since planets are so close to their parent star, $P_{system+star} = -\frac{\sum Q_i}{F_{star}+\sum F_i}$, with $F_{star}\ [W/(sr\ m^2\ m)]$ the stellar flux and $i$ the planet index. The star's polarized flux is not present in the above equation as starlight is assumed to be unpolarized.

### Earth-like planets with black surfaces

First, the case of having seven planets with black surfaces ($A_s = 0$) and Earth-like atmosphere compositions (in terms of depolarization factor $\delta_{air}$, refractive index $n_{air}$, surface pressure $p_s$, top-of-atmosphere pressure $p_{top}$, and atmospheric gas molecular mass $M_u$) is considered. However, the planets vary in gravitational acceleration, radius, and semi-major axis, which are the exact values of the respective Trappist-1 planets. The properties of these planets are summarized in Table 4.3, and the curves are plotted in Fig. 4.18. The planetary eclipses have been included. Figure 4.19 shows the $F$ and $P_s$ plots for 1e only, and is the same as Fig. 4.18, with the only difference being that in the latter figure, 1e has a surface ocean and a wind speed of 7 $m/s$.

| **Parameter** | **Value** |
|---|---|
| Wavelength | $\lambda = 1.15\ \mu m$ |
| Depolarization factor | $\delta_{air} = 0.03$ (@$1.15\mu m$) |
| Surface albedo | $A_s = 0$ |
| Air refractive index | $n_{\mathrm{air}} = 1.0$ |
| Surface pressure | $p_s = 1\ atm$ |
| Top of atmosphere pressure | $p_{top} = 0\ atm$ |
| Molecular mass | $M_{\mathrm{u}} = 29\ amu$ |
| Ocean | No |
| Clouds | No |
| **Variable Parameters** | |
| Gravitational acceleration | $g$ |
| Radius | $R$ |
| Semi-major axis | $a$ |

Table 4.3: Table showing the parameters used for this computation, and their values. The "variables parameters" entry implies each Trappist-1 planet has its own value, as per Tables 2.1 and 2.2.

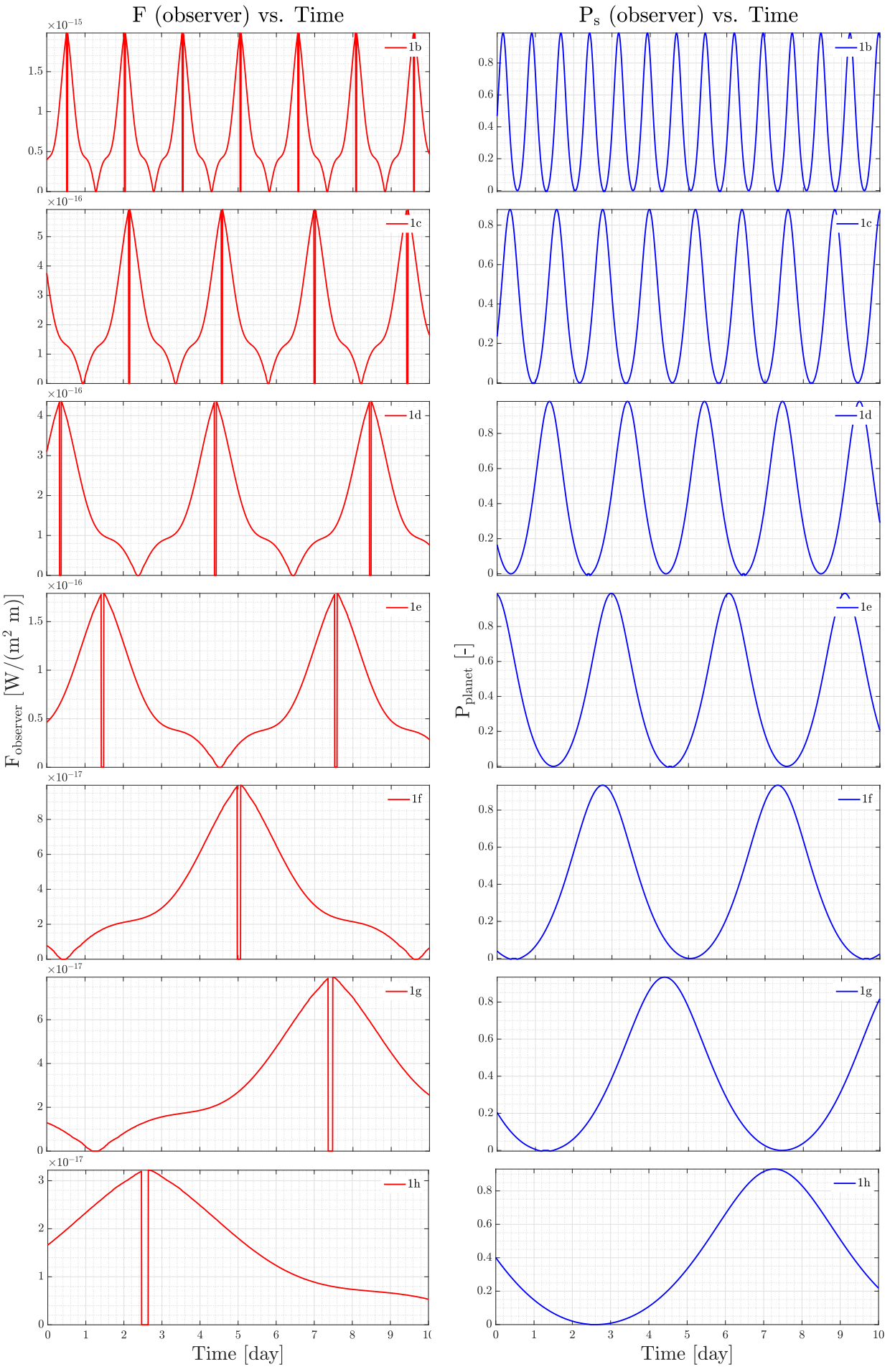


Figure 4.18: The total fluxes $F$ (left) and the degree of polarization $P_s$ (right) of starlight reflected by the individual Trappist-1 planets, modeled as having black surfaces and gaseous atmospheres, as functions of time. This is the reflected light that is received by the observer on Earth. Planet-1e is modeled as a dry planet. From top to bottom: planet-1b, 1c, 1d, 1e, 1f, 1g, and 1h.

From Fig. 4.18 the following can be noticed:

The $F$ and $P_s$ curves look similar in shape to the ones from Section 4.2, though they look tighter due to the phase angle-time dependency (compared to the phase angle dependency previously). Both $F$ and $P_s$ curves look symmetric, as the phase angle $\alpha$ goes up to $180°$, after which it drops in the same manner. This symmetry occurs for a planet whose orbit is circular, thus having constant orbital velocity, which is the case for all Trappist-1 planets due to the close proximity to their parent star.

The reflected flux curves drop in value when going from 1b to 1h. This is due to the increasing distance from the parent star $D$, for which the stellar flux arriving at the planet decreases, as shown in Eq. 3.7. Another factor contributing to the change in $F$ is the planet radius $r$, for which $F$ is inversely proportional, so its effect on $F$ is opposite to that of the planet's distance from the star. However, since $D$ increases by a larger amount than the increase $r$ (when comparing adjacent planets, going from 1b to 1h), then the reflected flux for Trappist-1 planets depends more on the planets' distance from their parent star, and so $F$ decreases when going from 1b to 1h. Information on the effect of each planets' size and orbital distance on the reflected and polarized fluxes is shown in Table 4.4.

The degree of polarization $P_s$ on the other hand, is not directly affected the planet size and orbital parameters (though these indirectly affect the planet's surface and atmospheric properties, i.e., composition and gravitational acceleration), but depends on the atmosphere and surface properties, since it equals $P_s = -Q/F$, so the physical and orbital terms cancel out.

The effect of the eclipse is not as noticeable on $P_s$ as it is on $F$; this is because for the eclipse angles (at which the phase angles are smallest) $P_s$ is already very small, so its drop to 0 is not as noticeable as that of the reflected flux.

When comparing Fig. 4.18 e to Fig. 4.19, we see that the $F$ curve undergoes a sharp increases for large phase angles (taking the eclipse feature to be at $\alpha = 0°$), due to the ocean glint. This increase in $F$ due to the glint causes the curve to exceed that of 1b (with the maximum $F \approx 2 \times 10^{-15}$ for 1b and $F \approx 6 \times 10^{-15}$ for 1e). Also, in the presence of an ocean, the $P_s$ curve undergoes a skew from its original bell-shape, which is also due to having an ocean, as per the discussion of Fig. 4.6.

Note that the reflected flux of 1b is in the order of $10^{-15}$, while that of 1h is in the order of $10^{-17}$. These planets have different radii and orbital distances, where 1b's radius is 1.45 times that of 1h and its orbital distance is 0.186 that of 1h, so from Eq. 3.7, its contribution to $F$ is $(1.45/0.186)^2 \approx 61$ times higher than that of 1h, based on orbital and size parameters only (the rest of the differences are from the normalized reflected flux).

| **Scaling factor** | **1b** | **1c** | **1d** | **1e** | **1f** | **1g** | **1h** |
|---|---|---|---|---|---|---|---|
| $r_{1b}/r$ | 1.00 | 1.02 | 1.43 | 1.23 | 1.07 | 0.98 | 1.45 |
| $D_{1b}/D$ | 1.00 | 0.73 | 0.52 | 0.39 | 0.30 | 0.25 | 0.19 |
| $(r_{1b}/r)^2 / (D/D_{1b})^2$ | 1.00 | 1.97 | 7.61 | 9.75 | 12.78 | 15.71 | 60.50 |

Table 4.4: Table showing the effect that size and orbital distance of the Trappist-1 planets have on the reflected and polarized fluxes, as per Eq. 3.7, with respect to 1b.

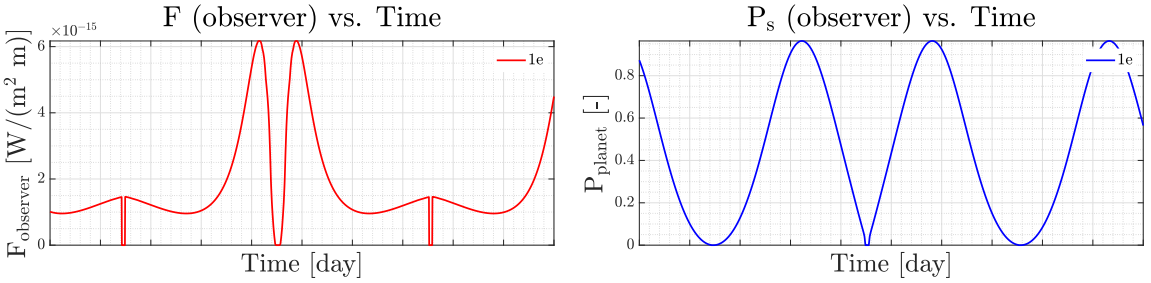


Figure 4.19: Similar to Fig. 4.18 e, but considering an ocean for 1e with wind speed of 7 $m/s$.

Fig. 4.20 shows the degree of polarization for the Trappist-1 system, according to the parameters of Table 4.3, and does not have an ocean for 1e. The figure shows the system with (bottom) and without (top) including stellar flux, with (right) and without (left) considering the eclipse, as a function of time. Eq. 3.14 was used to compute the curves in the following figure.

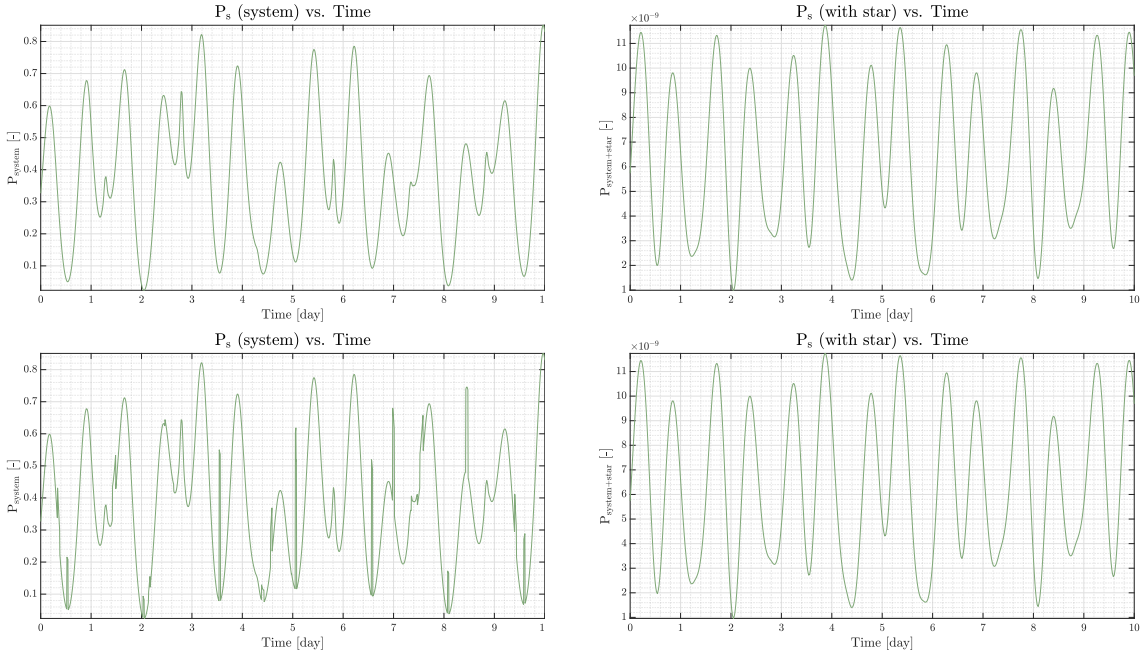


Figure 4.20: The degree of polarization of the Trappist-1 system as a whole, with (bottom) and without (top) including stellar flux, with (right) and without (left) considering the eclipse, as a function of time. All planets are modeled as having black surface with Earth-like atmospheres, and no clouds or oceans. This figure is associated with Fig. 4.18

From Fig. 4.20

1. System without star, no eclipse (top left):
   - The deepest troughs in this figure occur at times analogous to peaks in $F$ for 1b (in Fig. 4.18). This makes sense, as 1b is the biggest contributor to this plot due to how close it is to the star, and because $P_s$ is inversely proportional to $F$, so for the largest values of $F$ (peaks), the system $P_s$ curve undergoes a minimum.
   - Planet 1b having the highest contribution does not imply that the peaks and troughs seen in this plot are analogous to those of 1b. Since this plot shows the sum of all planet signals, other planets play a role as well, though this contribution decreases for each successive planet after 1b, mainly due to increasing orbital distance. For example, at about 2.8 days in Fig. 4.18, 1b undergoes a minimum, but in this figure, it it is met with a small peak, while at about 3.4 days, the curve undergoes its largest peak, due to the constructive interference of other planet curves, 1c (undergoing a minimum in $F$), and 1b having a relatively low value of $F$ at this point.

- Given that the individual planets have their signals already computed, the shape of the signal of the entire system depends on the orbit ephemeris of the planets. So, if we chose a different initial time, the curves would add differently, depending on the planet position at such time. Implications of this include different peak heights.

2. System without star, with eclipse (bottom left):
   - The system curve with an eclipse looks identical to the one without an eclipse, with the addition of narrow vertical spike features. These features are due to the eclipse of each planet, with their vertical height and width depending on the planet; a planet of higher contribution to the signal, such as 1b, is expected to have a higher spike, due to having a higher $F$ (so a sudden drop in $F$ causes a rise in $P_s$). Note that the reverse does not always hold true; this means that a high spike does not imply a planet of higher contribution, as many planets could be eclipsing at once. This is shown in Fig. 4.18 at 5 days, where the eclipses of 1b and 1f are overlapping.
   - The width of the eclipse spike is proportional to the time during which the planet was orbiting behind its parent star. This time increases with increasing distance from the star, and so the spike gets progressively wider when going from 1b to 1h. For instance, the spike at 8.4 days, considerably wider than other ones, is due to the eclipse of 1d. The height of this feature is particularly large as the $F$ signals of the innermost planets (1b and 1c) is low, so we see a big jump. Looking at 3.5 days for example, we see a very noticeable peak, which occurs when 1b is undergoing an eclipse. Its unusual size is attributed to 1c having a minimum $F$ at this time as well (due to having a phase angle of 180°). Another example occurs at 5 days, which shows another peak due to 1b, whose prominence is due to the constructive interference of 1b and 1f (both eclipsing), and 1e having a considerably low value of $F$.
   - Since the eclipse width is due to orbital distance (increases with increasing distance), and since a planet's contribution to the system signal is also affected by its orbital distance (decreases with increasing distance), we do not expect to clearly notice the eclipse effect of the farthest planets like 1g or 1h.
3. System with star, without eclipse (top right):
   - As previously mentioned, adding the starlight to the system results in the following degree of polarization : $P_{system+star} = -\frac{\sum Q_i}{F_{star}+\sum F_i}$, where starlight is assumed to be unpolarized, so does not have a polarized flux component $Q$. From a numerical perspective, this tells us that the total $P_s$ of the system will greatly decrease since the starlight is added to the denominator. This dilutes the features, leaving only those of the inner planets (1b, 1c, and 1d) visible, such as the most prominent peaks and troughs.
4. System with star, with eclipse (bottom right):
   - There is no visual difference between the curve for the system and star with and without eclipse, most likely due to the dilution of the signal features caused by adding the stellar flux into the denominator.

Fig. 4.21 is similar to Fig. 4.20, with the addition of an ocean on 1e, and an associated wind speed of 7 $m/s$. The figure shows the system with (bottom) and without (top) including stellar flux, with (right) and without (left) considering the eclipse, as a function of time.

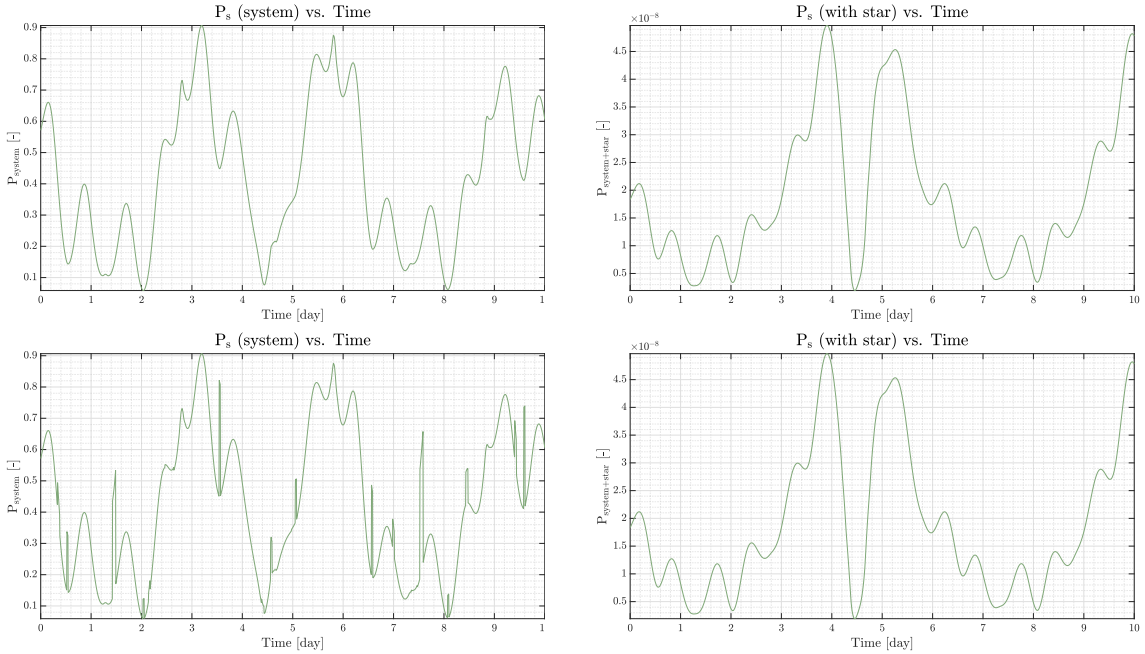


Figure 4.21: Similar to Fig. 4.20, but with 1e having an ocean (and wind speed of 7 $m/s$). This figure is associated with Fig. 4.18

From Fig. 4.21

1. System without star, no eclipse (top left):
    - The general shape of the curve resembles that of 1e, due to being dominated by the signal of 1e, which in turn, is due to the presence of the ocean. As such, the peaks and troughs are still present, though their magnitude dropped; an exception to this are the features located where the glint feature picks up, so for the range of 3-4.5 days, and their symmetric counterpart (4.5-6 days), in Fig. 4.19.
2. System without star, with eclipse (bottom left):
    - The eclipse features for 1e (at about 1.4 and 7.6 days) are now most prominent, due its increased contribution to the signal after adding the ocean. Furthermore, the $P_s$ of the system greatly increases in the presence of an ocean (by about a factor of 5 when compared to the case without an ocean).
3. System with star, without eclipse (top right)
    - Similarly to what has been said previously, adding the stellar flux dilutes some features. This current plot has the outline of that of 1e, indicating its importance, and the difference adding an ocean makes.
4. System with star, with eclipse (bottom right)
    - Similarly to what was said previously, there is no visual difference caused by considering the eclipse effect for this scenario, probably because of the dominance by the stellar flux of the signal.

Fig. 4.22 shows the signal curves from Figs. 4.20 and 4.21, to illustrate the difference an ocean makes. The figure shows the system with (bottom) and without (top) including the eclipse, for a system with (right) and without (left) stellar flux, as a function of time.

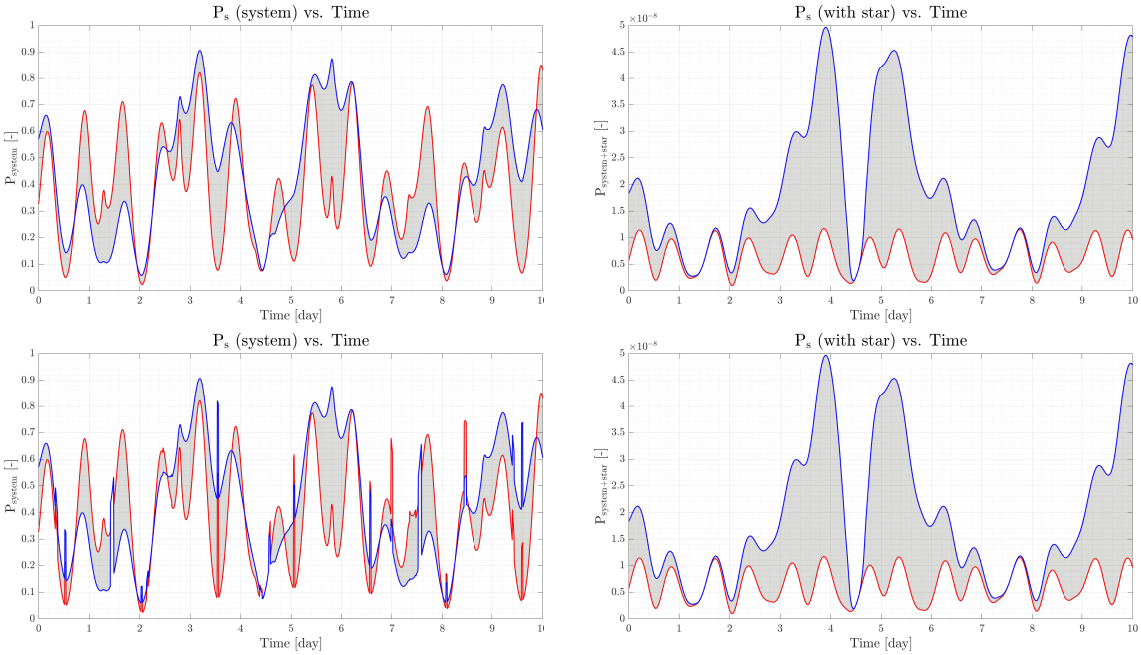


Figure 4.22: Figure showing the degree of polarization of the Trappist-1 system with all black surfaces and 1e having a black dry surface (red line), and the same system but with 1e having a surface ocean (blue line). The grey area is the difference between the two curves, i.e., the difference an ocean makes, so its effect on the system. The figure shows the system with (bottom) and without (top) including the eclipse, with (right) and without (left) including stellar flux.

Fig. 4.22 shows the system $P_s$ curves, illustrating the difference in signal an ocean makes. Since these plots simply combine the previous ones (Figs. 4.21 and 4.20), the main discussion points are mentioned above.

Similarly to what was previously said, the presence of an ocean quashes some features like peaks in the $P_s$ plot. Also, when the $F$ signal of 1e is 0, we expect both curves to meet, as it is the differing factor between these curves. Indeed, this happens when 1e reaches a phase angle of 0° and undergoes each of two eclipses (see Fig. 4.19 and ), occurring at 4.6, 1.4, and 7.6 days respectively.

### Trappist-1 planets without clouds

Next, we consider the case of having seven planets with non-black surfaces and atmosphere compositions corresponding to those of the Trappist-1 planets (in terms of depolarization factor $\delta_{air}$, refractive index $n_{air}$, surface pressure $p_s$, top-of-atmosphere pressure $p_{top}$, and atmospheric gas molecular mass $M_u$). Similar to the previous scenario, the planets vary in gravitational acceleration, radius, and semi-major axis, which are the exact values of the respective Trappist-1 planets. The properties of these planets are summarized in Table 4.5, and the curves are plotted in Fig. 4.23. The planetary eclipses have been included.

| Parameter | Value |
|---|---|
| Wavelength | $\lambda = 1.15\ \mu m$ |
| Surface pressure | $p_s = 1\ atm$ |
| Top of atmosphere pressure | $p_{top} = 0\ atm$ |
| Ocean | 1e |
| Clouds | No |
| **Variable Parameters** | |
| Surface albedo | $A_s$ |
| Depolarization factor | $\delta$ |
| Molecular mass | $M_u$ |
| Air refractive index | $n$ |
| Gravitational acceleration | $g$ |
| Radius | $R$ |
| Semi-major axis | $a$ |

Table 4.5: Similar to Table 4.3, but for Trappist-1 planets characteristics. The “variables parameters” values are found in Table 2.1 and 2.2. The atmospheres of the planets (from 1b to 1h) are composed of the following gases: $H_2O$, $O_2$, $H_2O$, $H_2O$, $N_2$, $N_2$, and $N_2$.

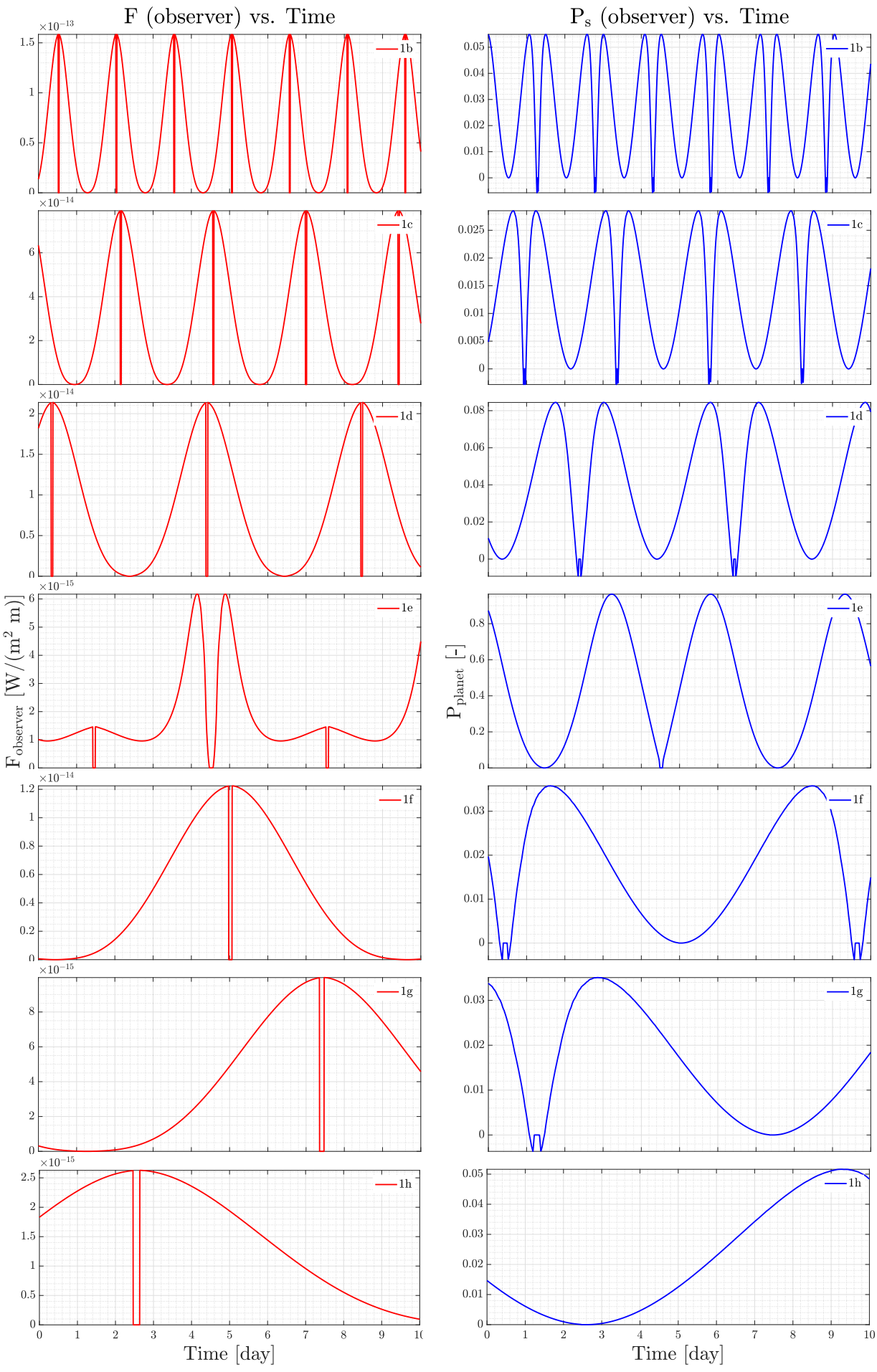


Figure 4.23: Similar to Fig. 4.18, but for the real Trappist-1 planets (in terms of surface albedo, atmosphere), all of which are considered cloudless. Note that 1e has an ocean and wind speed of 7 $m/s$.

From Fig. 4.23, we can see that the $F$ curves have increased by about two orders of magnitude for each planet, while their $P_s$ curves have decreased by a factor of 12-40, when compared to Fig. 4.18. This is due to the change in surface albedo and atmospheric composition, where the former accounts for most of the changes (see discussion of Fig. 4.2). As such, 1e no longer has the highest $F$, and is thus no longer the major contributor to $P_s$.

The fork-like shape in the $P_s$ plots of Fig. 4.23 occurs at the largest phase angles, or during transit (so it is not related to the eclipse), where this negative polarization is characteristic for light that was scattered twice by molecules in the planetary atmosphere (see the discussion of Fig. 4.1). This feature varies in size depending on many factors, such as atmospheric molecular mass (dip increases for lighter gases), surface albedo (dip decreases for increasing albedo). In the discussion of Fig. 4.1 we mentioned that when reflection is near the backward ($\alpha \approx 0°$) and forward directions ($\alpha \approx 180°$), the dependence of $P_s$ on $\alpha$ is not affected by the atmospheric characteristics, so $P_s = 0$ at those angles. We are only interested in large phase angle values, so when $\alpha \approx 180°$. This would result in a flattening of the $P_s$ curve, for instance at about 1.2-1.4 days for 1g. Due to orbital symmetry, the $P_s$ curve is flipped after $\alpha = 180°$, so we end up with two consecutive dips, forming a feature that looks fork-like.

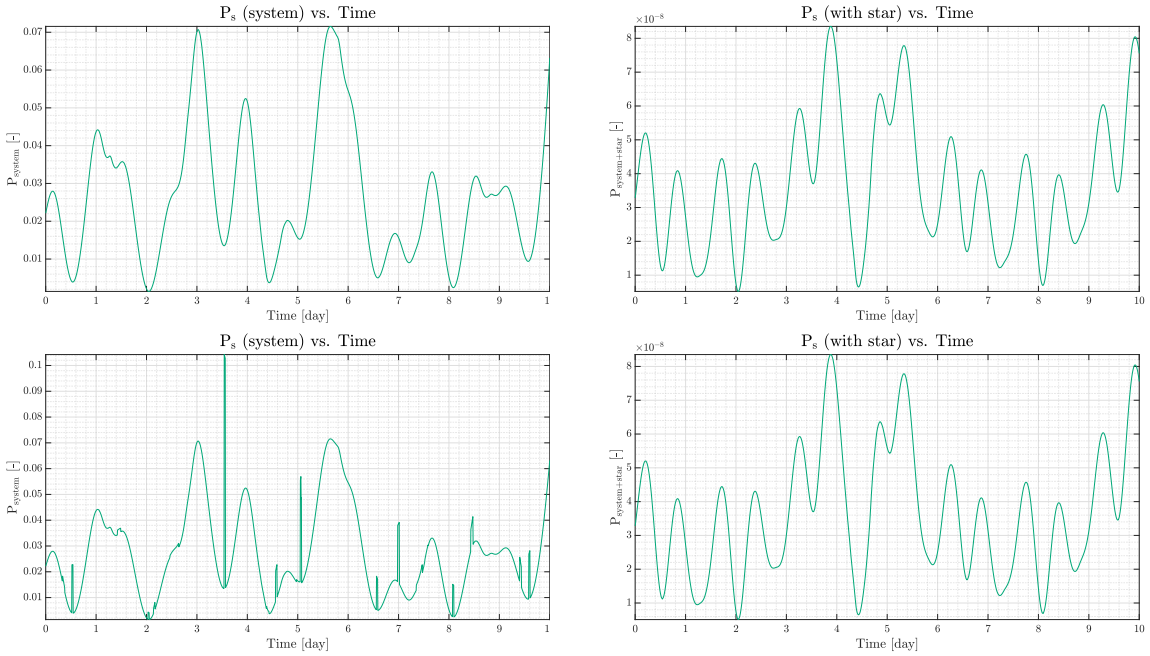


Figure 4.24: The degree of polarization of the Trappist-1 system as a whole, with (bottom) and without (top) including stellar flux, with (right) and without (left) considering the eclipse, as a function of time. The planets in this system have the most likely composition and surface feature, as per Table 2.2, though none has clouds. Note that 1e has an ocean and wind speed of 7 $m/s$. This figure is associated with Fig. 4.23.

From Fig. 4.24

1. System without star, no eclipse (top left):
    - The location of the troughs and peaks remains the same when comparing with Fig. 4.20, though some are now not as noticeable than others.
2. System without star, with eclipse (bottom left):
    - The $P_s$ plot of the system without star is much smaller now, reaching a peak value of 0.07, as opposed to values of 0.9 in Fig. 4.20, mainly due to the change in surface albedo.
    - The height of the spike changes depending on the surface albedo and atmospheric composition of planets; for instance, the feature of 1b (at about 3.5 days) is considerably longer

now than in Fig. 4.20 (relative to the curve amplitude).

3. System with star, without eclipse (top right)
    - When considering an ocean, some features subside, and it becomes clearer that the shape of the plot strikes a resemblance to that of 1e. this is because 1e has a high $P$, with a
4. System with star, with eclipse (bottom right)
    - Similar to previous scenarios, this plot looks identical to its non-eclipse counterpart.

Fig. 4.28 shows the degree of polarization for the cloudy Trappist-1 system with 1e being an ocean planet with an atmosphere, as well as the degree of polarization for the exact same system, but with 1e having a black surface with an atmosphere and no ocean, in order to illustrate the difference in signal an ocean makes.

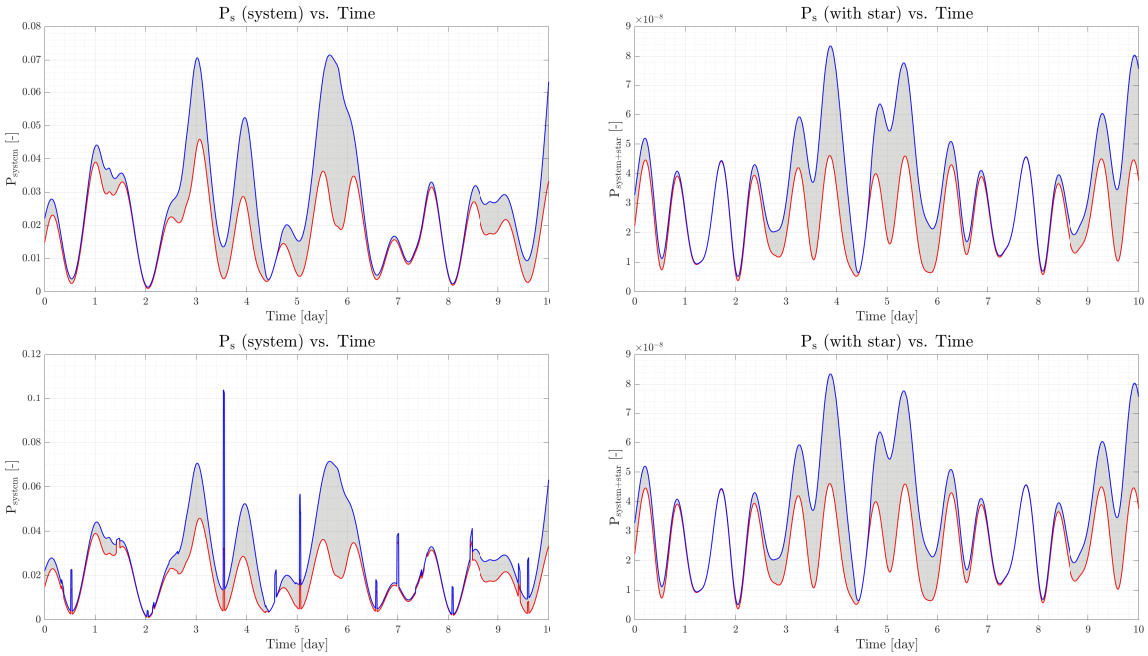


Figure 4.25: Similar to Fig. 4.22, this figure shows the degree of polarization of the Trappist-1 system for all cloudy planets and 1e having an ocean (blue line), and for the same system but with 1e having no ocean (red line). The plots are placed with (top) and without (bottom) eclipses, for the system with (right) and without (left) the star.

Similar to Fig. 4.22, Fig. 4.25 shows the system $P_s$ curves. The figures are different as the former is for the Trappist-1 planets modeled as black surfaces with atmospheres, while this scenario considers the actual surface and atmospheric composition of the planets. In this figure, the only difference between the two curves is the presence of an ocean on 1e (the red line is for 1e modeled as a black surface with an atmosphere, and the blue line is for 1e modeled as an ocean planet with the same atmosphere), thus the grey shaded area illustrates the difference in signal this ocean makes.

From Fig. 4.25, we see that for a cloudless system, having an ocean increases the total system $P_s$ at every instance when compared to the same system but with 1e having no ocean, mainly due to the ocean surface. When observers view the system, they actually see the $P_s$ of total system and its star, so the plots on the right are what is seen. As such, adding an ocean surface on 1e for a cloudless Trappist-1 system induces a difference in the degree of polarization of the system reaching up to $P_s = 3.83 \times 10^{-8}$, occurring at about 4 days, during which the reflected flux plot of 1e is undergoing a maximum due to the glint, peaking at this time.

**Trappist-1 planets with clouds**

For this scenario, we assume the same conditions as the previous one, with the addition of a full cloud deck on each Trappist-1 planet. The data for this is found in Tables 4.5 and 4.6, and the figures are plotted in Fig. 4.26.

| **Parameter** | **Value** |
|---|---|
| Wavelength | $\lambda = 1.15\ \mu m$ |
| Surface pressure | $p_s = 1\ atm$ |
| Top of atmosphere pressure | $p_{top} = 0\ atm$ |
| Ocean | 1e |
| Clouds | Yes |
| **Variable Parameters** | |
| Surface albedo | $A_s$ |
| Depolarization factor | $\delta$ |
| Molecular mass | $M_u$ |
| Air refractive index | $n$ |
| Gravitational acceleration | $g$ |
| Radius | $R$ |
| Semi-major axis | $a$ |

Table 4.6: Similar to Table 4.5, but with clouds. The “variables parameters” values are found in Table 2.1. The atmospheres of the planets (from 1b to 1h) are composed of the following gases: $H_2O$, $O_2$, $H_2O$, $H_2O$, $N_2$, $N_2$, and $N_2$.

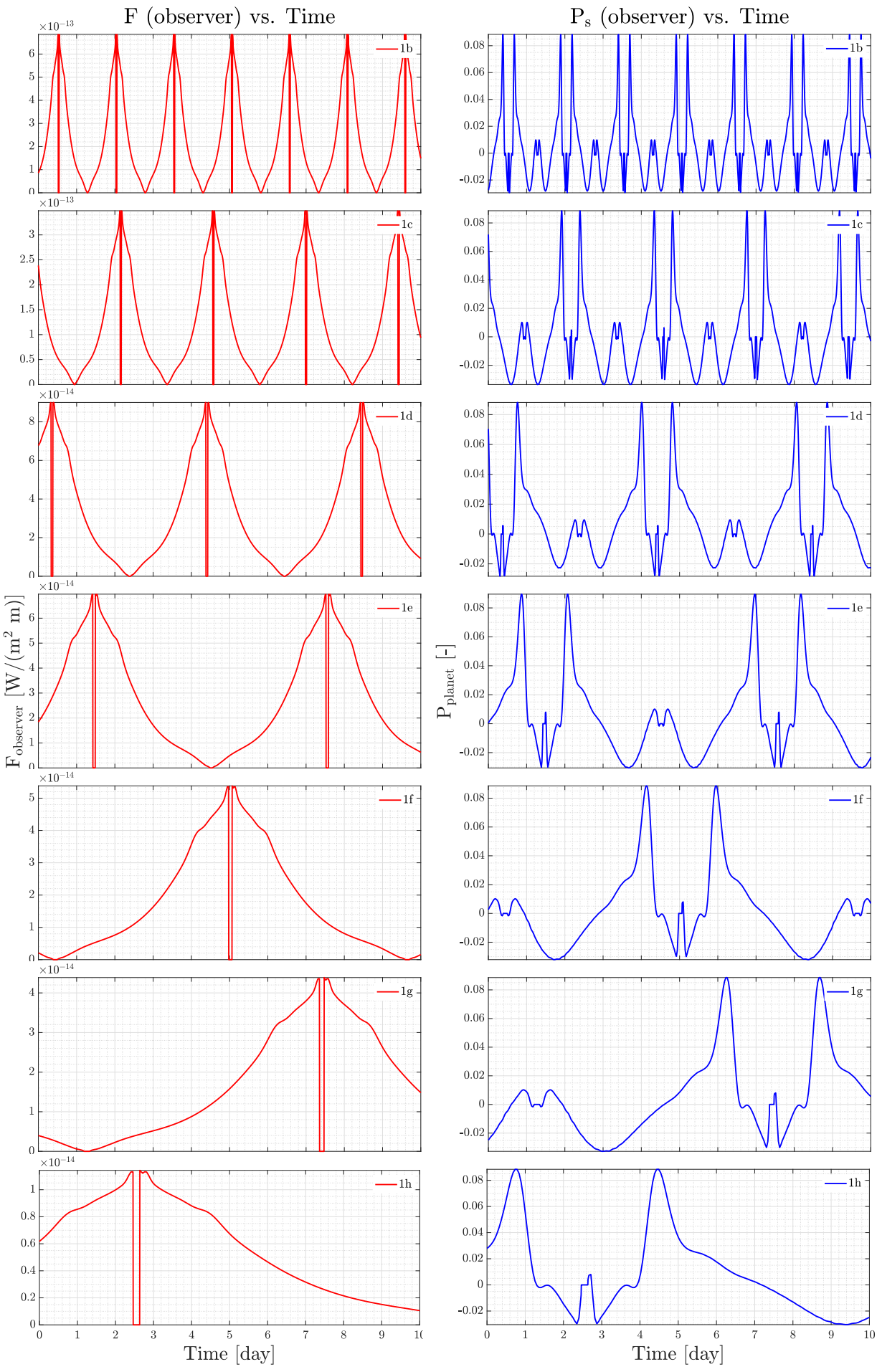


Figure 4.26: Similar to Fig. 4.23, but all planets are fully covered by a cloud deck.

Fig. 4.26, shows that the $F$ curves have increased drastically due to the clouds (see Fig. 4.11 to see how much does $F$ change when adding a cloud layer), with noticeable bumps due to the rainbow, i.e., at about 2 days for 1e.

The $P_s$ curves also look different, with the rainbow peaks generally reaching higher values of $P_s$ than for the clear case, though the atmospheric composition and gravitational acceleration of clear cases plays a role, and should be considered.

The features in $F$ and $P_S$ caused by having an ocean are now subdued in the presence of clouds (see Fig. 4.14); though different atmospheric compositions will have different $P_s$ curves at certain times (see Fig. 4.11 and its discussion), due to the scattering of atmospheric gas above the cloud layer.

Next, we plot the degree of polarization of the whole system in Fig. 4.27, with all Trappist-1 planets being fully cloudy. The figure shows plots with (bottom) and without (top) including stellar flux, with (right) and without (left) considering the eclipse, as a function of time.

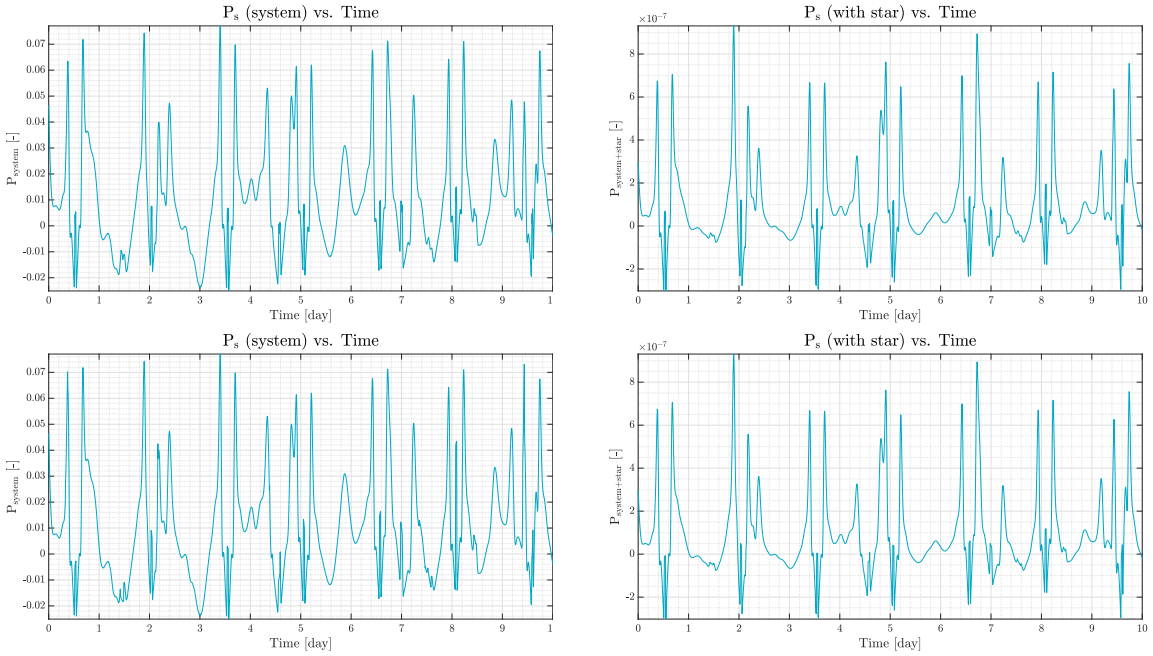


Figure 4.27: Similar to 4.24, but all the planets are fully cloudy.

From Fig. 4.27, the curves look much spikier in the presence of clouds, compared to the clear cases. These features are due to the rainbow peak, as well as the steep changes in polarization direction. This makes the eclipse-induced features much harder to spot, some of which can be seen, i.e., the spikes at 0.4 days ($P_s \approx 0.070$) at 9.4 days ($P_s \approx 0.074$). This is because the eclipse occurs when $F$ is supposed to be at a maximum, for which the phase angle is near 0°, around which the $P_s$ curve undergoes many peaks and sign changes. Moreover, the $P_s$ curves being symmetric (due to orbit symmetry) doubles these features over a very short time period. Fig. 4.8 shows how concentrated these features are.

Similarly to what was said previously, adding a star into the signal dilutes some features, for example the peak at 5.8 days.

Having planets with clouds increases the degree of polarization of the system as seen by the observer, where in this case it $8.5 \times 10^{-7}$. For comparison, for the case of Trappist-1 planets having no clouds, and 1e being an ocean, $P_s = 8.3 \times 10^{-8}$ (Fig. 4.24), while for the case of Trappist-1 planets having black surfaces with Earth-like compositions, $P_s = 1.2 \times 10^{-8}$ (Fig. 4.20).

Next, we would like to see the difference in signal due to having an ocean for this scenario (i.e., all Trappist-1 planets with 1e being an ocean planet, and all planets are fully cloudy, with an atmosphere).

To do this, we make a plot overlaying two curves, one for the Trappist-1 system with 1e being an ocean, while the other is the same but 1e has its ocean substituted by a black surface (while its atmosphere remains the same). This is shown in Fig. 4.28.

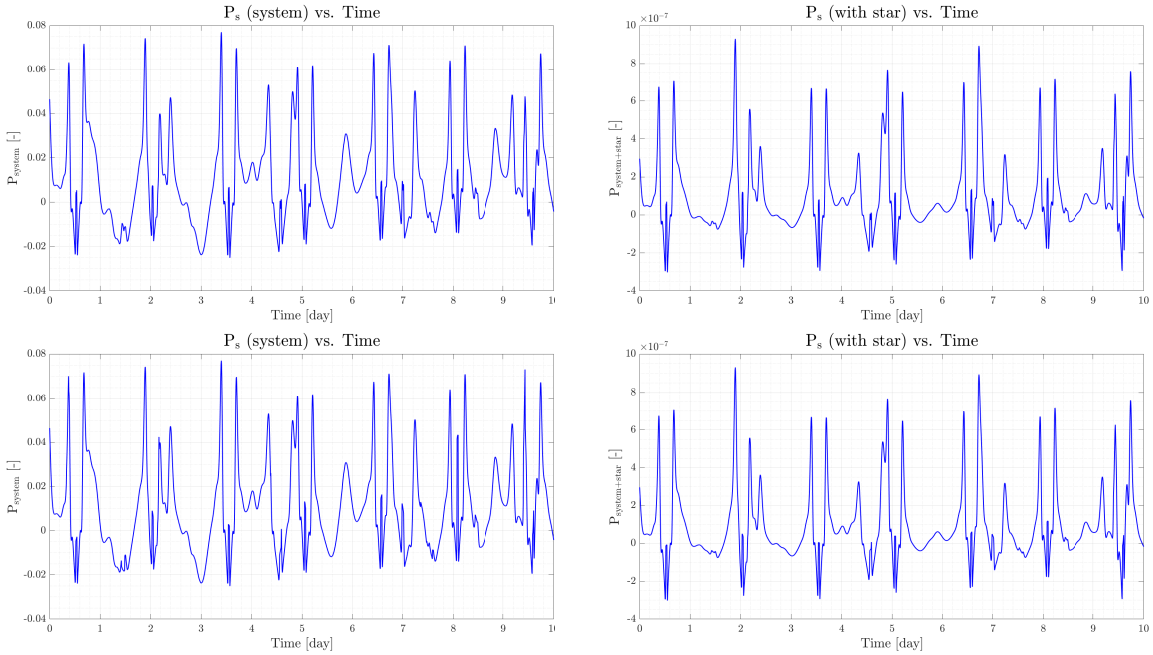


Figure 4.28: Similar to Fig. 4.22, this figure shows the degree of polarization of the Trappist-1 system for all cloudy planets and 1e having an ocean (blue line), and for the same system but for 1e having no ocean (red line). The plots are placed with (top) and without (bottom) eclipses, for the system with (right) and without (left) including the star.

We notice that Fig. 4.28 is similar to Fig. 4.25 with the addition of a cloud deck above the surface. In this figure, the difference between the two curves is the presence of an ocean on 1e (the red line is for 1e modeled as a black surface with an atmosphere and clouds, and the blue line is for 1e modeled as an ocean planet with the same atmosphere and clouds). We see that the curves are exactly the same, due to clouds completely covering the surface, hence we cannot notice any difference made by the presence of an ocean. As such, adding an ocean surface on 1e for a fully cloudy Trappist-1 system induces no difference in the degree of polarization of the system, or $P_s = 0.0$, and so the presence of an ocean cannot be observed.

It is interesting to note that when the planets are spatially unresolved from their star, Seager et al. predict that the degree of polarization is expected to be in the order of $\sim 10^{-6}$ [58]. We obtain this value when we have a full cloud cover, as seen in Fig. 4.28, though when there are no clouds in the system, this value drops to about $10^{-7}$, see Fig. 4.25.

### Trappist-1 planets with patchy clouds

Next, we would like to see the change in the signal curves for intermediate cloud cover values, so here we consider a patchy partial cover. Here, we assume the same conditions as the previous scenario, where we consider the case of having seven planets with non-black surfaces and atmosphere compositions corresponding to those of the Trappist-1 planets (in terms of depolarization factor $\delta_{air}$, refractive index $n_{air}$, surface pressure $p_s$, top-of-atmosphere pressure $p_{top}$, and atmospheric gas molecular mass $M_u$). Similar to the previous scenario, the planets vary in gravitational acceleration, radius, and semi-major axis, which are the exact values of the respective Trappist-1 planets.

For this scenario, the system consists of Trappist-1 planets with a variable cloud cover (25%, 50%, 75%), with 1e having an ocean. The data for the upcoming several figures are found in Tables 4.7 and 2.2. The properties of these planets are summarized in Table 4.7, and the curves are plotted in Fig. 4.29. The planetary eclipses have been included.

| **Parameter** | **Value** |
|---|---|
| Wavelength | $\lambda = 1.15\ \mu m$ |
| Surface pressure | $p_s = 1\ atm$ |
| Top of atmosphere pressure | $p_{top} = 0\ atm$ |
| Ocean | 1e |
| Clouds | 25%, 50%, 75% |
| **Variable Parameters** | |
| Surface albedo | $A_s$ |
| Depolarization factor | $\delta$ |
| Molecular mass | $M_u$ |
| Air refractive index | $n$ |
| Gravitational acceleration | $g$ |
| Radius | $R$ |
| Semi-major axis | $a$ |

Table 4.7: Similar to Table 4.5, but with clouds. The “variables parameters” values are found in Table 2.1. The atmospheres of the planets (from 1b to 1h) are composed of the following gases: $H_2O$, $O_2$, $H_2O$, $H_2O$, $N_2$, $N_2$, and $N_2$.

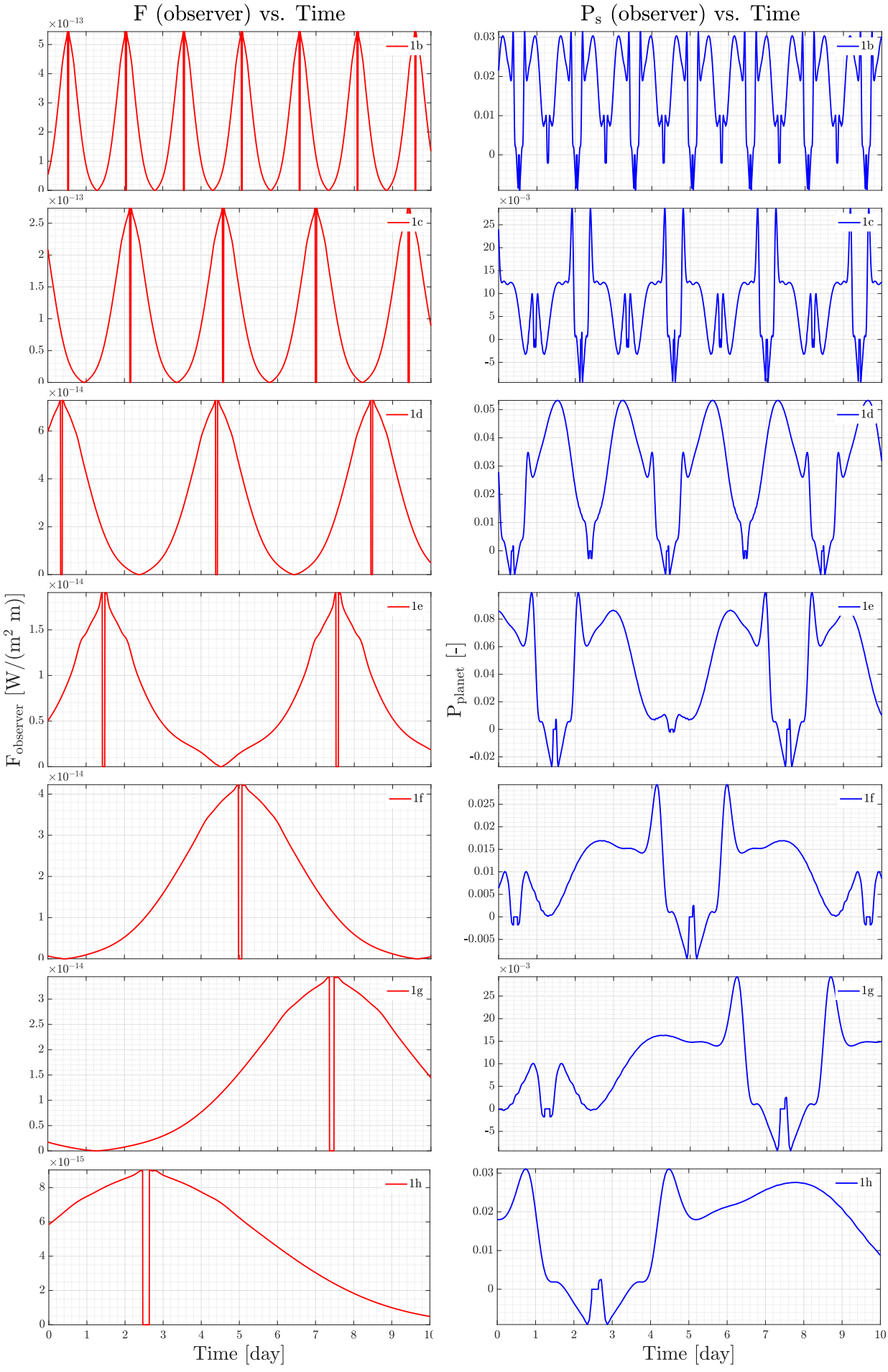


Figure 4.29: Similar to Fig. 4.26, but all planets have a 25% patchy cloud cover.

Fig. 4.29 shows that the $F$ and $P_s$ curves have decreased when compared to a full cloud coverage (see Fig. 4.26), where a lower cloud cover causes a lower reflected flux and degree of polarization (see the discussion of Figs. 4.10 and 4.11), when compared to a full coverage.

We also notice that for a lowering in cloud cover, the role of the atmospheric gas increases, producing a round shape right after the rainbow peak, at about 2.2 days for 1e for example. This shape is not present in the fully cloudy case as atmospheric gas scatters very little compared to clouds. This phenomenon weakens for an increase in cloud cover (causing more scattering, so the shape 'deflates'), and increases for a lower mass of atmospheric gas and/or gravitational acceleration. As such, this feature is not equally present in the $P_s$ plots, given the different characteristics of different planets. It is most noticeable in 1d, even exceeding the rainbow peak. The reason for this is that 1d has a combination of a relatively light atmospheric gas, and has the lowest gravitational acceleration in the Trappist-1 system.

For 1e, the signal curves shrink greatly when we add clouds, even for a 25% coverage. For instance, for no clouds, $F$ and $P_s$ reach values of $6 \times 10^{-15}$ and 0.9 respectively, while for a 25% cloud cover, they reach values of $2 \times 10^{-14}$ and 0.09 respectively. It should be noted that with a 25% cloud cover, the effect of the ocean is still noticeable, as the $P_s$ of 1e reaches values that are about 1.5-3 times larger than other Trappist-1 planets.

Next, we plot the degree of polarization of the whole system in Fig. 4.30, with all Trappist-1 planets having a 25% cloud cover. The figure shows plots with (bottom) and without (top) including stellar flux, with (right) and without (left) considering the eclipse, as a function of time.

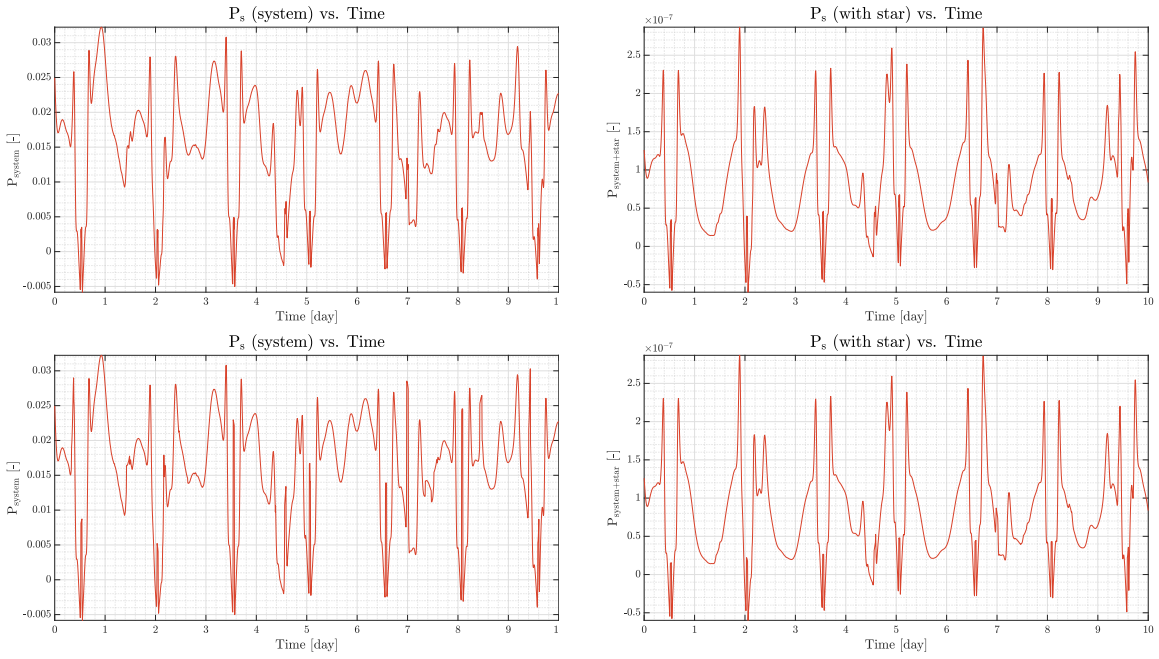


Figure 4.30: Similar to 4.24, but all the planets have a cloud cover of 25%.

From Fig. 4.30, we see that all $P_s$ curves shrunk compared to the 100% cloudy case (see 4.28), peaking at about $P_s = 3 \times 10^{-7}$, compared to $8 \times 10^{-7}$ for a full cloud cover.

Fig. 4.31 below illustrates the difference in signal due to having an ocean for this scenario, where the planets are modeled as Trappist-1 planets, 1e being an ocean planet and each having a 25% patchy cloud cover, along with an atmosphere. Similar to previous cases, we illustrate this difference by overlaying the curves, one of which has the whole system with 1e as an ocean planet, and the other has this ocean replaced by a black surface.

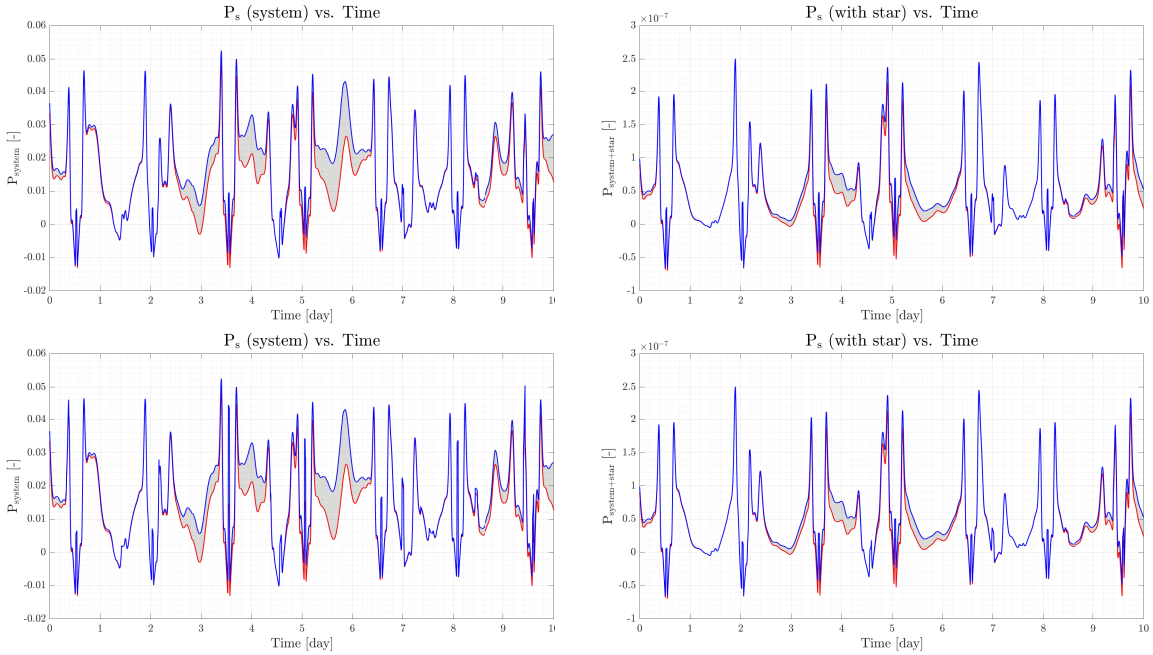


Figure 4.31: Similar to Fig. 4.28, with all planets having a cloud cover of 25%. This figure shows the degree of polarization of the Trappist-1 system for all cloudy planets and 1e having an ocean (blue line), and for the same system but for 1e having no ocean (red line).

The presence of an ocean on 1e, when compared to a black surface planet, induces a difference in the degree of polarization of the system reaching up to $P_s = 2.87 \times 10^{-8}$, occurring at about 4 days.

Fig. 4.31 shows the system $P_s$ curves for a cloud coverage of 25% for all planets, with atmospheres. It is similar to Fig. 4.25, but with the addition of a patchy cloud deck above the surface. The curves in Fig. 4.31 differ as one has an ocean on 1e, while the other does not (the red line is for the system with 1e modeled as a black surface with an atmosphere and clouds, and the blue line is for the system with 1e modeled as an ocean planet with the same atmosphere and clouds). Comparing to Fig. 4.25, we concur that an increase in cloud cover causes the difference in degree of polarization caused by the presence of an ocean to decrease, reaching about $3 \times 10^{-8}$ at 4 days in this case. This is expected because as the cloud cover increases, a larger portion of the surface is covered, concealing features like oceans and their signal. Reminder that for a 100% cloud cover, there were no observable differences between the degree of polarization curves, while for a 0% cloud cover, the difference between the degree of polarization curves were largely observable, but the $P_s$ curves had lower values than the 100% cover case. When the cloud cover increases, the reflected flux increases, while the degree of polarization increases at some phase angles and decreases at others, though the rainbow peak gets consistently larger, until reaching a coverage of 100% (see Fig. 4.11). Since for our analysis the Trappist-1 planets do not have light atmospheric gases like $H_2$, the largest feature in the $P_s$ plot is the rainbow peak; if the atmosphere were made up of a lighter gas like $H_2$, the $P_s$ would be dominated by its peak, rather than the rainbow peak (see Fig. 4.11 for the difference in peak size). As such, since the $P_s$ curve is dominated by the rainbow peak, which increases with cloud cover, then as the latter increases, we expect a larger $P_s$. However, the difference between the curves decreases with increasing cloud cover, so at 100% cover, we will have the largest $P_s$ plot, but there will be no difference between the curves, so we cannot view the ocean. Therefore, we need to take intermediate cloud coverage values as we have done here (like 25%, 50%, and 75%) to estimate when should we expect the clearest difference due to the ocean.

Next is Fig. 4.32, which is identical to the previous case, except for having a cloud cover of 50%. The data for it is found in Table 4.7

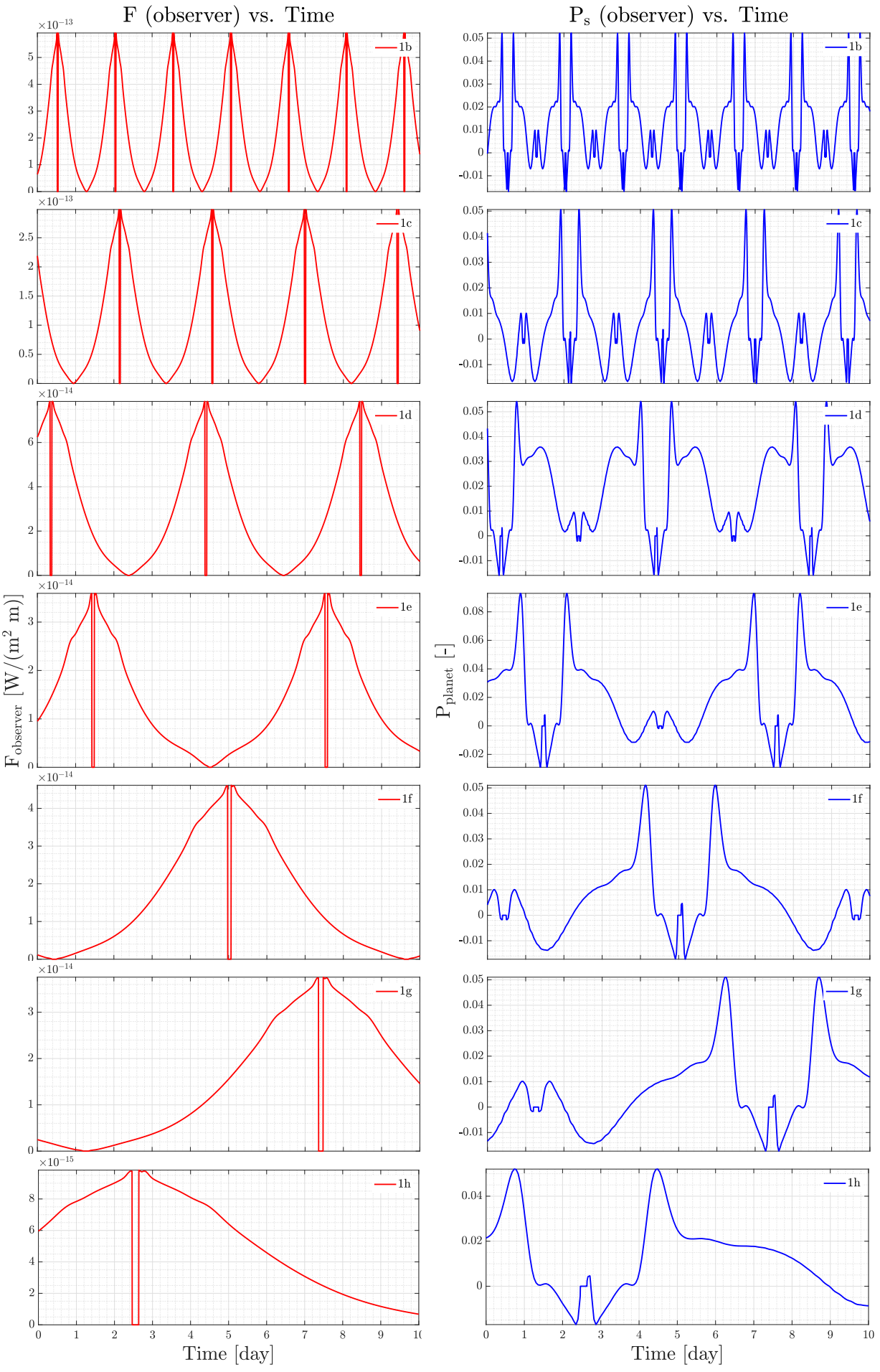


Figure 4.32: Similar to Fig. 4.26, but all planets have a 50% patchy cloud cover.

Fig. 4.32 continues the trend, where an increase in cloud cover increases both $F$ and $P_s$. for the planets, 1d in particular, The increase in cloud cover diminishes the role of the gas, decreasing the $P_s$ right after the rainbow peak (see Fig. 4.13). The highest $P_s$ point for each planet in this plot is the peak due to the rainbow, and the same goes for Fig. 4.29, though for 1d, the curve experienced a considerable increase in $P_s$ after the rainbow (at about 1-2.2 days), which is due to the planet's low atmospheric mass and gravitational acceleration.

The degree of polarization of the whole system is plotted in Fig. 4.33, with all Trappist-1 planets having a 50% cloud cover. The figure shows plots with (bottom) and without (top) including stellar flux, with (right) and without (left) considering the eclipse, as a function of time.

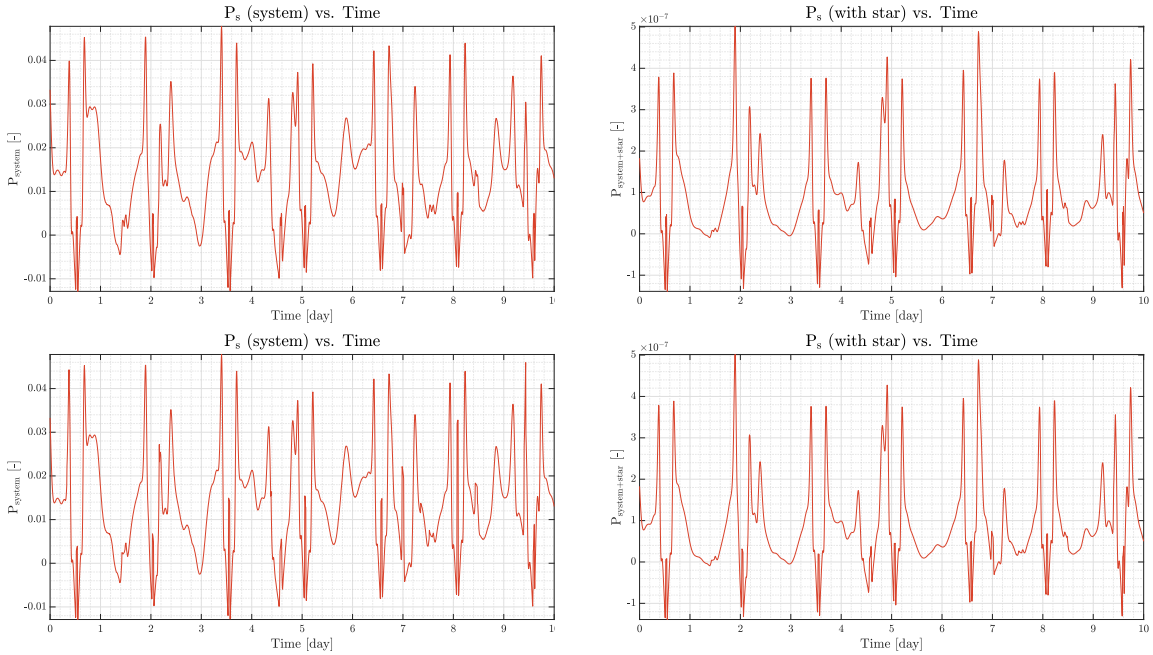


Figure 4.33: Similar to 4.24, but all the planets have a cloud cover of 50%.

From Fig. 4.33, we see that all $P_s$ curves expanded compared to the 25% cloud cover case (see 4.30), peaking at about $P_s = 5 \times 10^{-7}$, while the latter case peaked at about $P_s = 2.8 \times 10^{-7}$.

Fig. 4.34 below illustrates the difference in signal due to having an ocean for a 50% cloud cover scenario.

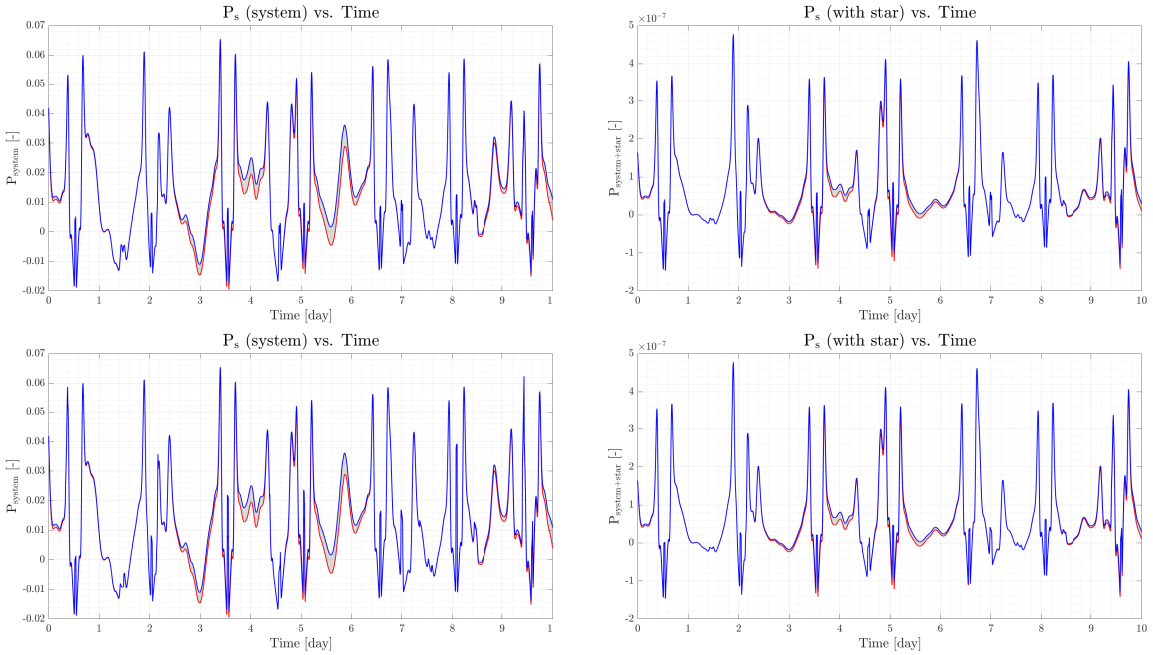


Figure 4.34: Similar to Fig. 4.22, with all planets having a cloud cover of 50%.

In Fig. 4.34, the curves differ only by the presence of an ocean on 1e (the red line is for 1e modeled as a black surface with an atmosphere, and the blue line is for 1e modeled as an ocean planet with the same atmosphere). Similar to what was said for Fig. 4.30, the degree of polarization of the whole system increase with cloud cover, but the difference between the two cases decreases, as more of the planet is covered by clouds. The presence of an ocean on 1e, when compared to a black surface planet, induces a difference in the degree of polarization of the system reaching up to $P_s = 1.92 \times 10^{-8}$, occurring at about 4 days.

Next is Fig. 4.35, which is identical to the previous case, except for having a cloud cover of 75%. The data for it is found in Table 4.7

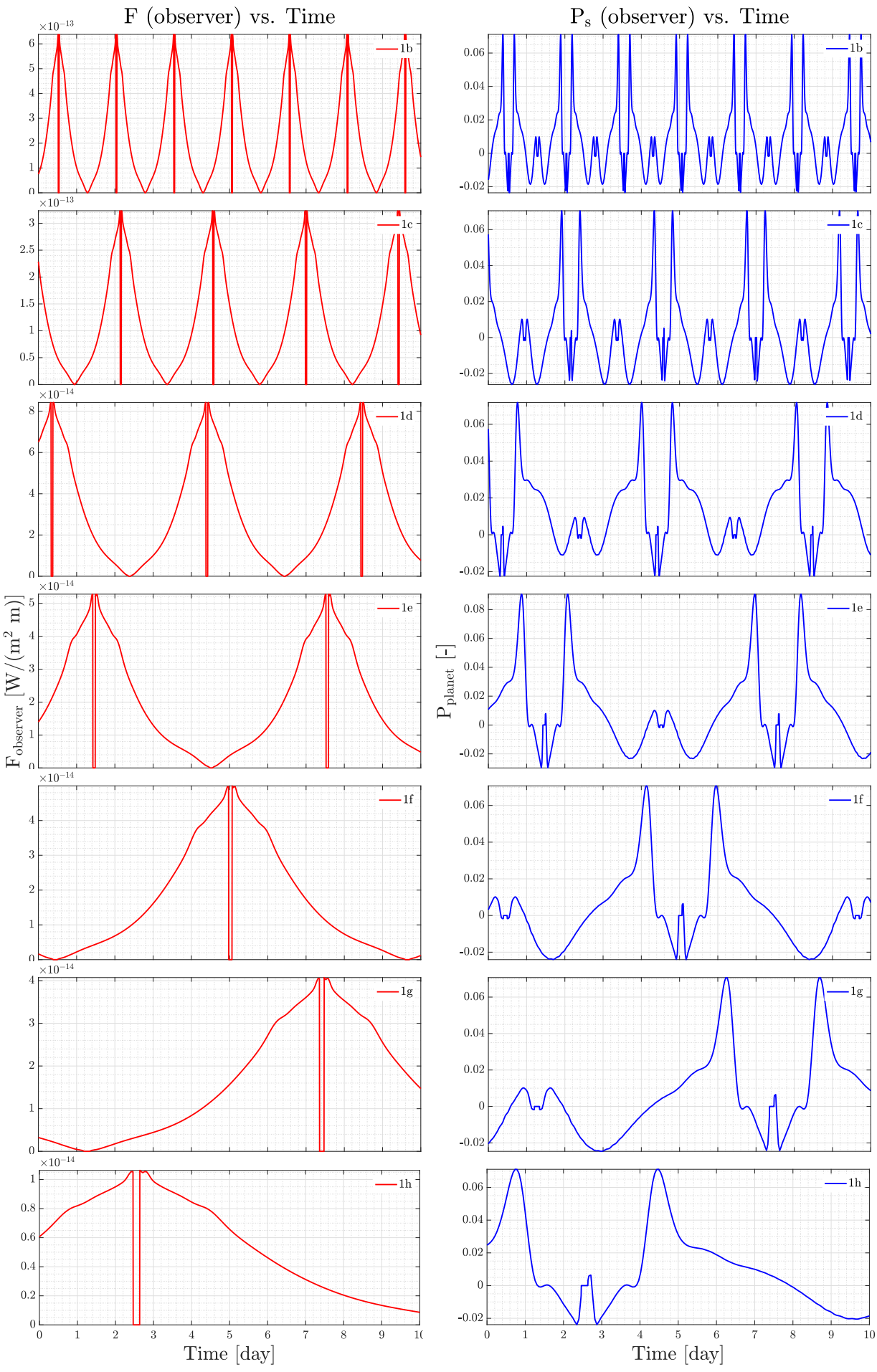


Figure 4.35: Similar to Fig. 4.26, but all planets have a 75% patchy cloud cover.

Fig. 4.35 shows the same trend as the previous cases; both $F$ and $P_s$ increase with cloud cover, diminishing the role of the gas.

The degree of polarization of the whole system is plotted in Fig. 4.36, with all Trappist-1 planets having a 75% cloud cover. The figure shows plots with (bottom) and without (top) including stellar flux, with (right) and without (left) considering the eclipse, as a function of time.

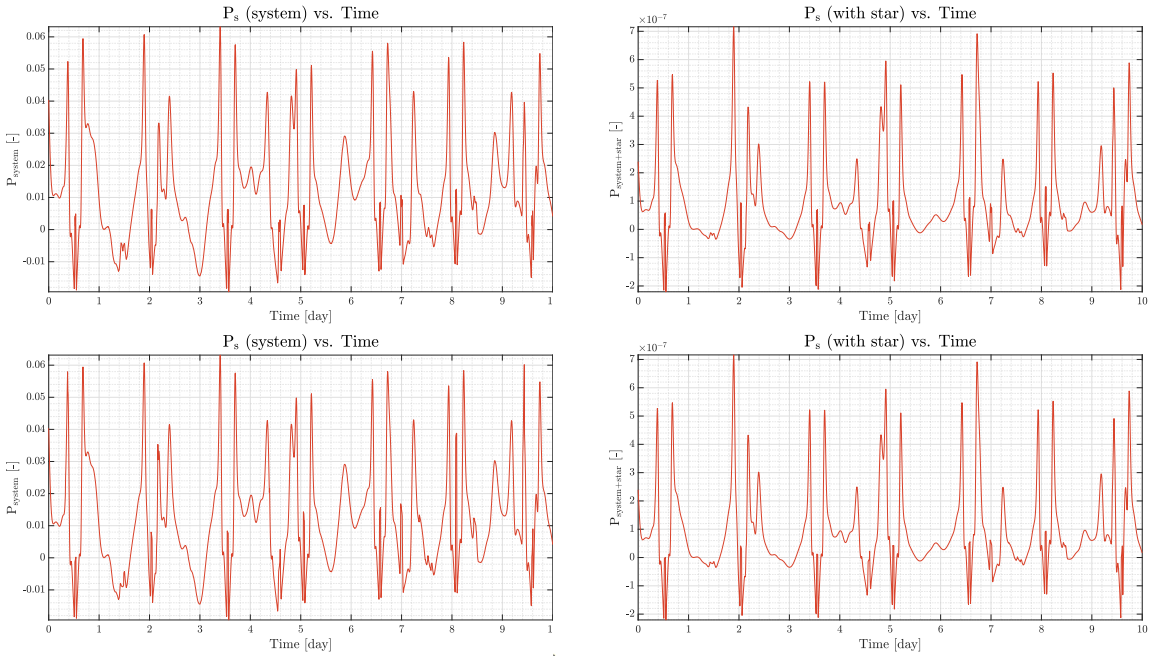


Figure 4.36: Similar to 4.24, but all the planets have a cloud cover of 75%.

Similar to the case for a 50% cloud cover, an increase in cloud cover leads to larger $P_s$ curves Fig. 4.36, we see that all $P_s$ curves expanded, peaking at about $P_s = 7.2 \times 10^{-7}$.

Fig. 4.37 below illustrates the difference in signal due to having an ocean for a 75% cloud cover scenario.

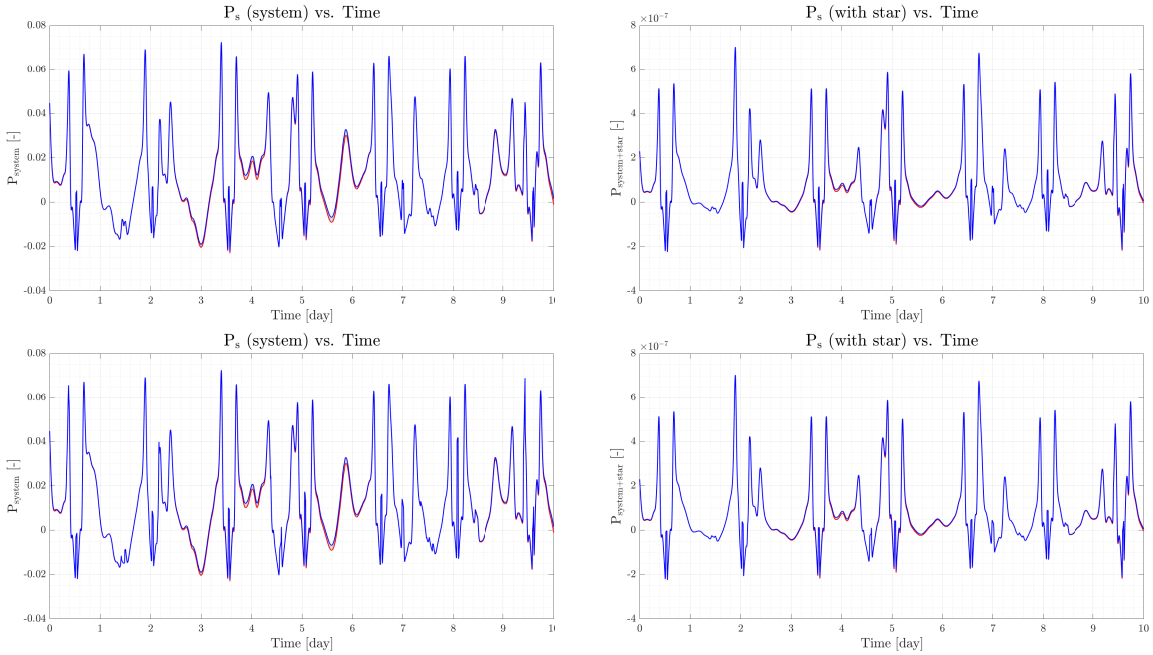


Figure 4.37: Similar to Fig. 4.22, with all planets having a cloud cover of 75%.

The presence of an ocean on 1e, when compared to a black surface planet, induces a difference in the degree of polarization of the system reaching up to $P_s = 9.58 \times 10^{-9}$, occurring at about 4 days.

### 4.3.1. Other works

Here, we refer to Kopparla et al., who attempted to observe the ocean on 1e, and modelled the disk-integrated phase curves and polarization signals for the Trappist-1 planets [33].

The $F$ and $P$ plots for 1e of Kopparla et al. are shown below. For this, they used an ocean-covered surface with wind speed of $v_{wind} = 10\ m/s$, clouds with radius $r = 2\ \mu m$ and variance $v = 0.1\ \mu m$. Note that they use a different definition of the phase angle, which starts at mid-transit and has a value of $0 - 1$.

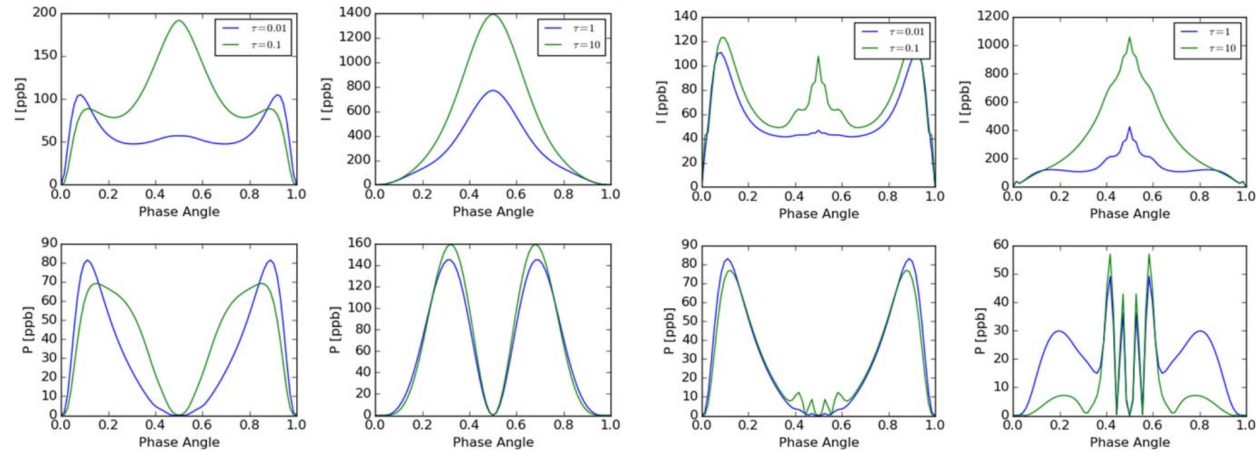


Figure 4.38: The Trappist-1 system: planet sizes and orbits, by Kopparla et al. [33]. Figure a) Reflected starlight intensity and degree of polarization curves, for 1e for a thin (left) and thick (right) atmospheres over an ocean-like surface with a glint. The parameters are expressed in parts per billion. Figure b) Similar to Fig. a) but with the addition of cloud particles of radius 2 $\mu m$.

The general shape of the $F$ and $P$ curves is reminiscent of Figs. 4.6 and 4.14, the former for Fig. 4.38 a) for a thin atmosphere, and the latter for Fig. 4.38 b). Note that they use the absolute value of $P_s$, so their plots will be positive, concealing the change in direction of polarization (though the direction change can be inferred whenever the curves touch the x-axis). We notice that they have considered that multiple scattering at large phase angle values drops the $P$ plot to negative values.

From Fig. 4.38, Koparla et al. concluded that polarization signals are strongest for optically thin ($\tau \sim 0.1$) atmospheres over widespread oceans (which we also concluded in Fig. 4.14).

Next is the total system, for which all planets but 1e are dry and spatially homogeneous, have a surface albedo of $0.2$, have atmospheric optical thickness $\tau = 0.1$, and a weakly absorbing atmosphere with single-scattering albedo of 0.9999.

We attempted to do the same plots to accurately compare our results. To reduce the differences between our methods, we have used their convention of scaling planet signals and axes. We assume their unstated parameters such as gravitational acceleration are the correct ones, according to Delrez et al. [9], and their unstated variables such as surface pressure, are similar to the values we used. We use a wavelength of $\lambda = 1.15\ \mu m$, and used our convention of the phase angle.

Our used parameters are similar to those in Table 4.5, where 1e is an ocean planet with a wind speed of $7 m/s$. The atmospheres of the planets (from 1b to 1h) are composed of the following gases: $H_2O$, $O_2$, $H_2O$, $H_2O$, $N_2$, $N_2$, and $N_2$.

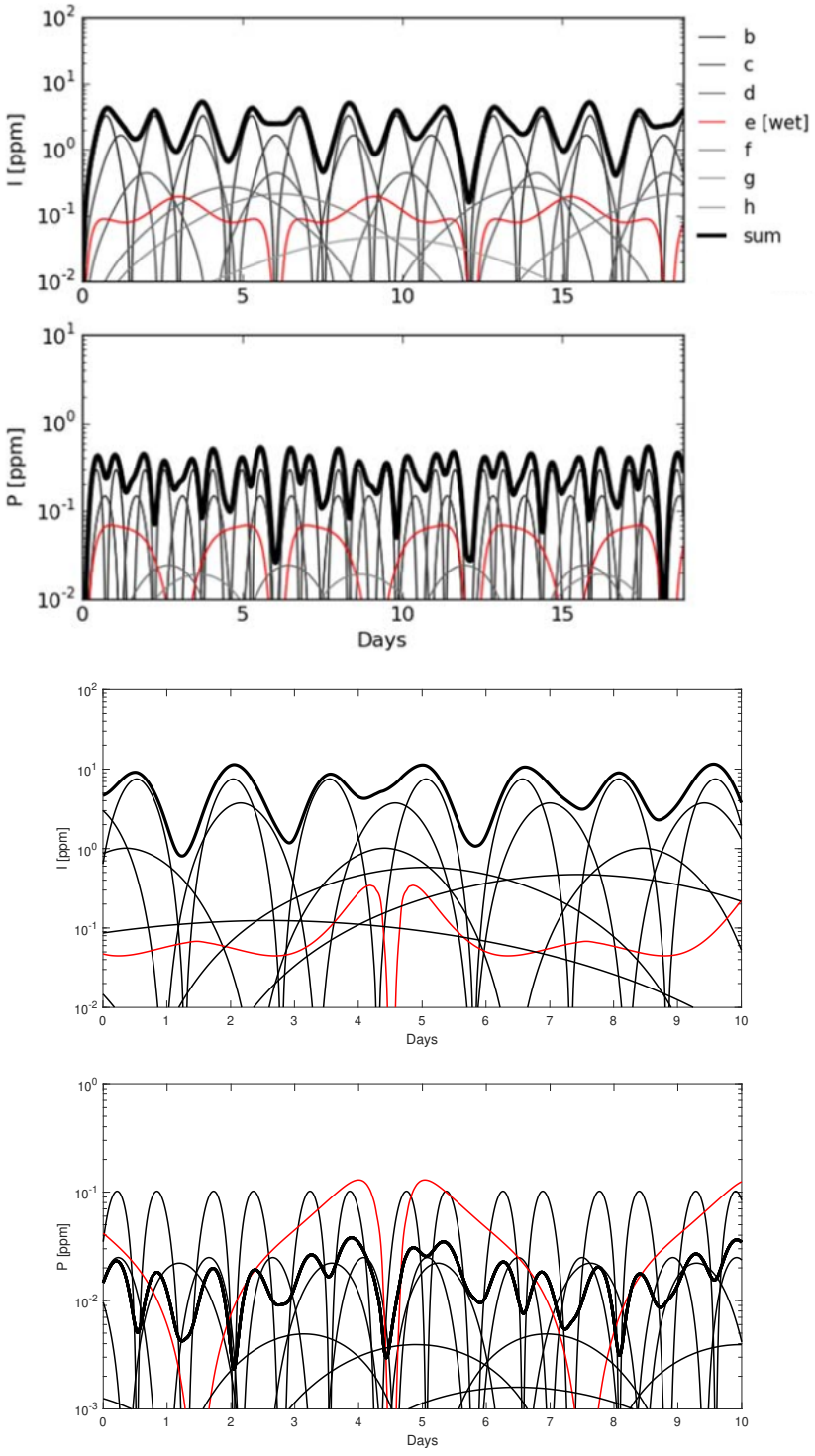


Figure 4.39: Polarization signals of the Trappist-1 system. Top two plots: $F$ and $P$ of the entire system, made by Kopparla et al., for which all planets are fully dry, except for the ocean planet 1e. There are no clouds for the system. Bottom two plots: $F$ and $P$ of the entire system, using our code and parameters. There are no clouds in the system, and 1e has a global ocean. For all figures, the red line indicates 1e, and the thick black line indicates the entire system. We used $\lambda = 1.15\ \mu m$.

At first glance, we see that our values for system reflected flux are somewhat similar. One apparent difference is the choice of wind speed for 1e, where a lower value yields a lower $F$ but a higher glint peak, and a higher $P$ value (see Fig. 4.6). In our $P$ plot in Fig. 4.39, the ocean curve is the highest, which we attribute to two factors, the first being our choice of wind speed (if we chose a larger value, the

$P$ would decrease), and the second being the optical thickness of the atmosphere of 1e, which is much thinner than that of Kopparla et al., where they assumed an optical thickness of 0.1 for every planet, while ours depends on our input (having values of 0.0007, 0.0008, 0.0010, 0.0011, 0.0012, 0.0013, and 0.0015, from 1b to 1h, using Eq. 3.16).

In addition, Kopparla et al. have not considered the orbit ephemerides, as their curves begin at the (0, 0) coordinate point for every planet.

One issue we have with the $P$ plot of the entire system is that Kopparla et al. plotted the individual degree of polarization of every planet and added the stellar signal to it, with the justification that since the planets are so tight to their star, the planets' flux will be indistinguishable from the stellar flux. So, when they are computing the $P$ of the entire system, they are including the stellar flux seven times, once for each planet, which explains why their values for $P$ are so low. The observer on Earth receives the combined signal of the system, comprising of each planet's signal plus the star's, so the stellar flux should be added to the whole system once rather than to each planet, resulting in a slightly higher system $P$. Another issue we have is that they summed individual degree of polarization signals, rather than dividing the sum of $F$ and $Q$ signals ($P = \sum Q / \sum F$), obtaining a net $P$ curve greater than its component curves at all times. While the shape of our $P$ curve looks slightly similar to their, we are doubtful of obtaining the system's total degree of polarization by summing adding individual $P$ signals.

Aside from that, our figures are similar to their in terms of shape and values, though some of their parameters were not defined.

# 5

# Conclusions

Trappist-1 is a planetary system consisting of an M-dwarf star located at about 39 light years away from Earth, and has seven known planets orbiting it very tightly. This system is special for many reasons; first, given Trappist-1's low instellation levels, combined with its planets' close proximity to it, makes it possible for these planets to receive instellation levels similar to Earth's, which could open many doors regarding the planets' habitability [33]. Second, its planets orbit their parent star in such tight orbits that we cannot observe the planets' individual signals separately, and those cannot be resolved from the star. Finally, one of its planets, 1e, is highly believed to contain surface water, a requirement for life.

These planets have been discovered by transit observations and as such, their surface and atmospheric properties are not very well known. Using little information such as the star's properties and the sizes, masses and orbital distances of the planets, many models have been used to predict the atmosphere and surface of each Trappist-1 planet (such as the ones by Batalha et al. [5], Lincowski et al. [35], Grimm et al. [15] and many others). The aim of this Master's Thesis research project was to numerically simulate the possible polarimetric signals of the Trappist-1 planets, using atmosphere and surface predictions from those other models.

For exoplanets, polarimetry could allow distinguishing faint planetary signals from brighter stellar light. Measuring a polarized signal would confirm an object's nature [53]. For instance, observing polarized light allows up to a tenfold increase in star-planet contrast, compared to photometric observations alone [33]. Using present-day technology, we cannot reach contrast levels high enough at angular separations of the Trappist-1 planets from their star; therefore, observations of reflected light curves cannot spatially separate light from the Trappist-1 planets, so in reality, collected data will consist of the sum of reflected light from all planets [33].

First, we took a look at various atmospheric and surface possibilities of the Trappist-1 planets and assessed which were more plausible. Then, we computed the total flux and polarization signals of starlight that is reflected by each planet. Since the Trappist-1 system is very far away from Earth and the planets are so close to their star, their individual signals cannot be viewed separately, so the flux and polarization signals that would be intercepted by the observer consist of stellar light and stellar light reflected off the planets (we neglect the planets' thermal signals). The latter depends on the planets' position with respect to the star over time. The results of this work serve as a rough guide to the expected signals of Trappist-1, which can be used for designing instruments and telescopes for such direct observations and for setting up observing programs.

We have performed our simulations at a wavelength of $\lambda = 1.15\ \mu m$, at which the Trappist-1 star emits the most. For this, we varied the following planet properties: surface albedo (with and without clouds), atmospheric gas mass, gravitational acceleration, surface pressure, wind speed above an ocean surface, ocean composition, cloud-top altitude, cloud cover percentage, and atmospheric composition. We have tailored these parameters for each Trappist-1 planet to get these planets' individual $F$ and $P_s$ curves, and we have computed the expected signal of the entire system, with and without including

the stellar flux. We observed that the degree of polarization that can be observed for an exoplanetary system depends on the planets' intrinsic degree of polarization, as well as on the stellar flux in the background of the planetary signals, in agreement with Rossi et al. [53].

For each planet, having a lighter atmospheric composition, such as $H_2$, causes an increase in both reflected flux and degree of polarization, so for the whole system, the degree of polarization would be higher. Given our assumed atmospheric composition, having clouds on planets increases the degree of polarization of the entire system by about an order of magnitude. The presence of thick clouds, such as cumulus clouds, renders the role of the atmospheric gas almost negligible. Given its position in the system's habitable zone, 1e is highly believed to have a surface ocean. For a system of black surface planets, adding an ocean for one planet increases the entire system degree of polarization by a factor of 5.

A planet's orbital distance plays a large role as well, where the furthest planet from the star, 1h, is 5.36 times further than the closest planet to the star, 1b. This difference in distance results in a 30-fold increase in the reflected flux of 1b compared to 1h. The planetary radius acts in a similar way, though its effect is much less because the difference in Trappist-1 planets radii is much smaller; 1b is 1.45 times larger in radius than the smallest planet, 1h, getting a 2-fold increase in reflected flux compared to the latter. Hence, based only on size and semi-major axis, the reflected flux of 1b is 60 times larger than that of 1h (see Table 4.4). However, since we cannot discern the signal of individual planets, then the previous should be expressed in terms of contribution to the system's degree of polarization, where closer planets would contribute the most to the total system signal, while outer planets like 1h barely make a difference.

In addition, we have computed the signal of the Trappist-1 system numerous times, varying the cloud cover between runs (from 0% to 100% in increments of 25%), to assess the the ability to detect an ocean on 1e. The ocean is central to our work as water is a requirement for life, so having an abundance of water on a planet satisfies one criterion to find life there, making the system much more interesting with respect to habitability prospects. We notice that as the cloud cover increases, the reflected flux and degree of polarization increase as well, but the difference in signal due to the presence of an ocean on 1e decreases. This is due to the clouds concealing the surface and reducing the role of scattering by the atmospheric gas, where polarization from sources like atmospheric scattering and cloud variability poses challenges to the detection of polarization signals [33]. As such, for the properties we used, the presence of an ocean is best observed when the cloud cover is 0%, constituting a difference in degree of polarization of $P_s = 3.83 \times 10^{-8}$, which is not detectable by current technology.

Given how dim Trappist-1 is, for the best case scenario of all planets being cloudy (which is unrealistic), the system's degree of polarization is roughly $10^{-6}$. Modern polarimeters can reach accuracies in the order of $10^{-5} - 10^{-6}$ [27, 55], though not in the waveband of Trappist-1. The James Webb Space Telescope (JWST), which will not observe the reflected light of the Trappist-1 system, is slated to directly observe it sometime in its initial phase. This would give us a much clearer view of the planets and their surface and atmospheric properties. On the other hand, there are proposals for several large space- and ground-based telescopes with coronagraphs and polarimeters, which are sensitive to very low planet-star contrasts [33]. We hope that in the near future, new instruments with increased capabilities will enable us to better view such systems and determine the physical properties of their planets.

# 6

# Future work

This chapter addresses possible future studies related to this work.

Investigating other exoplanetary systems would be interesting. The Trappist-1 system is special as it is a tight system, whose planets cannot be observed separately; this also applies to the TOI700 and HD209458 systems. The red dwarf TOI700 system is particularly intriguing as it is the *"brightest known host of a transiting habitable-zone Earth-sized planet discovered to date"* [50]. Its planet TOI700 1d, likely a rocky planet with a similar radius and mass to Earth's, is a good contender for being a habitable world [1, 50]. Another interesting system to look into is HD209458, whose planet HD209458b, or Osiris, contains water vapor in its atmosphere and potentially clouds [44].

Another suggestion would be the study of cloud formation on Earth-like exoplanets, which was an initial version of this project. For this, cloud microphysics and circulation models would be used, such as *Speedy* (Simplified Parameterizations, primitivE-Equation DYnamics). The focus of the study was later changed as the current *Speedy* version proved to be unfeasible in terms of code functionality and the knowledge level needed to operate its associated programs, such as the grid display of results on GrADS. Currently, a user-friendly version of *Speedy* that can be adapted for planets other than Earth.

For prospective students, ideas for thesis projects in the same vein as this work include:

- Investigating the signals of planets with clouds and non-water oceans, such as methane. It would be interesting to study the effect of the air-ocean interface on the signals, as well as how wind speed and composition affect the crossing in the reflected flux curves.
- Making the planet orbits more realistic, such as by considering orbital variables like eccentricity and inclination, or even investigating combinations of the planets' ephemerides and their effect on the signal curves. In reality, polarimeters have integration times during which they collect photons. The longer the integration time, the more the instrument receives photons, and so the received signal will more accurately depict the real one. This could be investigated in conjunction with the system's photometric response for instance.
- Considering the absorption of gases. In this project we neglected the absorption of radiation by atmospheric molecules, mainly water, due to the time constraints. Future studies could give a closer look into the behaviour of water.
- Modeling the eclipse effect. We assumed the planets were infinitely small points and their signals immediately drop to zero once the planets go behind the star. This has room for improvement, such as by accounting for the real size of the planet, so the signal would go to zero in a smoother fashion. Another phenomenon that we did not consider is the drop in received stellar flux when the planet transits the star. While this effect is very small, accounting for it gives a more accurate representation of what the received signal would look like.

- Having a different type of cloud cover. In this work we assumed the cloud cover to be either a full deck or a patchy cover, which is assumed to be randomly distributed and follows from Eq. 3.20. This assumption is fairly accurate, but in reality the placement of clouds on planets is not entirely random and depends on many factors, such as the climate and circulation of each planet. Studying the exact location of clouds would simulate the reflected flux and degree of polarization signals much more accurately.
- Considering different cloud properties. In this work, we assumed that all clouds are cumulus and have an optical thickness of 30. Other cloud types optical thickness values could be investigated, which would yield different reflected flux and degree of polarization signals. We also assumed that the clouds-tops are located at an altitude of 3 km, where we demonstrated that the cloud altitude caused no difference in reflected flux and little difference in the degree of polarization (in Fig. 4.9). We also assumed a cloud thickness of 1 km based on Genkova et al. [10]. This may not be true for different planetary systems, so the cloud thickness can be reconsidered.
- Considering more than one atmospheric composition. For the majority of the report, we assumed that the atmospheric composition was homogeneous, and touched on the possibility of having an atmosphere made up of many constituents, such as the shaded region in Fig. 4.11. We also assumed that the atmospheric pressure on each Trappist-1 planet surface is 1 atm, which is similar to Earth's, though in reality this is never the case. For a different atmospheric composition and pressure, the signals would be different, so it is recommended to account for variations in these parameters.
- Looking into the chemical makeup of Trappist-1 planets' atmospheres. As the system's composition has not been observed, we have no data about the planets' atmospheres. So, we chose the planets' atmospheric composition values based on the available literature, with each paper having different assumptions. It would be beneficial to estimate the planets' atmospheric composition and evaluate how they interact with other phenomena, such as rotation, the presence of an ocean, and so on.

# A

# Refractive Indices

This appendix addresses how to compute the refractive indices of the atmospheric gases we used. The refractive indices, a characteristic of the atmosphere, are used in the codes to compute the $F$ and $P_s$ signals.

The wavenumber $\nu$, usually given in $cm^{-1}$, is the inverse of the wavelength, given as

$$\nu\ [cm^{-1}] = \frac{100}{\lambda\ [m]} \tag{A.1}$$

**Earth Air (dry)**

The equation for the refractive index $n_s[-]$ of Earth air, applicable for a wavelength range of $\lambda = 0.185 - 1.690\ \mu m$, is given by [48, 68]

$$[n_s(p_s, T_s, \lambda) - 1] \times 10^8 = 8060.51 + \frac{2480990}{132.274 - 1/\lambda^2} + \frac{17455.7}{39.32957 - 1/\lambda^2} \tag{A.2}$$

With $\lambda\ [\mu m]$ the wavelength, $T_S\ [K]$ the air temperature, and $p_s\ [hPa]$ the total air pressure.

**Hydrogen**

For hydrogen, the refractive index at $T = 293\ K$ and $p = 1.01325\ bar$ for the wavelength range $0.168 - 1.6945\ \mu m$ is given by [47]

$$n - 1 = \frac{0.0148956}{180.7 - 1/\lambda^2} + \frac{0.0049037}{92 - 1/\lambda^2} \tag{A.3}$$

With $\lambda\ [\mu m]$ the wavelength.

**Water Vapor**

The refractive index of water vapor is given by [46]

$$(n - 1) \times 10^7/\rho = 3.0198 + 0.16365\ \lambda^{-2} + 0.000133\ \lambda^{-4} \tag{A.4}$$

with $\lambda\ [\mu m]$ the wavelength and $\rho\ [g/m^3]$ the density.

**Liquid Water**

The refractive index $n_s$ $[-]$ of water for the range $0.2\ \mu m \leq \lambda \leq 200\ \mu m$ is given by [16]

$$n(\lambda_0) = n(\lambda_1) + \text{Prin.}\left[\frac{2(\lambda_1^2 - \lambda_0^2)}{\pi}\int_0^\infty \frac{\lambda k(\lambda d\lambda}{(\lambda_0^2 - \lambda^2)(\lambda_1^2 - \lambda^2)}\right] \tag{A.5}$$

With $\lambda_0$ $[\mu m]$ the desired wavelength, $n(\lambda_1)$ $[-]$ is a known value of the index of refraction at wavelength $\lambda_1$ $[\mu m]$, Prin. is the Cauchy principal of the integral, and $k(\lambda)$ $[-]$ the extinction coefficient.

At $\lambda = 1.15\ \mu m$, $n_{water} = 1.32475$ [16].

**Carbon Dioxide**

The refractive index $n_s$ $[-]$ of $CO_2$ at $15°C$ and $1013\ hPa$ is given by [6] and corrected by [62] as

$$\frac{n_s(\lambda) - 1}{1142.7} = \frac{5799.3}{16.6 \times 10^9 - 1/\lambda^2} + \frac{120}{7.96 \times 10^9 - 1/\lambda^2} + \frac{5.33}{5.63 \times 10^9 - 1/\lambda^2} + \frac{4.32}{4.6 \times 10^9 - 1/\lambda^2} + \frac{1.22 \times 10^{-5}}{5.85 \times 10^6 - 1/\lambda^2} \tag{A.6}$$

With $\lambda$ $[cm]$ the wavelength.

**Nitrogen**

For nitrogen, for wavelength range $0.468 \leq \lambda \leq 2.059\ \mu m$ $(4860\ cm^{-1} \leq \nu \leq 21360\ cm^{-1})$, the refractive index is [62]

$$(n - 1) \times 10^8 = 6498.2 + \frac{307.43305 \times 10^{12}}{14.4 \times 10^9 - \nu^2} \tag{A.7}$$

With $\nu$ $[cm^{-1}]$. Since nitrogen is a non-spherical molecule, it has a non-zero depolarization [62].

**Oxygen**

For oxygen, the refractive index at $T = 293\ K$ and $p = 1.01325\ bar$ for the wavelength range $0.4{-}1.8\ \mu m$ is given by [34]

$$n - 1 = 1.181494 \times 10^{-4} + \frac{9.708931 \times 10^{-3}}{75.4 - 1/\lambda^2} \tag{A.8}$$

With $\lambda$ $[\mu m]$.

**Methane**

For methane gas, the refractive index is [62]

$$(n - 1) \times 10^8 = 46662 + 4.02 \times 10^{-6}\ \nu^2 \tag{A.9}$$

With $\nu$ $[cm^{-1}]$.

Another source for the methane gas refractive index is [36]

$$n = 1.00042607 + (6.1396687 \times 10^{-6})\ \lambda^{-2} \tag{A.10}$$

With $\lambda$ $[\mu m]$.

# Bibliography


[1] C. Andreoli. NASA Planet Hunter Finds Earth-Size Habitable-Zone World, 2020. URL https://www.jpl.nasa.gov/news/news.php?feature=7569.

[2] David Andrews. *An Introduction to Atmospheric Physics*. Cambridge University Press, 1st edition, 2000.

[3] Rory Barnes. Tidal locking of habitable exoplanets. *Celestial Mechanics and Dynamical Astronomy*, 129(4):509–536, Dec 2017. doi: 10.1007/s10569-017-9783-7.

[4] Jack Barrett. Greenhouse molecules, their spectra and function in the atmosphere. *Energy & Environment*, 16(6):1037–1045, 2005. doi: 10.1260/095830505775221542. URL https://doi.org/10.1260/095830505775221542.

[5] Natasha E. Batalha, Nikole K. Lewis, Michael R. Line, Jeff Valenti, and Kevin Stevenson. Strategies for Constraining the Atmospheres of Temperate Terrestrial Planets with JWST. *Astrophysical Journal Letters*, 856(2):L34, April 2018. doi: 10.3847/2041-8213/aab896.

[6] A Bideau-Mehu, Y Guern, R Abjean, and A Johannin-Gilles. Interferometric determination of the refractive index of carbon dioxide in the ultraviolet region. *Optics Communications*, 9(4):432–434, 1973.

[7] L. Carone, R. Keppens, and L. Decin. Connecting the dots - II. Phase changes in the climate dynamics of tidally locked terrestrial exoplanets. *Monthly Notices of the Royal Astronomical Society*, 453(3):2412–2437, November 2015. doi: 10.1093/mnras/stv1752.

[8] Julien de Wit, Hannah R. Wakeford, Michaël Gillon, Nikole K. Lewis, Jeff A. Valenti, Brice-Olivier Demory, Adam J. Burgasser, Artem Burdanov, Laetitia Delrez, Emmanuël Jehin, Susan M. Lederer, Didier Queloz, Amaury H. M. J. Triaud, and Valérie Van Grootel. A combined transmission spectrum of the Earth-sized exoplanets TRAPPIST-1 b and c. *Nature*, 537(7618):69–72, Sep 2016. doi: 10.1038/nature18641.

[9] L. Delrez, M. Gillon, A. H. M. J. Triaud, B. O. Demory, J. de Wit, J. G. Ingalls, E. Agol, E. Bolmont, A. Burdanov, A. J. Burgasser, S. J. Carey, E. Jehin, J. Leconte, S. Lederer, D. Queloz, F. Selsis, and V. Van Grootel. Early 2017 observations of TRAPPIST-1 with Spitzer. *Monthly Notices of the Royal Astronomical Society*, 475(3):3577–3597, April 2018. doi: 10.1093/mnras/sty051.

[10] Iliana Genkova, Gabriela Seiz, Paquita Zuidema, Guangyu Zhao, and Larry Di Girolamo. Cloud top height comparisons from aster, misr, and modis for trade wind cumuli. *Remote sensing of environment*, 107(1-2):211–222, 2007.

[11] Michaël Gillon, Emmanuël Jehin, Susan M. Lederer, Laetitia Delrez, Julien de Wit, Artem Burdanov, Valérie Van Grootel, Adam J. Burgasser, Amaury H. M. J. Triaud, Cyrielle Opitom, Brice-Olivier Demory, Devendra K. Sahu, Daniella Bardalez Gagliuffi, Pierre Magain, and Didier Queloz. Temperate Earth-sized planets transiting a nearby ultracool dwarf star. *Nature*, 533(7602):221–224, May 2016. doi: 10.1038/nature17448.

[12] Michaël Gillon, Amaury H. M. J. Triaud, Brice-Olivier Demory, Emmanuël Jehin, Eric Agol, Katherine M. Deck, Susan M. Lederer, Julien de Wit, Artem Burdanov, James G. Ingalls, Emeline Bolmont, Jeremy Leconte, Sean N. Raymond, Franck Selsis, Martin Turbet, Khalid Barkaoui, Adam Burgasser, Matthew R. Burleigh, Sean J. Carey, Aleksander Chaushev, Chris M. Copperwheat, Laetitia Delrez, Catarina S. Fernandes, Daniel L. Holdsworth, Enrico J. Kotze, Valérie Van Grootel, Yaseen Almleaky, Zouhair Benkhaldoun, Pierre Magain, and Didier Queloz. Seven temperate terrestrial planets around the nearby ultracool dwarf star TRAPPIST-1. *Nature*, 542(7642):456–460, February 2017. doi: 10.1038/nature21360.

[13] Goddard Spaceflight Center. General Questions About Webb. URL https://jwst.nasa.gov/content/about/faqs/faq.html#sharp.

[14] Thomas P. Greene, Michael R. Line, Cezar Montero, Jonathan J. Fortney, Jacob Lustig-Yaeger, and Kyle Luther. CHARACTERIZING TRANSITING EXOPLANET ATMOSPHERES WITH JWST. *The Astrophysical Journal*, 817(1):17, jan 2016. doi: 10.3847/0004-637x/817/1/17. URL https://doi.org/10.3847%2F0004-637x%2F817%2F1%2F17.

[15] Simon L. Grimm, Brice-Olivier Demory, Michaël Gillon, Caroline Dorn, Eric Agol, Artem Burdanov, Laetitia Delrez, Marko Sestovic, Amaury H. M. J. Triaud, Martin Turbet, and et al. The nature of the trappist-1 exoplanets. *Astronomy & Astrophysics*, 613:A68, May 2018. ISSN 1432-0746. doi: 10.1051/0004-6361/201732233. URL http://dx.doi.org/10.1051/0004-6361/201732233.

[16] George M Hale and Marvin R Querry. Optical constants of water in the 200-nm to 200-$\mu$m wavelength region. *Applied optics*, 12(3):555–563, 1973.

[17] J. E. Hansen and L. D. Travis. Light scattering in planetary atmospheres. *Space Science Reviews*, 16(4):527–610, Oct 1974. doi: 10.1007/BF00168069.

[18] Chao He, Sarah M. Hörst, Nikole K. Lewis, Julianne I. Moses, Eliza M. R. Kempton, Mark S. Marley, Caroline V. Morley, Jeff A. Valenti, and Véronique Vuitton. Gas Phase Chemistry of Cool Exoplanet Atmospheres: Insight from Laboratory Simulations. *arXiv e-prints*, art. arXiv:1812.06957, Dec 2018.

[19] H. J. Hoeijmakers, F. Snik, D. M. Stam, and C. U. Keller. LOUPE: Spectropolarimetry of the Earth from the surface of the Moon. In *European Planetary Science Congress*, volume 9, pages EPSC2014–574, April 2014.

[20] John Houghton. *The Physics of Atmospheres*. Cambridge University Press, 3rd edition, 2002.

[21] Yongyun Hu and Jun Yang. Role of ocean heat transport in climates of tidally locked exoplanets around m dwarf stars. *Proceedings of the National Academy of Sciences*, 111(2):629–634, 2014. ISSN 0027-8424. doi: 10.1073/pnas.1315215111. URL https://www.pnas.org/content/111/2/629.

[22] *Definition of Terms Used Within the DDC Pages*. Intergovernmental Panel on Climate Change, 2018.

[23] D. J. Jacob. *Introduction to Atmospheric Chemistry*. Princeton University Press, 1999.

[24] Manoj M. Joshi and Robert M. Haberle. Suppression of the Water Ice and Snow Albedo Feedback on Planets Orbiting Red Dwarf Stars and the Subsequent Widening of the Habitable Zone. *Astrobiology*, 12(1):3–8, Jan 2012. doi: 10.1089/ast.2011.0668.

[25] A. Kamp. *Space Instrumentation Engineering*. TU Delft, 2007.

[26] T. Karalidi, D. M. Stam, and J. W. Hovenier. Looking for the rainbow on exoplanets covered by liquid and icy water clouds. *Astronomy & Astrophysics*, 548:A90, December 2012. doi: 10.1051/0004-6361/201220245.

[27] Markus Kasper, J-L Beuzit, Christophe Verinaud, P Baudoz, A Boccaletti, R Gratton, C Keller, F Kerber, HM Schmid, N Thatte, et al. Epics, the exoplanet imager for the e-elt. In *1st AO4ELT conference-Adaptive Optics for Extremely Large Telescopes*, page 02009. EDP Sciences, 2010. URL https://www.eso.org/sci/libraries/SPIE2008/7015-63.pdf.

[28] D. Kitzmann, A. B. C. Patzer, P. von Paris, M. Godolt, B. Stracke, S. Gebauer, J. L. Grenfell, and H. Rauer. Clouds in the atmospheres of extrasolar planets. I. Climatic effects of multi-layered clouds for Earth-like planets and implications for habitable zones. *Astronomy & Astrophysics*, 511:A66, February 2010. doi: 10.1051/0004-6361/200913491.

[29] W. J. J. Knibbe, J. F. de Haan, J. W. Hovenier, D. M. Stam, R. B. A. Koelemeijer, and P. Stammes. Deriving terrestrial cloud top pressure from photopolarimetry of reflected light. *Journal of Quantitative Spectroscopy & Radiative Transfer*, 64(2):173–199, Jan 2000. doi: 10.1016/S0022-4073(98)00135-6.

[30] R. K. Kopparapu, E. T. Wolf, G. Arney, N. E. Batalha, J. Haqq-Misra, S. L. Grimm, and K. Heng. Habitable moist atmospheres on terrestrial planets near the inner edge of the habitable zone around m dwarfs. *The Astrophysical Journal*, 845(1):5, August 2017. doi: 10.3847/1538-4357/aa7cf9. URL https://doi.org/10.3847%2F1538-4357%2Faa7cf9.

[31] Ravi Kumar Kopparapu, Ramses Ramirez, James F. Kasting, Vincent Eymet, Tyler D. Robinson, Suvrath Mahadevan, Ryan C. Terrien, Shawn Domagal-Goldman, Victoria Meadows, and Rohit Deshpande. Habitable Zones around Main-sequence Stars: New Estimates. *The Astrophysical Journal*, 765(2):131, March 2013. doi: 10.1088/0004-637X/765/2/131.

[32] Ravi Kumar Kopparapu, Ramses M. Ramirez, James SchottelKotte, James F. Kasting, Shawn Domagal-Goldman, and Vincent Eymet. Habitable zones around main-sequence stars: Dependence on planetary mass. *The Astrophysical Journal*, 787(2):L29, May 2014. ISSN 2041-8213. doi: 10.1088/2041-8205/787/2/l29. URL http://dx.doi.org/10.1088/2041-8205/787/2/L29.

[33] Pushkar Kopparla, Vijay Natraj, David Crisp, Kimberly Bott, Mark R Swain, and Yuk L Yung. Observing oceans in tightly packed planetary systems: Perspectives from polarization modeling of the TRAPPIST-1 system. *The Astronomical Journal*, 156(4):143, sep 2018. doi: 10.3847/1538-3881/aad9a1. URL https://doi.org/10.3847%2F1538-3881%2Faad9a1.

[34] Petr Křen. Comment on “Precision refractive index measurements of air, N_2, O_2, Ar, and CO_2 with a frequency comb”. *Applied Optics*, 50(35):6484, December 2011. doi: 10.1364/AO.50.006484.

[35] Andrew P. Lincowski, Victoria S. Meadows, David Crisp, Tyler D. Robinson, Rodrigo Luger, Jacob Lustig-Yaeger, and Giada N. Arney. Evolved climates and observational discriminants for the TRAPPIST-1 planetary system. *The Astrophysical Journal*, 867(1):76, November 2018. doi: 10.3847/1538-4357/aae36a. URL https://doi.org/10.3847%2F1538-4357%2Faae36a.

[36] Stanisław Loria. Über die dispersion des lichtes in gasförmigen kohlenwasserstoffen. *Annalen der Physik*, 334(8):605–622, 1909.

[37] Rodrigo Luger, Marko Sestovic, Ethan Kruse, Simon L. Grimm, Brice-Olivier Demory, Eric Agol, Emeline Bolmont, Daniel Fabrycky, Catarina S. Fernandes, Valérie Van Grootel, Adam Burgasser, Michaël Gillon, James G. Ingalls, Emmanuël Jehin, Sean N. Raymond, Franck Selsis, Amaury H. M. J. Triaud, Thomas Barclay, Geert Barentsen, Steve B. Howell, Laetitia Delrez, Julien de Wit, Daniel Foreman-Mackey, Daniel L. Holdsworth, Jérémy Leconte, Susan Lederer, Martin Turbet, Yaseen Almleaky, Zouhair Benkhaldoun, Pierre Magain, Brett M. Morris, Kevin Heng, and Didier Queloz. A seven-planet resonant chain in TRAPPIST-1. *Nature Astronomy*, 1:0129, June 2017. doi: 10.1038/s41550-017-0129.

[38] Nikku Madhusudhan and Seth Redfield. Optimal measures for characterizing water-rich super-earths. *International Journal of Astrobiology*, 14(2):177–189, 2015. doi: 10.1017/S1473550414000421.

[39] Mark S. Marley and Sujan Sengupta. Probing the physical properties of directly imaged gas giant exoplanets through polarization. *Monthly Notices of the Royal Astronomical Society*, 417(4):2874–2881, November 2011. doi: 10.1111/j.1365-2966.2011.19448.x.

[40] John V Martonchik and Glenn S Orton. Optical constants of liquid and solid methane. *Applied optics*, 33(36):8306–8317, 1994.

[41] François Ménard, Xavier Delfosse, and J-L Monin. Optical linear polarimetry of ultra cool dwarfs. *Astronomy & Astrophysics*, 396(3):L35–L38, 2002.

[42] Sarah E. Moran, Sarah M. Hörst, Natasha E. Batalha, Nikole K. Lewis, and Hannah R. Wakeford. Limits on clouds and hazes for the TRAPPIST-1 planets. *The Astronomical Journal*, 156(6):252, November 2018. doi: 10.3847/1538-3881/aae83a. URL https://doi.org/10.3847%2F1538-3881%2Faae83a.

[43] Caroline V. Morley, Laura Kreidberg, Zafar Rustamkulov, Tyler Robinson, and Jonathan J. Fortney. Observing the Atmospheres of Known Temperate Earth-sized Planets with JWST. *The Astrophysical Journal*, 850(2):121, December 2017. doi: 10.3847/1538-4357/aa927b.

[44] M. B. Murrill. Astronomers Do It Again: Find Organic Molecules Around Gas Planet, 2009. URL https://www.nasa.gov/mission_pages/spitzer/news/spitzer-20091020.html.

[45] Eduard Muslimov, Jean-Claude Bouret, Coralie Neiner, Arturo López Ariste, Marc Ferrari, Sébastien Vivès, Emmanuel Hugot, Robert Grange, Simona Lombardo, Louise Lopes, Josiane Costeraste, and Frank Brachet. POLLUX: a UV spectropolarimeter for the LUVOIR space telescope project. In *Proceedings of the Society of Photo-Optical Instrumentation Engineers*, volume 10699 of *Society of Photo-Optical Instrumentation Engineers (SPIE) Conference Series*, page 1069906, July 2018. doi: 10.1117/12.2310133.

[46] Kenneth B. Newbound. Refractive indices of water vapor and carbon dioxide at low pressure. *Journal of the Optical Society of America (1917-1983)*, 39(10):835, October 1949.

[47] Edson R Peck and Shiezen Huang. Refractivity and dispersion of hydrogen in the visible and near infrared. *Journal of the Optical Society of America*, 67(11):1550–1554, 1977.

[48] Edson R. Peck and Kaye Reeder. Dispersion of air*. *Journal of the Optical Society of America*, 62(8):958–962, Aug 1972. doi: 10.1364/JOSA.62.000958. URL http://www.osapublishing.org/abstract.cfm?URI=josa-62-8-958.

[49] R. T. Pierrehumbert. A Palette of Climates for Gliese 581g. *Astrophysical Journal Letters*, 726(1):L8, January 2011. doi: 10.1088/2041-8205/726/1/L8.

[50] Joseph E. Rodriguez, Andrew Vanderburg, Sebastian Zieba, Laura Kreidberg, Caroline V. Morley, Stephen R. Kane, Alton Spencer, Samuel N. Quinn, Jason D. Eastman, Ryan Cloutier, Chelsea X. Huang, Karen A. Collins, Andrew W. Mann, Emily Gilbert, Joshua E. Schlieder, Elisa V. Quintana, Thomas Barclay, Gabrielle Suissa, Ravi kumar Kopparapu, Courtney D. Dressing, George R. Ricker, Roland K. Vanderspek, David W. Latham, Sara Seager, Joshua N. Winn, Jon M. Jenkins, Zachory Berta-Thompson, Patricia T. Boyd, David Charbonneau, Douglas A. Caldwell, Eugene Chiang, Jessie L. Christiansen, David R. Ciardi, Knicole D. Colón, John Doty, Tianjun Gan, Natalia Guerrero, Maximilian N. Günther, Eve J. Lee, Alan M. Levine, Eric Lopez, Philip S. Muirhead, Elisabeth Newton, Mark E. Rose, Joseph D. Twicken, and Jesus Noel Villaseñor. The First Habitable Zone Earth-Sized Planet From TESS II: *Spitzer* Confirms TOI-700 d. *arXiv e-prints*, art. arXiv:2001.00954, January 2020.

[51] S. M. A. Rodts, P. G. Duynkerke, and H. J. J. Jonker. Size Distributions and Dynamical Properties of Shallow Cumulus Clouds from Aircraft Observations and Satellite Data. *Journal of Atmospheric Sciences*, 60:1895–1912, August 2003. doi: 10.1175/1520-0469(2003)060<1895:SDADPO>2.0.CO;2.

[52] L. Rossi and D. M. Stam. Using polarimetry to retrieve the cloud coverage of Earth-like exoplanets. *Astronomy & Astrophysics*, 607:A57, November 2017. doi: 10.1051/0004-6361/201730586.

[53] Loïc Rossi, Javier Berzosa-Molina, and Daphne M. Stam. PYMIEDAP: a Python-Fortran tool for computing fluxes and polarization signals of (exo)planets. *Astronomy & Astrophysics*, 616:A147, September 2018. doi: 10.1051/0004-6361/201832859.

[54] Loïc Rossi, Ashwyn Groot, Thomas Fauchez, and Daphne M Stam. Investigating cloud cover variability on earth-like exoplanets using polarimetry. In *European Planetary Science Congress 2018*, 2018.

[55] H. M. Schmid, J. L. Beuzit, M. Feldt, D. Gisler, R. Gratton, Th. Henning, F. Joos, M. Kasper, R. Lenzen, D. Mouillet, C. Moutou, A. Quirrenbach, D. M. Stam, C. Thalmann, J. Tinbergen, C. Verinaud, R. Waters, and R. Wolstencroft. Search and investigation of extra-solar planets with polarimetry. In C. Aime and F. Vakili, editors, *IAU Colloq. 200: Direct Imaging of Exoplanets: Science amp; Techniques*, pages 165–170, January 2006. doi: 10.1017/S1743921306009252.

[56] Gavin A. Schmidt, Reto A. Ruedy, Ron L. Miller, and Andy A. Lacis. Attribution of the present-day total greenhouse effect. *Journal of Geophysical Research (Atmospheres)*, 115(D20):D20106, Oct 2010. doi: 10.1029/2010JD014287.

[57] Donald P. Schneider, Jesse L. Greenstein, Maarten Schmidt, and James E. Gunn. Spectroscopy of an unusual emission line m star. *The Astronomical Journal*, 102:1180–1190, 1991.

[58] S. Seager, B. A. Whitney, and D. D. Sasselov. Photometric Light Curves and Polarization of Close-in Extrasolar Giant Planets. *The Astrophysical Journal*, 540(1):504–520, September 2000. doi: 10.1086/309292.

[59] Sara Seager. *Exoplanet Atmospheres: Physical Processes*. Princeton University Press, 2010.

[60] Sujan Sengupta. Polarization of Trappist-1 by the Transit of Its Planets. *The Astrophysical Journal*, 861(1):41, July 2018. doi: 10.3847/1538-4357/aac6da.

[61] A. L. Shields, S. Ballard, and J. A. Johnson. The Habitability of Planets Orbiting M-dwarf Stars. *Physics Reports*, 663:1–38, 2016. doi: 10.1016/j.physrep.2016.10.003.

[62] Maarten Sneep and Wim Ubachs. Direct measurement of the Rayleigh scattering cross section in various gases. *Journal of Quantitative Spectroscopy and Radiative Transfer*, 92(3):293–310, May 2005. doi: 10.1016/j.jqsrt.2004.07.025.

[63] David S. Spiegel, Kristen Menou, and Caleb A. Scharf. Habitable Climates: The Influence of Obliquity. *The Astrophysical Journal*, 691(1):596–610, Jan 2009. doi: 10.1088/0004-637X/691/1/596.

[64] D. M. Stam. Spectropolarimetric signatures of Earth-like extrasolar planets. *Astronomy & Astrophysics*, 482:989–1007, May 2008. doi: 10.1051/0004-6361:20078358.

[65] D. M. Stam. Light and Radiation, 2019.

[66] D. M. Stam, J. W. Hovenier, and L. B. F. M. Waters. Using polarimetry to detect and characterize Jupiter-like extrasolar planets. *Astronomy & Astrophysics*, 428:663–672, December 2004. doi: 10.1051/0004-6361:20041578.

[67] R. Stull, L. Berg, H. Modzelewski, and K. Schrieber. Size Distributions of Boundary-Layer Clouds. URL https://www.arm.gov/publications/proceedings/conf05/extended_abs/stull_r.pdf.

[68] Claudio Tomasi, Vito Vitale, Boyan Petkov, Angelo Lupi, and Alessandra Cacciari. Improved algorithm for calculations of rayleigh-scattering optical depth in standard atmospheres. *Applied Optics*, 44(16):3320–3341, Jun 2005. doi: 10.1364/AO.44.003320. URL http://ao.osa.org/abstract.cfm?URI=ao-44-16-3320.

[69] V. J. H. Trees. Transfer of Polarized Light in an (Exo)planetary Atmosphere-Ocean System. Master's thesis, Delft University of Technology, December 2018.

[70] Martin Turbet, Emeline Bolmont, Jeremy Leconte, François Forget, Franck Selsis, Gabriel Tobie, Anthony Caldas, Joseph Naar, and Michaël Gillon. Modeling climate diversity, tidal dynamics and the fate of volatiles on TRAPPIST-1 planets. *Astronomy & Astrophysics*, 612:A86, May 2018. doi: 10.1051/0004-6361/201731620.

[71] Cayman T. Unterborn, Steven J. Desch, Natalie R. Hinkel, and Alejandro Lorenzo. Inward migration of the TRAPPIST-1 planets as inferred from their water-rich compositions. *Nature Astronomy*, 2:297–302, March 2018. doi: 10.1038/s41550-018-0411-6.

[72] Valérie Van Grootel, Catarina S Fernandes, Michael Gillon, Emmanuel Jehin, Jean Manfroid, Richard Scuflaire, Adam J Burgasser, Khalid Barkaoui, Zouhair Benkhaldoun, Artem Burdanov, et al. Stellar parameters for trappist-1. *The Astrophysical Journal*, 853(1):30, 2018.

[73] M. Way, A. D. Del Genio, N. Y. Kiang, M. Kelley, I. D. Aleinov, T. Clune, and M. J. Puma. Exploring the Inner Edge of the Habitable Zone with Fully Coupled Oceans. In *AGU Fall Meeting Abstracts*, volume 2015, pages P34C–07, Dec 2015.

[74] D. R. Williams. Sun Fact Sheet, 2018. URL https://nssdc.gsfc.nasa.gov/planetary/factsheet/sunfact.html.

[75] D. R. Williams. Earth Fact Sheet, 2019. URL https://nssdc.gsfc.nasa.gov/planetary/factsheet/earthfact.html.

[76] Eric T. Wolf. Assessing the habitability of the TRAPPIST-1 system using a 3d climate model. *The Astrophysical Journal*, 839(1):L1, April 2017. doi: 10.3847/2041-8213/aa693a. URL https://doi.org/10.3847%2F2041-8213%2Faa693a.

[77] Jun Yang, Nicolas B. Cowan, and Dorian S. Abbot. Stabilizing Cloud Feedback Dramatically Expands the Habitable Zone of Tidally Locked Planets. *Astrophysical Journal Letters*, 771(2):L45, Jul 2013. doi: 10.1088/2041-8205/771/2/L45.

[78] Jun Yang, Gwenaël Boué, Daniel C. Fabrycky, and Dorian S. Abbot. Strong Dependence of the Inner Edge of the Habitable Zone on Planetary Rotation Rate. *Astrophysical Journal Letters*, 787 (1):L2, May 2014. doi: 10.1088/2041-8205/787/1/L2.